

NASA TECHNICAL  
REPORT



NASA TR R-185

2.1

NASA TR R-185

LOAN

0068084



TECH LIBRARY KAFB, NM

AERODYNAMIC HEATING OF CONICAL  
ENTRY VEHICLES AT SPEEDS IN  
EXCESS OF EARTH PARABOLIC SPEED

*by H. Julian Allen, Alvin Seiff,  
and Warren Winovich*

*Ames Research Center  
Moffett Field, California*

# ERRATA

*Completed  
Apr 19 Oct 65*

NASA Technical Report R-185

## AERODYNAMIC HEATING OF CONICAL ENTRY VEHICLES AT SPEEDS IN EXCESS OF EARTH PARABOLIC SPEED

By H. Julian Allen, Alvin Seiff, and Warren Winovich

Appendix B, page 36:

Equations (B10a) and (B10b) should read:

$$Z_e = 0.14 \left( \frac{V_E \sin \theta_w}{10^4} \right)^{12.45} ; \quad \frac{V_E \sin \theta_w}{10^4} < 1.37 \quad (\text{B10a})$$

$$Z_e = 0.14 \left( \frac{V_E \sin \theta_w}{10^4} \right)^{12.45} \left[ 1 - 1.074 x_1^{1.8} \left( \frac{1}{1.8} - \frac{x_1}{2.8} + \frac{x_1^2}{2!(3.8)} - \frac{x_1^3}{3!(4.8)} + \dots \right) \right] \\ + 39 \left( \frac{V_E \sin \theta_w}{10^4} \right)^{2.05} x_2^{1.8} \left( \frac{1}{1.8} - \frac{x_2}{2.8} + \frac{x_2^2}{2!(3.8)} - \frac{x_2^3}{3!(4.8)} + \dots \right) ;$$

$$\frac{V_E \sin \theta_w}{10^4} > 1.37 \quad (\text{B10b})$$

The coefficients 0.14 and 39 in these equations replace the values given in the report which were in error by a factor of 2. The table of values of  $Z_e$ , table II, page 61, and the corresponding values of  $\eta_e$  in the figures are correct as given in the report.



0068084

AERODYNAMIC HEATING OF CONICAL ENTRY VEHICLES AT SPEEDS  
IN EXCESS OF EARTH PARABOLIC SPEED

By H. Julian Allen, Alvin Seiff,  
and Warren Winovich

Ames Research Center  
Moffett Field, Calif.

NATIONAL AERONAUTICS AND SPACE ADMINISTRATION

---

For sale by the Office of Technical Services, Department of Commerce,  
Washington, D. C. 20230 -- Price \$2.25

# AERODYNAMIC HEATING OF CONICAL ENTRY VEHICLES AT SPEEDS

## IN EXCESS OF EARTH PARABOLIC SPEED

By H. Julian Allen, Alvin Seiff,  
and Warren Winovich

### SUMMARY

The aerodynamic heating characteristics during Earth's atmosphere entry at speeds greater than Earth parabolic speed are calculated for vehicles of conical shape. Ablative heat shields are assumed for these bodies and both laminar and turbulent boundary layers are considered. It is shown that if conical shape can be maintained, an optimum cone angle will exist and a cone of this angle will be superior to the more usual blunt entry shapes at speed well in excess of parabolic speed. The improvements result from the fact that radiative heat-transfer contributions from the shock layer are much reduced for the cones so that, although the convective contributions are increased, a net gain is realized. For optimum cones, the approximate analysis indicates that the convective contributions constitute 85 to 90 percent of the total heating. Solutions to the problem of maintaining conical shape as ablation progresses are considered, and some experimental demonstrations of means for accomplishing this are presented.

### INTRODUCTION

Interplanetary travel may require entry into planetary atmospheres at speeds well in excess of parabolic speed in order to shorten trip times (ref. 1). Figure 1 shows trip time as a function of entry speed into Earth's atmosphere for travel from Mars and Venus. There are limits which must be set for the maximum entry speed allowable because of both the loads entailed (ref. 2) and the aerodynamic heating. In this report we shall be concerned only with the heating aspects.

Up to the present time, atmosphere entry speeds have been sufficiently low that aerodynamic heating has been essentially a convective process. Osborne Reynolds long ago (ref. 3) showed that the molecular process by which a frictional force is exerted on an aerodynamic surface is directly related to the process by which heat can be convected to that surface. In consequence, it can be shown (ref. 4) that the incremental quantity of energy in the form of heat convected to an entry vehicle,  $\delta H$ , is related to the increment in time,  $\delta t$ , by

the proportionality<sup>1</sup>

$$\delta H \sim F V \delta t \quad (1)$$

where  $F$  is the total frictional force exerted on the vehicle. On the other hand, the incremental change in kinetic energy in the same interval is given by

$$\delta E = D V \delta t \quad (2)$$

where  $D$  is the total drag force experienced by the vehicle. It follows that

$$\delta H \sim \frac{F}{D} \delta E \quad (3)$$

Let us consider that the ratio of the friction force to the drag remains essentially constant. The total energy in the form of heat convected to the vehicle during entry is then proportional to the total kinetic energy change which occurs during entry, and, for a vehicle which is not to be destroyed on landing at the planet's surface, this total kinetic energy is simply the kinetic energy of the vehicle at entry to the atmosphere. To minimize the convective heating, then, one must choose a vehicle shape with the smallest ratio of frictional force to total drag force. Thus one chooses blunt shapes for which pressure drag is high, in order that the drag coefficient may be made as large as possible. The amount of heat transferred by convection depends upon whether the boundary layer is laminar or turbulent. At the usual Reynolds numbers characteristic of entry, it is advantageous to have laminar flow. Accordingly, one strives to maintain such a flow. Also most entry bodies employ ablative shields for heat protection. In part, ablative systems are used because the ablating vapors fend off the air and so reduce the shear in the boundary layer from what it would be in the absence of these vapors, and, hence, the convective heat transfer as well. Under optimum conditions of high pressure drag and low frictional force, the fraction of the total kinetic energy convected to the entry vehicle can be kept very low indeed - of the order of 1/10 or 1 percent or less.

When, now, one considers the higher entry speeds desired in the future, one finds it difficult to prevent the heat transfer for a blunt body from increasing rapidly with increase in speed because convection is no longer the sole important heating mechanism involved. In the new speed regime the air which enters the bow shock layer undergoes such high molecular excitations that it becomes a powerful source of radiative energy. This process is well described in the literature (e.g., refs. 5 to 10). At this point it is only necessary to note that the most important radiative contribution to aerodynamic heating varies with velocity by as much as the fifteenth power and almost directly as the density. Hence, although for entry at near-Earth satellite speed the radiative contribution for a blunt body is usually trivial, it tends to become overwhelming at speeds well in excess of Earth parabolic speed. One is led, therefore, to re-examine the effect of vehicle shape when radiative contributions to heating are important.

---

<sup>1</sup>All symbols are defined in appendix A.

To this end, consider the conical body shown in figure 2. As an entry vehicle, it has the disadvantage of its drag coefficient being less than that for an essentially flat-faced body so that, other factors being equal, it must accept a larger convective heat load. On the other hand, the radiation per unit of shock layer volume depends upon excitation of the gas in the shock layer and so depends upon the component of velocity normal to the bow shock. This radiation varies as about the fifteenth power of the sine of the shock angle. Thus, at sufficiently high entry speeds, a reduction in shock angle, which increases convective heat input but greatly reduces the radiative heat input, can provide a net gain. Under these conditions it is to be expected that an optimum cone angle exists for any given set of entry conditions. It is the purpose of this paper to analyze entry bodies of conical shape to find these optimums. The metric system of units (kilogram-meter-second) are employed throughout this analysis.

### ANALYSIS

The rate of energy input in the form of heat to an entry body may be written (ref. 11)

$$\frac{dH}{dt} = \frac{1}{2} C_H \rho V^3 A \quad (4)$$

A number of assumptions will be made to simplify the analysis. The first two are that aerodynamic lift is zero and that during the time the heating process is important, the deceleration is large compared to the acceleration of gravity; hence, the gravitational effect can be ignored. In this case the trajectory is essentially a straight line (ref. 4) so that the time rate of change of altitude,  $Y$ , is

$$\frac{dY}{dt} = -V \sin \gamma \quad (5)$$

where  $\gamma$  is the flight-path angle as measured down from the local horizontal and is constant. The third assumption is that the air density in the atmosphere varies exponentially with altitude (see ref. 4, 11, or 12).

$$\rho = \bar{\rho} \rho_0 = \rho_0 e^{-\beta Y} \quad (6)$$

where  $\bar{\rho}$  is the air density in terms of a reference sea-level density,  $\rho_0$ , and  $\beta$  is a constant.

From equations (5) and (6) then

$$dt = - \frac{dY}{V \sin \gamma} = \frac{d\bar{\rho}}{\beta \bar{\rho} V \sin \gamma} \quad (7)$$

The fourth and fifth assumptions are that the drag coefficient is constant, and that the mass remains essentially constant during the entry. Thus, from reference 4,

$$V^2 = V_E^2 e^{-B\bar{\rho}} \quad (8)$$

where  $V_E$  is the vehicle speed at atmosphere entry and  $B$  is the ballistic coefficient

$$B = \frac{C_D \rho_0 A}{\beta m \sin \gamma} \quad (9)$$

where  $m$  is the entry body mass.

With equations (4), (7), and (8), the energy input to the entry vehicle in the form of heat for the whole entry is

$$H = \frac{\rho_0 V_E^2 A}{2\beta \sin \gamma} \int_{\bar{\rho}=0}^1 C_H e^{-B\bar{\rho}} d\bar{\rho} \quad (10)$$

The total kinetic energy change during entry is

$$E = \frac{1}{2} m V_E^2 \quad (11)$$

since the final speed at landing is zero for a vehicle which is to land intact. Then equations (9), (10), and (11) combined give the fraction of the total kinetic energy which appears as heat to the vehicle,  $\eta$ , as

$$\eta = \frac{H}{E} = \frac{B}{C_D} \int_{\bar{\rho}=0}^1 C_H e^{-B\bar{\rho}} d\bar{\rho} \quad (12)$$

The sixth assumption is that the heat shield is the ablation type for which mass loss is only by the process of sublimation or vaporization. Let  $\xi$  be the heat required to bring a unit mass of ablator from the cold state through vaporization expressed in kinetic energy units (i.e., in units of square of velocity). Then the mass loss by ablation in terms of the entry vehicle mass will be

$$\frac{\Delta m}{m} = \eta \left( \frac{V_E^2}{2\xi} \right) \quad (13)$$

We now proceed to determine the energy fractions,  $\eta$ , as a function of entry speed for conical bodies under the assumption (seventh) that the cone angle of the conical body remains unchanged during ablation. To this end we determine  $\eta$  as the sum of the contributions due to equilibrium radiative heating (denoted by  $\eta_e$ ),

the nonequilibrium radiative heating (denoted by  $\eta_n$ ), and either the laminar convective heating (denoted by  $\eta_l$ ) or the turbulent convective heating (denoted by  $\eta_t$ ). The eighth assumption is that each contribution may be calculated independently of the other. Cases for mixed laminar flow and turbulent flow are not treated but the limiting effect of approach to free-molecular flow is included. The drag coefficient used in the evaluation of  $\eta$  is assumed to be the Newtonian value (ninth assumption)

$$C_D = 2 \sin^2 \theta_C \quad (14)$$

where  $\theta_C$  is the half-cone angle. Thus, base pressure is ignored since the speeds of interest are great, and effects of friction on drag are ignored on the presumption that the cones of interest are never slender enough to warrant the complication of including this effect.

#### Equilibrium Radiative Heating

For the purposes of this analysis it has been assumed (tenth and eleventh assumptions) that the radiation per unit volume from a shock layer which is in thermodynamic and chemical equilibrium is constant throughout the shock layer (i.e., energy depletion due to radiation is ignored) and is nonabsorptive within the layer. The equilibrium radiation (appendix B) is, under these conditions, determined solely by the density,  $\bar{\rho}$ , ahead of the bow shock and the velocity normal to it.

$$U = V \sin \theta_W \quad (15)$$

An examination of the available data indicates (see appendix B) that the time rate of equilibrium radiation per unit volume of gas cap can be expressed approximately for the lower speed range

$$\frac{d\dot{E}_e}{dv} = C_{e1} U^{q_1} \bar{\rho}^p ; \quad U < U_{1,2} = 13,700 \text{ m/sec} \quad (16a)$$

and for the upper speed range

$$\frac{d\dot{E}_e}{dv} = C_{e2} U^{q_2} \bar{\rho}^p ; \quad U > U_{1,2} = 13,700 \text{ m/sec} \quad (16b)$$

wherein



$$\left. \begin{aligned}
 p &= 1.80 \\
 q_1 &= 15.45 \\
 q_2 &= 5.05 \\
 C_{e1} &= 6.14 \times 10^{-49} \frac{\text{kg}}{\text{m sec}^3} \left( \frac{\text{sec}}{\text{m}} \right)^{15.45} \\
 C_{e2} &= 6.44 \times 10^{-6} \frac{\text{kg}}{\text{m sec}^3} \left( \frac{\text{sec}}{\text{m}} \right)^{5.05}
 \end{aligned} \right\} \quad (17)$$

The time rate of the total equilibrium radiation from the shock layer is

$$\dot{E}_e = \frac{d\dot{E}_e}{dv} v \quad (18)$$

and approximately half of this radiation is received by the body surface, if there is no surface reflectivity. Then the equilibrium-radiation heat-transfer coefficient is

$$C_{He} = \frac{(1/2)\dot{E}_e}{(1/2)\rho V^3 A} = \frac{(d\dot{E}_e/dv)v}{\rho_o \bar{\rho} V^3 A} \quad (19)$$

where

$$\left. \begin{aligned}
 v &= \pi r_b^3 \left( \frac{\tan^2 \theta_W - \tan^2 \theta_C}{3 \tan^3 \theta_C} \right) \\
 A &= \pi r_b^2
 \end{aligned} \right\} \quad (20)$$

while for the ARDC standard atmosphere (ref. 13)

$$\rho_o = 1.225 \text{ kg/m}^3 \quad (21)$$

so that from equations (16), (8), and (14), equation (12) becomes<sup>2</sup> for  $V_E < U_{1,2}/\sin \theta_W$

---

<sup>2</sup>Properly, the value of  $C_{He}$  should be made zero in the free-molecular flow regime but the strong dependence of  $\eta_e$  on  $\bar{\rho}$  in equations (22a) and (22b) makes the contribution of the integral to  $\eta_e$  for the free-molecular altitudes negligible for vehicle weights and sizes of usual interest.

$$\eta_e = Br_b c_{e1} V_e^{q_1-3} \left[ \frac{\sin^{q_1} \theta_W (\tan^2 \theta_W - \tan^2 \theta_C)}{6 \sin^2 \theta_C \tan^3 \theta_C} \right] \int_{\bar{\rho}=0}^1 e^{-(B/2)(q_1-1)\bar{\rho}} \bar{\rho}^{p-1} d\bar{\rho} \quad (22a)$$

and for  $V_E > U_{1,2}/\sin \theta_W$

$$\begin{aligned} \eta_e = & Br_b c_{e1} V_e^{q_1-3} \left[ \frac{\sin^{q_1} \theta_W (\tan^2 \theta_W - \tan^2 \theta_C)}{6 \sin^2 \theta_C \tan^3 \theta_C} \right] \int_{\bar{\rho}=\bar{\rho}_{1,2}}^1 e^{-(B/2)(q_1-1)\bar{\rho}} \bar{\rho}^{p-1} d\bar{\rho} \\ & + Br_b c_{e2} V_e^{q_2-3} \left[ \frac{\sin^{q_2} \theta_W (\tan^2 \theta_W - \tan^2 \theta_C)}{6 \sin^2 \theta_C \tan^3 \theta_C} \right] \int_{\bar{\rho}=0}^{\bar{\rho}=\bar{\rho}_{1,2}} e^{-(B/2)(q_2-1)\bar{\rho}} \bar{\rho}^{p-1} d\bar{\rho} \end{aligned} \quad (22b)$$

where

$$\left. \begin{aligned} \rho_{1,2} &= \frac{2}{B} \ln \left( \frac{V_E \sin \theta_W}{U_{1,2}} \right) \\ c_{e1} &= \frac{c_{e1}}{\rho_0} = 5.012 \times 10^{-49} \frac{m^2}{sec^3} \left( \frac{sec}{m} \right)^{15.45} \\ c_{e2} &= \frac{c_{e2}}{\rho_0} = 5.318 \times 10^{-6} \frac{m^2}{sec^3} \left( \frac{sec}{m} \right)^{5.05} \end{aligned} \right\} \quad (23)$$

Details of the integrations of equations (22a) and (22b) are given in appendix B. The solution may be given in the form

$$\eta_e = \frac{r_b \psi_e Z_e}{B^{0.8}} \quad (24)$$

wherein  $\psi_e$  is a function of  $\theta_C$  (see appendix B and table I) and  $Z_e$  is a function of  $V_e \sin \theta_W$  (see appendix B and table II).

### Nonequilibrium Radiative Heating

For the purposes of this analysis it has been supposed that the portion of the shock layer which is not in thermodynamic and chemical equilibrium is confined to a region so close to the bow shock wave that it may be considered to originate at and be proportional to the area of the bow shock wave. In addition, the nonequilibrium radiation process is regarded as one involving binary collisions so that the radiation is independent of air density until "collision

limiting" occurs (see ref. 10 and appendix C) and is a function only of the velocity normal to the shock wave (see eq. (15)). Collision limiting is presumed to begin when  $\bar{\rho} = \bar{\rho}_{cl}$ , and in the regime for which  $\bar{\rho} < \bar{\rho}_{cl}$  the nonequilibrium radiation is considered to vary directly with density. When the free-molecular flow regime is reached (i.e., when  $\bar{\rho} < \bar{\rho}_{fm}$ ), this radiation is set to be zero. Thus, the time rate of nonequilibrium radiation per unit area of bow shock wave is given as

$$\frac{d\dot{E}_n}{da} = C_n U^s ; \quad \bar{\rho} > \bar{\rho}_{cl} \quad (25a)$$

$$\frac{d\dot{E}_n}{da} = \frac{C_n}{\bar{\rho}_{cl}} \bar{\rho} U^s ; \quad \bar{\rho}_{cl} > \bar{\rho} > \bar{\rho}_{fm} \quad (25b)$$

$$\frac{d\dot{E}_n}{da} = 0 ; \quad \bar{\rho} < \bar{\rho}_{fm} \quad (25c)$$

An examination of the available data indicated (see appendix C) that

$$\left. \begin{aligned} C_n &= 0.74 \times 10^{-22} \text{ sec}^4/\text{m}^4 \\ s &= 7 \\ \bar{\rho}_{cl} &= 10^{-3} \end{aligned} \right\} \quad (26)$$

The total time rate of radiation from the gas cap which is not in equilibrium is then

$$\dot{E}_n = \frac{d\dot{E}_n}{da} a \quad (27)$$

and only half of this radiation is received at the vehicle surface if the surface reflectivity is zero. Then the nonequilibrium radiative heat-transfer coefficient is

$$C_{H_n} = \frac{(1/2)\dot{E}_n}{(1/2)\rho V^3 A} = \frac{(d\dot{E}_n/da)a}{\rho_0 \bar{\rho} V^3 A} \quad (28)$$

where

$$\left. \begin{aligned} a &= \pi r_b^2 \left( \frac{\tan^2 \theta_W}{\sin \theta_W \tan^2 \theta_C} \right) \\ A &= \pi r_b^2 \\ \rho_O &= 1.225 \text{ kg/m}^3 \end{aligned} \right\} \quad (29)$$

while, again,

so that from equations (25), (8), and (14), equation (12) becomes

$$\begin{aligned} \eta_n &= B c_n V_E^{s-3} \left( \frac{\sin^{s-1} \theta_W \tan^2 \theta_W}{2 \sin^2 \theta_C \tan^2 \theta_C} \right) \left[ \int_{\bar{\rho}=\bar{\rho}_{cl}}^1 e^{-(B/2)(s-1)\bar{\rho}} \frac{d\bar{\rho}}{\bar{\rho}} \right. \\ &\quad \left. + \frac{1}{\bar{\rho}_{cl}} \int_{\bar{\rho}=\bar{\rho}_{fm}}^{\bar{\rho}_{cl}} e^{-(B/2)(s-1)\bar{\rho}} d\bar{\rho} \right] \end{aligned} \quad (30)$$

where

$$c_n = \frac{C_n}{\rho_O} = 0.60 \times 10^{-22} \text{ sec}^4/\text{m}^4 \quad (31)$$

Details of the integration of equation (30) are given in appendix C. The solution may be given in the form

$$\eta_n = \Psi_n \Phi_n \left( \frac{V_E}{10^4} \right)^4 \quad (32)$$

where  $\Psi_n$  is a function of  $\theta_C$  (see appendix C and table I) and  $\Phi_n$  is a function of  $B$  (see appendix C and table III).

#### Laminar Convective Heat Transfer

Calculation of the laminar convective heat-transfer coefficients as a function of velocity, air density, and cone angle was made by the procedure given in appendix D. In the absence of ablation it is indicated that the heat-transfer coefficient may be expressed as (sub zero indicates no ablation)

$$C_{H_{lO}} = \frac{c_l}{V^j \sqrt{\bar{\rho} r_b}} \quad (33)$$

where  $c_l$  and  $j$  are functions of the velocity  $V$ . When vapor ablation occurs, the vapor layer fends off the air and so reduces the convective heating. It is assumed in this analysis that for ablation (twelfth assumption)

$$C_{H_l} = \left( \frac{1 - \sigma_l}{1 + K_l V^2} + \sigma_l \right) C_{H_{l0}} \quad (34)$$

where  $\sigma_l$  is an asymptotic lower limit when

$$K_l V^2 \rightarrow \infty \quad (35)$$

and  $K_l$  is a constant depending upon the ablative material and can be defined as

$$K_l = \frac{\alpha_l}{\xi} \quad (36)$$

wherein  $\alpha_l$  depends upon the molecular weight of the ablating vapors<sup>3</sup> and  $\xi$  is the heat energy per unit mass (expressed in kinetic energy units of square of velocity) required to heat the ablator from the cold state through vaporization.

As an approximation for speeds up to 13,000 m/sec, the variable  $c_l$  and the  $j$  values may be replaced by the constants (see appendix D)

$$\left. \begin{aligned} c_l &= c_{l1} = 3.5 \times 10^{-4} \sqrt{\sin 2\theta_C}, \text{ m}^{1/2} \\ j_1 &= 0 \end{aligned} \right\} \quad (37)$$

and at speeds above 26,000 m/sec, the variables can be approximated by the constants

$$\left. \begin{aligned} c_l &= c_{l2} = 19.8 \sqrt{\sin 2\theta_C}, \text{ m}^{1/2} \left( \frac{\text{m}}{\text{sec}} \right)^{1.17} \\ j_2 &= 1.17 \end{aligned} \right\} \quad (38)$$

The foregoing applies in a continuum flow regime. In the free-molecular flow regime, the fraction of the total kinetic energy which, converted to heat, appears as heat to the vehicle is assumed to be one-half (ref. 15); that is to say, in the free-molecular flow regime

$$C_{H_l} = \frac{C_D}{2} \quad (39)$$

---

<sup>3</sup>The value of  $\alpha_l$  is  $1/2 \beta_L$  as defined in reference 14.

Of course the continuum results (eqs. (33) and (34)) only apply when the Knudsen number (ratio of air mean free path to body diameter) is very small compared to unity; conversely, the free-molecular result (eq. (39)) only applies when the Knudsen number is very large compared to unity. A transition from one regime to the other occurs when the Knudsen number is of order unity. Experiment has indicated that the transition from one regime to the other is smooth (see, e.g., ref. 16). For the present calculations it was deemed adequate to consider that the continuum result applied at all air densities for which

$$C_{H_L} = \left( \frac{1 - \sigma_L}{1 + K_L V^2} + \sigma_L \right) \frac{c_L}{V^j \sqrt{\bar{\rho}} r_b} \leq \frac{C_D}{2} = \sin^2 \theta_C \quad (40)$$

Within the free-molecular flow range, for the sizes and masses of entry vehicles of interest in this analysis, the velocity can safely be taken to be the entry velocity,  $V_E$ . Thus the continuum flow results will be applied for all air density ratios greater than

$$\bar{\rho}_{fm} = \left[ \left( \frac{1 - \sigma_L}{1 + \xi_L} + \sigma_L \right) \frac{c_L}{V_E^j \sqrt{r_b} \sin^2 \theta_C} \right]^2 \quad (41)$$

with

$$\xi_L = K_L V_E^2 \quad (42)$$

and in the free-molecular flow range we take

$$C_{H_L} = \frac{C_D}{2} = \sin^2 \theta_C ; \quad \bar{\rho} < \bar{\rho}_{fm} \quad (43)$$

Finally, then, the laminar convective energy fraction may be written

$$\begin{aligned} \eta_L = & \frac{B c_L (1 - \sigma_L)}{2 V_E^j \sqrt{r_b} \sin^2 \theta_C} \int_{\bar{\rho}_{fm}}^1 \frac{e^{-B[1-(j/2)]\bar{\rho}} d\bar{\rho}}{(1 + \xi_L e^{-B\bar{\rho}}) \sqrt{\bar{\rho}}} \\ & + \frac{B c_L \sigma_L}{2 V_E^j \sqrt{r_b} \sin^2 \theta_C} \int_{\bar{\rho}_{fm}}^1 \frac{e^{-B[1-(j/2)]\bar{\rho}} d\bar{\rho}}{\sqrt{\bar{\rho}}} + \frac{B}{2} \int_0^{\bar{\rho}_{fm}} e^{-B\bar{\rho}} d\bar{\rho} \end{aligned} \quad (44)$$

It is shown in appendix D that the solution of equation (44) for the entry speed range up to 13,000 m/sec may be given as

$$\eta_l = \eta_{l_1} = \Psi_{l_1} \sqrt{\frac{B}{r_b}} [(1 - \sigma_l) \Omega_{l_1} + 1.772 \sigma_l - \Phi_{l_1}] - 2 \Psi_{l_1}^2 \left( \frac{B}{r_b} \right) \left( \frac{1 - \sigma_l}{1 + \xi_l} + \sigma_l \right)^2 \quad (45)$$

and, for the entry speed range above 26,000 m/sec, as

$$\begin{aligned} \eta_l = \eta_{l_2} = & \frac{\Psi_{l_2}}{(V_E/10^4)^{1.17}} \sqrt{\frac{B}{r_b}} [(1 - \sigma_l) \Omega_{l_2} + 2.748 \sigma_l - \Phi_{l_2}] \\ & - 2 \frac{\Psi_{l_2}^2}{(V_E/10^4)^{2.34}} \left( \frac{B}{r_b} \right) \left( \frac{1 - \sigma_l}{1 + \xi_l} + \sigma_l \right)^2 \end{aligned} \quad (46)$$

where

$\Psi_{l_1}, \Psi_{l_2}$  functions of  $\theta_C$  (see appendix D and table I)

$\Omega_{l_1}, \Omega_{l_2}$  functions of  $\xi_l$  (see appendix D and table IV)

$\Phi_{l_1}, \Phi_{l_2}$  functions of  $B$  (see appendix D and table III)

For speeds between 13,000 and 26,000 m/sec the values of  $\eta_l$  are assumed to change smoothly from the first range to the second, and the following applies:

Define

$$\left. \begin{aligned} G_1 &= \eta_{l_1} \text{ at } V_E = 13,000 \text{ m/sec} \\ G_2 &= \eta_{l_2} \text{ at } V_E = 26,000 \text{ m/sec} \\ G_3 &= (\eta_{l_1} \text{ at } V_E = 13,000 \text{ m/sec}) - (\eta_{l_1} \text{ at } V_E = 12,000 \text{ m/sec}) \\ G_4 &= (\eta_{l_2} \text{ at } V_E = 27,000 \text{ m/sec}) - (\eta_{l_2} \text{ at } V_E = 26,000 \text{ m/sec}) \end{aligned} \right\} \quad (47)$$

Then calculate

$$\left. \begin{aligned} b_0 &= G_1 + 5(G_2 - G_1) - 52G_3 - 26G_4 \\ b_1 &= - \left( \frac{120}{13} \right) (G_2 - G_1) + 80G_3 + 50G_4 \\ b_2 &= \left( \frac{900}{169} \right) (G_2 - G_1) - \left( \frac{500}{13} \right) G_3 - \left( \frac{400}{13} \right) G_4 \\ b_3 &= - \left( \frac{2000}{2197} \right) (G_2 - G_1) + \left( \frac{1000}{169} \right) G_3 + \left( \frac{1000}{169} \right) G_4 \end{aligned} \right\} \quad (48)$$

so that for the speed range  $13,000 \text{ m/sec} < V_E < 26,000 \text{ m/sec}$

$$\eta_l = \eta_{l_{1-2}} = b_0 + b_1 \left( \frac{V_E}{10^4} \right) + b_2 \left( \frac{V_E}{10^4} \right)^2 + b_3 \left( \frac{V_E}{10^4} \right)^3 \quad (49)$$

### Turbulent Convective Heat Transfer

The analysis of appendix E shows that in the absence of ablation the turbulent heat-transfer coefficient can be expressed with reasonable accuracy by

$$C_{H_{t_0}} = \frac{\theta_C \cos \theta_C}{\sin^k \theta_W \sin \theta_C} \left( \frac{c_t}{V^{k_0} r_b^{0.204} r_b^{0.148}} \right) \quad (50)$$

for  $\theta_C$  expressed in degrees of arc and,

for  $V \sin \theta_W \leq 7,500 \text{ m/sec}$

$$\left. \begin{aligned} c_t &= c_{t_1} = 8.80 \times 10^{-7} \text{ m}^{0.148} (\text{deg})^{-1} (\text{m/sec})^{-0.66} \\ k &= k_1 = -0.66 \end{aligned} \right\} \quad (51a)$$

and for  $V \sin \theta_W \geq 7,500 \text{ m/sec}$

$$\left. \begin{aligned} c_t &= c_{t_2} = 1.35 \times 10^{-3} \text{ m}^{0.148} (\text{deg})^{-1} (\text{m/sec})^{0.16} \\ k &= k_2 = 0.16 \end{aligned} \right\} \quad (51b)$$

The effect of vapor ablation to reduce the turbulent convective heat transfer can be assumed in the form (twelfth assumption)

$$\left. \begin{aligned} C_{H_t} &= \left( \frac{1 - \sigma_t}{1 + K_t V^2} + \sigma_t \right) C_{H_{t_0}} \\ K_t &= \frac{\alpha_t}{\xi} \end{aligned} \right\} \quad (52)$$

wherein  $\alpha_t$  depends upon the molecular weight of the ablating vapors.<sup>4</sup>

---

<sup>4</sup>The value of  $\alpha_t = 1/2 \beta_t$  as defined in reference 14. As suggested in the reference, we shall use  $\alpha_t = 1/3 \alpha_l$  in this report.



As in the case of laminar flow, one properly should consider separately the free-molecular flow regime. However, the interesting turbulent flow cases are those for which  $B$  is small (no more than a few hundred at most). With this restriction the presumption that the continuum regime extends up to entry conditions ( $\bar{\rho} = 0$ ) in calculating the heat transfer leads to negligible error.

Then equation (12) gives for

$$V_E \leq \frac{7500}{\sin \theta_W} \text{ m/sec}$$

$$\eta_t = \frac{Bc_{t1}}{V_E^{k_1} r_b^{0.148}} \left( \frac{\theta_C \cos \theta_C}{2 \sin^{k_1} \theta_W \sin^3 \theta_C} \right) \int_{\bar{\rho}=0}^1 \left( \frac{1 - \sigma_t}{1 + \xi_t e^{-B\bar{\rho}}} + \sigma_t \right) \frac{e^{-B\left(1+\frac{k_1}{2}\right)\bar{\rho}}}{\bar{\rho}^{0.204}} d\bar{\rho} \quad (53a)$$

while for

$$V_E \geq \frac{7500}{\sin \theta_W} \text{ m/sec}$$

$$\begin{aligned} \eta_t = & \frac{Bc_{t1}}{V_E^{k_1} r_b^{0.148}} \left( \frac{\theta_C \cos \theta_C}{2 \sin^{k_1} \theta_W \sin^3 \theta_C} \right) \int_{\bar{\rho}=\frac{2}{B} \ln \left( \frac{V_E \sin \theta_W}{7500} \right)}^1 \left( \frac{1 - \sigma_t}{1 + \xi_t e^{-B\bar{\rho}}} + \sigma_t \right) \frac{e^{-B\left(1+\frac{k_1}{2}\right)\bar{\rho}}}{\bar{\rho}^{0.204}} d\bar{\rho} \\ & + \frac{Bc_{t2}}{V_E^{k_2} r_b^{0.148}} \left( \frac{\theta_C \cos \theta_C}{2 \sin^{k_2} \theta_W \sin^3 \theta_C} \right) \int_{\bar{\rho}=0}^{\frac{2}{B} \ln \left( \frac{V_E \sin \theta_W}{7500} \right)} \left( \frac{1 - \sigma_t}{1 + \xi_t e^{-B\bar{\rho}}} + \sigma_t \right) \frac{e^{-B\left(1+\frac{k_2}{2}\right)\bar{\rho}}}{\bar{\rho}^{0.204}} d\bar{\rho} \end{aligned} \quad (53b)$$

wherein

$$\xi_t = K_t V_E^2 \quad (54)$$

It is shown in appendix E that the energy fraction may be given in the form

$$\eta_t = \frac{B^{0.204}}{r_b^{0.148}} \left[ \Lambda_t - \Phi_t \Psi_t \left( \frac{V_E}{10^4} \right)^{0.66} \right] \quad (55)$$

wherein  $\Psi_t$  is a function of  $\theta_C$  (see appendix E and table I),  $\Phi_t$  is a function of  $B$  (see appendix E and table III), and, for given values of  $\sigma_t$  and  $K_t$ ,  $\Lambda_t$  is a function of both  $V_E$  and  $\theta_C$  (see appendix E and table V). The second term in equation (55) will only be important when the ballistic parameter,  $B$ , is very small.

## RESULTS

The analysis of the preceding section was used to compute by IBM 7090 the heat-transfer characteristics of conical entry vehicles entering the Earth's atmosphere. Since the analysis requires attached bow shock waves which limit the maximum cone half-angle to about  $55^\circ$ , results at larger angles are shown by dotted curves in all the figures to follow. The calculations have been carried out for a 1-meter base radius. In one case the heat shield was assumed to be composed of a low temperature ablator having the assumed characteristics of subliming Teflon, and a high temperature ablator having the assumed characteristics of vaporizing quartz. For the Teflon the characteristics assumed are

$$\left. \begin{aligned} \zeta &= 2.2 \times 10^6 \text{ m}^2/\text{sec}^2 \\ K_l &= 12 \times 10^{-8} \text{ sec}^2/\text{m}^2 \text{ (for } \alpha_l = 0.26) \\ K_t &= 4 \times 10^{-8} \text{ sec}^2/\text{m}^2 \text{ (for } \alpha_t = 0.09) \\ \sigma_l &= \sigma_t = 0.1 \end{aligned} \right\} \quad (56)$$

For the quartz the characteristics assumed are

$$\left. \begin{aligned} \zeta &= 16 \times 10^6 \text{ m}^2/\text{sec}^2 \\ K_l &= 1.5 \times 10^{-8} \text{ sec}^2/\text{m}^2 \text{ (for } \alpha_l = 0.24) \\ K_t &= 0.5 \times 10^{-8} \text{ sec}^2/\text{m}^2 \text{ (for } \alpha_t = 0.08) \\ \sigma_l &= \sigma_t = 0.1 \end{aligned} \right\} \quad (57)$$

The choices of  $\alpha_l$ ,  $\alpha_t$ , and  $\zeta$  were based upon available literature (e.g., refs. 14 and 17). The choices for  $\sigma_l$  and  $\sigma_t$  are based on the knowledge from experiments with Teflon (ref. 18) that the asymptote is not zero (as predicted by the usual theories). The asymptotic value is probably a function of molecular weight and thermal conductivity at least, and is probably different for laminar and turbulent flow. Values from experiment range from 0.05 to 0.2. The choice of 0.1 is an arbitrary one.

### Laminar Flow

The analysis for all laminar flow during vehicle descent (excepting free-molecule flow at entry) is probably restricted to those cases for which the maximum Reynolds number does not reach too large values. This condition is only fulfilled for the larger values of the ballistic parameter ( $B$  of the order of hundreds or thousands) and the results presented are so restricted. It is well to treat, first, a single case to illustrate the typical effect of increasing entry speed on the variation of the contribution of radiative and convective

heating to the total. Such an example is given in figure 3 for which the entry body has a cone half-angle of  $30^\circ$ , a ballistic parameter of 200, and a Teflon head shield. At low entry speeds the convective transfer dominates and in this range the total energy fraction falls with increase in entry speed because (eq. (34)) the effectiveness of ablation to reduce the convective heat-transfer rate is assumed to improve with increasing speed and because  $\text{CH}_2\text{O}$  diminishes (above 10 km/sec) with increasing speed. At the higher entry speeds, the radiative heating rises rapidly with speed so that the total energy fraction exhibits a minimum. Note that the contribution of the nonequilibrium radiation to the total energy fraction is very small and could well be ignored. This observation applies generally to all cases of interest.

Consider next the more general case wherein the ballistic parameter is fixed but we vary the cone half-angle over a wide range. The energy fractions as a function of entry speed are then typically those shown in figure 4 for, again, a ballistic parameter of 200 and a Teflon heat shield. The envelope values giving the minimum energy fraction as a function of entry speed are shown by the dashed curve.

If now we consider various values of  $B$  appropriate to laminar flow, we can determine a series of envelope curves. Such envelopes are shown in figure 5(a) for a Teflon heat shield and in figure 5(b) for a vaporizing quartz heat shield. It is seen that, at any entry speed, lowering the ballistic coefficient diminishes the energy fraction.

#### Turbulent Flow

The analysis for the turbulent flow case made no allowance for any laminar flow which is, of course, unrealistic. However, it is expected that the errors resulting from failure to allow for any laminar flow will be unimportant if the maximum Reynolds number occurring during the flight trajectory is very high. Thus we can presume that the "all turbulent" results will be realistic if the ballistic parameter is small - say of the order of 20 or less - but will be in error by unknown magnitudes for larger values. Accordingly, the results presented are restricted to the smaller ballistic parameters. As for the laminar case it is well, first, to illustrate the typical effect of increasing entry speed on the variations of the contribution of radiative and convective heating to the total. Such an example is given in figure 6 for which the entry body has a cone half-angle of  $30^\circ$ , a ballistic parameter of 20, and a Teflon heat shield. The variation of the energy function with entry speed is seen to be similar to that for the laminar flow case (fig. 3) and for the same reasons. Again, it should be noted that the contribution of nonequilibrium radiation to the total is very small and could well be ignored. As for the laminar case, this observation applies generally to all cases of interest.

Consider, next, the more general case wherein the ballistic parameter is fixed but we vary the cone half-angle over a wide range. The energy fractions as a function of entry speed are typically those shown in figure 7 for a

ballistic parameter of 20 and a Teflon heat shield. As before, the envelope values are given by the dashed curve.

If, now, we consider various values of  $B$  which may be appropriate to turbulent flow, we can determine a series of envelope curves. Such envelopes are shown in figure 8(a) for a Teflon heat shield and in figure 8(b) for a vaporizing quartz heat shield. It is seen that at any entry speed, the energy fraction is again diminished by lowering the ballistic coefficient.

## DISCUSSION

In the following, the salient features of the results for the laminar and turbulent flow cases are considered separately and then compared. Finally, the important assumptions made in the analysis are reviewed to assess their adequacy.

### Laminar Flow

In figures 5(a) and 5(b) it is clear that the least energy fraction is obtained by making the ballistic parameter as small as possible. Since the maximum flight Reynolds number varies inversely with the ballistic parameter (see appendix F) and since there is probably an upper limit to the Reynolds number which one can allow and still enjoy laminar flow for the whole of the trajectory, then it follows that there is some minimum ballistic parameter at any given entry speed which can be permitted if the assumption of laminar flow over the whole trajectory is to apply.

At lower supersonic speeds than we consider here, there is some support for the contention that there is some limiting Reynolds number (denoted hereinafter as  $Re_{lim}$ ) above which one cannot expect to maintain laminar flow. It is probable that in this high-speed region  $Re_{lim}$  varies with free-stream enthalpy and with the composition of the ablation material.<sup>5</sup>

We have assumed from experience with nonablating surfaces at lower speeds that a maximum Reynolds number based on local surface flow conditions of  $10^7$  can be reached before turbulence occurs. However, we will show the effect of increasing or decreasing this limiting Reynolds number by presenting results for limit Reynolds numbers of  $2 \times 10^7$  and  $0.5 \times 10^7$  as well. The analysis of appendix F gives the relation between the cone half-angle, the ballistic parameter, and the entry speed for an arbitrary limit Reynolds number. The optimum values of ballistic

---

<sup>5</sup>Not only is it probable that this limiting Reynolds number will be influenced by the molecular weight of the ablated vapor but it is most likely to depend upon the uniformity of the ablative process. For example, one expects a composite ablator, such as a plastic impregnated fibrous material or a charring ablator, by virtue of the jet-like injection of vapor from such a surface, to behave differently than some ablator such as uniform Teflon which should be free of such jetting.

parameter, cone half-angle, and energy fraction as a function of entry speed were found in the following way: For a series of entry speeds,  $V_E$ , base radii,  $r_b$ , ablation asymptotes,  $\sigma_l$ , and ablation constants,  $K_l$ , energy fraction,  $\eta$ , was plotted as a function of cone half-angle,  $\theta_C$ , for various values of the ballistic parameter,  $B$ . (An example is shown by the solid curves in fig. 9.) On these same plots the values of  $B$  and  $\theta_C$  corresponding to limit Reynolds numbers of  $0.5 \times 10^7$ ,  $10^7$ , and  $2 \times 10^7$  were located and the corresponding curves of  $\eta$  as a function of  $\theta_C$  were constructed from which one can determine the optimum values of energy fraction,  $\eta_{opt}$  and the corresponding values of ballistic parameter,  $B_{opt}$ , and cone angle,  $\theta_{Copt}$ . (For the particular case given in figure 9, these are shown by the dotted curves. The lowest values of  $\eta$  correspond to  $\eta_{opt}$ .) From the total complex of plots, it was then determined that for the range of variables

$$\left. \begin{aligned} 0.5 \times 10^7 &\leq Re_{lim} \leq 2 \times 10^7 \\ 0.2 \text{ m} &\leq r_b \leq 1 \text{ m} \\ 0.05 &\leq \sigma_l \leq 0.2 \\ 2 \times 10^{-8} \frac{\text{sec}^2}{\text{m}^2} &\leq K_l \leq 15 \times 10^{-8} \frac{\text{sec}^2}{\text{m}^2} \end{aligned} \right\} \quad (58)$$

the optimum could be expressed approximately by

$$\eta_{opt} = \bar{\eta}_{opt} (Re_{lim} \times 10^{-7})^{-0.281} r_b^{0.044} (10\sigma_l)^{0.310} (K_l \times 10^8)^{-0.276} \quad (59)$$

$$\theta_{Copt} = \bar{\theta}_{Copt} (Re_{lim} \times 10^{-7})^{-0.088} r_b^{-0.017} (10\sigma_l)^{0.020} (K_l \times 10^8)^{-0.028} \quad (60)$$

$$\left(\frac{B}{r_b}\right)_{opt} = \left(\frac{\bar{B}}{r_b}\right)_{opt} (Re_{lim} \times 10^{-7})^{-0.881} r_b^{0.041} (10\sigma_l)^{-0.033} (K_l \times 10^8)^{0.035} \quad (61)$$

where the values of  $\bar{\eta}_{opt}$ ,  $\bar{\theta}_{Copt}$ , and  $(\bar{B}/r_b)_{opt}$  are the functions of entry speed given in figure 10 and correspond by definition to values of  $\eta_{opt}$ ,  $\theta_{Copt}$ , and  $(B/r_b)_{opt}$  when

$$\left. \begin{aligned} Re_{lim} &= 10^7 \\ r_b &= 1 \text{ m} \\ \sigma_l &= 0.1 \\ K_l &= 10^{-8} \text{ sec}^2/\text{m}^2 \end{aligned} \right\} \quad (62)$$

A fact of considerable importance is that when the energy fraction is optimum, the convective contribution is the principal part of the total, approximately  $0.87 \pm 0.02$ . Thus it is important to know the convective contributions with an order of magnitude greater accuracy than the equilibrium radiation. The nonequilibrium radiation is, as noted earlier, a trivial contribution to the total. Other points to note about these optima are the following:

(1) The optimum energy fraction is insensitive to the vehicle size ( $r_b$ ) and can be approximately given as

$$\eta_{\text{opt}} \approx \bar{\eta}_{\text{opt}} \left( \frac{\sigma_l}{K_l \text{Re}_{\text{lim}}} \right)^{0.3} = \bar{\eta}_{\text{opt}} \left( \frac{\sigma_l \zeta}{\alpha_l \text{Re}_{\text{lim}}} \right)^{0.3} \quad (63)$$

so that other factors being equal the optimum energy fraction is unfavorably affected by improvement in the heat of ablation as shown in figure 11, as would be expected (eqs. (34) and (36)).

The optimum mass loss ratio is given (eq. (13)) by the approximation

$$\left( \frac{\Delta m}{m} \right)_{\text{opt}} = \eta_{\text{opt}} \frac{V_E^2}{2\zeta} \approx \frac{\bar{\eta}_{\text{opt}} V_E^2}{2} \left( \frac{\sigma_l}{\alpha_l \text{Re}_{\text{lim}}} \right)^{0.3} \zeta^{-0.7} \quad (64)$$

The parameter

$$\left( \frac{\Delta m}{m} \right)_{\text{opt}} \left( \frac{\alpha_l \text{Re}_{\text{lim}}}{\sigma_l} \right)^{0.3} \zeta^{0.7} \approx \frac{\bar{\eta}_{\text{opt}}}{2} V_E^2 \quad (65)$$

is plotted in figure 12 as a function of  $V_E$ .

From the foregoing it is seen that although vaporizing quartz, a high-temperature ablator, has a heat of ablation about eight times that for Teflon, a low-temperature ablator, the mass loss for quartz is only about one-fourth that for Teflon. These materials are compared in figure 13 wherein a limit Reynolds number of  $10^7$  is assumed. Note that at the optimum conditions one can keep the mass loss to the order of 10 percent or less for speeds well in excess of escape speed.

(2) With reference to the optimum cone half-angle, we note that it is essentially independent of all factors except the entry speed and that

$$\theta_{\text{Copt}} \approx \bar{\theta}_{\text{Copt}} \quad (66)$$

As seen in figure 10, then, the optimum conical bodies are not slender ones. Even at an entry speed of 30 km/sec, the optimum cone half-angle is  $25^\circ$  of arc.

(3) Concerning the optimum ballistic parameter we note that it varies almost directly with the base radius, nearly inversely with the limiting Reynolds number, and is essentially independent of other factors except entry speed. Thus

$$\left(\frac{B}{r_b}\right)_{\text{opt}} \approx \left(\frac{\bar{B}}{r_b}\right)_{\text{opt}} (\text{Re}_{\text{lim}} \times 10^{-7})^{-0.9} \quad (67)$$

The fact that  $B/r_b$  appears as the basic variable should not be surprising. As noted earlier nonequilibrium radiation is a trivial contributor to the total heating. Equilibrium radiation (eq. (24)) variation is

$$\eta_e \sim \frac{r_b}{B^{0.8}} \approx \left(\frac{B}{r_b}\right)^{-0.8} \quad (68)$$

while laminar convection (eq. (45) or (46)) is directly determined by  $B/r_b$ .

With reference to the  $(B/r_b)_{\text{opt}}$ , there are some important connotations to be made regarding trajectory angles. Since

$$B_{\text{opt}} = \left(\frac{C_D \rho_o A}{\beta_m \sin \gamma}\right)_{\text{opt}} = \frac{2 \rho_o A \sin^2 \theta_{C_{\text{opt}}}}{\beta_m \sin \gamma} \quad (69)$$

and since

$$\theta_{C_{\text{opt}}} \approx \bar{\theta}_{C_{\text{opt}}} \quad (70)$$

while

$$m \approx \frac{\pi r_b^3 \rho_b}{3 \tan \bar{\theta}_{C_{\text{opt}}}} \quad (71)$$

where  $\rho_b$  is the average density of the entry body, then for

$$\left. \begin{aligned} \rho_o &= 1.225 \text{ kg/m}^3 \\ \beta &= \frac{1}{7000} \text{ m}^{-1} \end{aligned} \right\} \quad (72)$$

we get

$$\left(\frac{B}{r_b}\right)_{\text{opt}} \approx 5.2 \times 10^4 \frac{\sin^2 \bar{\theta}_{C_{\text{opt}}} \tan \bar{\theta}_{C_{\text{opt}}}}{\rho_b r_b^2 \sin \gamma} \quad (73)$$

or, at optimum,

$$\rho_b r_b^2 \sin \gamma \approx 5.2 \times 10^4 \left[ \frac{\sin^2 \theta_{Copt} \tan \theta_{Copt}}{(\bar{B}/r_b)_{opt}} \right] (Re_{lim} \times 10^{-7})^{0.9} \quad (74)$$

and the right side of this expression is a function only of the entry velocity and Reynolds number limit. The relation is shown in figure 14. Let us now review values of the product  $\rho_b r_b^2 \sin \gamma$  which are typical of entry vehicles.

For current manned vehicles the order of values for density, base radius, and trajectory angle is

$$\left. \begin{aligned} \rho_b &\approx 250 \text{ kg/m}^3 \\ r_b &\approx 1 \text{ m} \\ \sin \gamma &\approx 0.06 \end{aligned} \right\} \quad (75)$$

so that

$$\rho_b r_b^2 \sin \gamma \approx 15 \text{ kg/m} \quad (76)$$

so that one expects that over the likely range of entry speeds permitted by entry load considerations - say, less than 20 km/sec (see ref. 2) - there may not be difficulty in maintaining laminar flow in the boundary layers. Of course, the small values of  $\gamma$  which are required from load considerations demand the use of lift in order to hold the vehicle in an earth curvature flight path. Half-cone bodies (see, e.g., ref. 19) suggest themselves for such applications. Moreover, it should be noted that the analysis given herein for the aerodynamic heating of conical bodies is predicated upon the assumption of constant  $\gamma$  trajectories and, hence, can only be considered a crude approximation for shallow-angle entries.

For unmanned space probes the vehicle density will be about that for manned vehicles but the size will generally be less (say,  $r_b = 0.5$  m), and the vehicle load consideration will usually permit steep descent (i.e.,  $\sin \gamma$  up to unity). Steep descent removes the necessity for employing lift during entry while freedom in the choice of  $\gamma$  may greatly ease the guidance problem prior to entry. However, if we intend to maintain laminar flow over such vehicles, we may be forced to resort to flat trajectories except for low entry speeds, as seen by the results shown on figure 15 which give the maximum entry angle as a function of entry speed for typical vehicle quantities ( $\rho_b = 250 \text{ kg/m}^3$ ,  $r_b = 0.5$  m). As vehicle size increases, the probable trend with time, the choice of entry angle can become even more stringent. Thus, even for instrument probes, we may desire flat trajectories at the higher speeds - but not because of load restrictions. It must be remembered, however, that these conclusions are based upon the dubious assumption that the maximum Reynolds number permitted for laminar flow is of the order of  $10^7$ . The need for high-speed laminar-flow research is clearly evident.



## Turbulent Flow

As for laminar flow if one is to minimize the energy fraction one must employ the lowest ballistic parameter that can be permitted, particularly at the higher speeds (see figs. 8(a) and 8(b)). However, it should be noted at the outset that one cannot indefinitely reduce the ballistic parameter and still recover the vehicle intact. In the absence of auxiliary drag devices (drag brakes, parachutes, etc.) for terminal deceleration, the impact speed (see eq. (8)) is

$$V_0 = V_E e^{-B/2} \quad (77)$$

so that values of  $B$  upward of 10 must be set as a lower limit. With auxiliary drag devices, this lower limit might perhaps be halved. Even at these very low values of the ballistic parameter the turbulent energy fractions (see figs. 8(a) and 8(b)) are not as low as can be attained with laminar flow for limit Reynolds numbers of the order of  $10^7$ . For the turbulent case, as for the laminar, when conditions are optimum, the convective heating is the dominant contribution to the energy fraction. Again, the optimum cone half-angles are not small even at very high speeds.

In comparing the optimum energy fractions for turbulent flow with laminar flow it should be noted that the turbulent values are an order of magnitude higher (the ordinates of figs. 8(a) and 8(b) are expressed in percent while those of figs. 5(a) and 5(b) are tenths of percent). This disparity is forcefully demonstrated in figure 16 wherein for three entry speeds, optimum energy fraction is plotted as a function of the ballistic parameter. (Note the lower ends of the laminar curves represent a Reynolds number limit of  $10^7$  and that the dotted curves are arbitrary fairings to indicate how the turbulent and laminar might join.) It is clear that laminar flow is to be sought even if the limit Reynolds numbers are low. Figure 17 shows the corresponding variations of optimum cone half-angles with entry speed and ballistic parameter and again emphasizes that the optimum angle is only, in essence, dependent on velocity.

## Review of Assumptions

In the analytical development many assumptions were made. While a number of these are clearly valid approximations there are many that should be reviewed to ascertain, in retrospect, their adequacy. Discussion of them is given in the following:

(1) The assumption that flight path angle is constant, which was made for the purpose of simplifying the analysis, is generally admissible when the entry trajectory is steep (see ref. 12). However, for manned vehicles and for high-speed probes which may enjoy laminar flow the assumption is not strictly admissible so that this restriction must be borne in mind in interpreting the results which have been given. In any event the restriction does not invalidate the conclusions when considered in a comparative sense.

(2) The assumption that the drag coefficient is constant demands that the body not be slender and that no shape change occur during entry. We have already seen that optimum bodies are, in fact, not slender so that from this aspect the assumption is valid. However, the process of ablation will tend to promote a shape change which, as will be shown later, can and must be minimized so that the assumption is therefore valid with this restriction.

(3) The assumption that ablation is either by sublimation or vaporization of the surface is generally an acceptable one for low-temperature ablators but can be seriously in error for high-temperature ablators. Quartz, for example, would experience considerable ablation in the liquid state unless the heat-transfer rates were very high and of short total duration, as during steep trajectories. Thus the results given for quartz might be appropriate for the turbulent flow cases discussed but surely underestimate energy fraction and mass loss for the laminar ones (see ref. 14 for actual performance of quartz at low heat rates). Finally, it should be noted that for very high heat-transfer rates, there is considerable danger that ablation in the solid state may occur as a result of structural failure due to excessive thermal stress within the ablator. Stony meteoroids commonly experience structural failure during atmosphere entry (see ref. 20 and also ref. 21 for a particularly spectacular example) which may result in part or in whole from excessive thermal stress. Many of the ablative heat shields which have demonstrated excellent performance to date may not fare too well under the more severe service we have considered here.

(4) The assumption is made that the mass lost by ablation during entry is small compared to the entry mass. The results show (fig. 13) that  $\Delta m/m$  smaller than about 0.1 is obtained over a considerable range of entry speeds. For this range the assumption is therefore valid.

(5) The assumption that no cross coupling (ref. 22) of radiative and convective heat transfer occurs will certainly be an acceptable one for the results which have been given for near-optimum cases since, as has been shown, in these cases convective heating dominates. Since the energy loss from the shock layer by radiation is small it cannot have an important effect on the convection. At conditions away from optimum, coupling may become more important, but such conditions are not of interest for the present study.

(6) The assumptions that energy depletion due to radiation is trivial and that no reabsorption of radiation occurs within the gas cap are generally acceptable for the more interesting case considered (i.e., for near-optimum bodies) since the energy fractions are then small.

(7) The assumption that some limiting Reynolds number exists below which one expects laminar flow is open to serious doubt, as has been pointed out earlier. This assumption is based on the experiences obtained from tests at far lower speeds than are considered in this paper. Clearly, some important research can and must be done on the stability of laminar flows at high speeds. A similar comment applies to the assumed formulation (eqs. (34) and (52)) for the ratio of convective transfer in the presence of ablation to that in its absence.

(8) Finally, the assumption that no shape change occurs during entry requires considerable review, for it is in contradiction to the fact that the heat-transfer rate is not uniform over a conical surface during those portions of the trajectory where heating is very important (i.e., in the continuum flow regime). In continuum flow, particularly for the laminar case, the convective heat-transfer rate varies from large values at the apex of a cone to small values at the skirt. Thus the cone tends to be ablated to a round-nosed near-cone with increased cone half-angle. If the entry speed is high, the rounded apex, promoted by the convective heating variation along the cone, becomes flattened by the radiative heating contribution at the lower altitudes. The flattened face now ablates rapidly because of the near-normal shock conditions at the bow, and the mass loss, if the entry speed is high, will be much greater for the ablated shape than it would have been if shape change had been prevented. Thus such adverse changes in body shape must be prevented if the advantages of conical bodies are to be realized. This problem is the subject of the following section.

### The Problem of Shape Change

To illustrate how the shape of an initially conical body changes with time as the result of variations in heat-transfer rate along the surface, a Teflon cone was subjected to laminar convective heating in an arc-jet flow of moderate enthalpy. (The arc-jet flow characteristics and description of the models used in these experiments are given in appendix G.) Photographs of the body initially and at 18 seconds after the establishment of air flow are shown in figure 18. The progression of shape change is shown in figure 19. Flattening does not occur in this experiment because the enthalpy of the stream is not high enough for radiative heating to be significant (the stream enthalpy corresponds to a flight velocity less than 3 km/sec).

If the entry speed of a vehicle is only slightly greater than parabolic speed - say 12 km/sec - the penalty for shape changes similar to the initial changes shown in figure 19 will, at the worst, be small because, as rounding of the apex occurs in an actual flight, the speed diminishes enough that normal shock radiative heating, because of its great sensitivity to speed, will not cause excessive additional ablation.

It is anticipated that such will not be the case if the entry speed is somewhat higher - say 14 km/sec. In this case one might profitably employ a near-conical body having a cusped apex, such as shown in figure 20(a). This shape was formed by adding to the original cone in the axial direction an amount of Teflon very nearly proportional to the inverse square root of the local radius of the cone. Figure 20 corresponds to the  $c = 0.1$  case (see appendix G for shape equation). When this cusped shape was subjected to the heating of the arc jet, the changes in shape with time were those shown by the photographs and the measured ordinates of figures 20 and 21, respectively. One other cusped shape corresponding to  $c = 0.3$  was also tested. The corresponding changes in shape with time are shown by the photographs and measured ordinates of figures 22 and 23. Comparing the ablation of the cusped bodies with the ablation of the cone, one sees that at any given time after the commencement of heating, the nose radius is less

the greater the cusp (i.e., the larger the value of  $c$ ). Thus flight vehicles having such cusped shape might be used for somewhat higher entry speeds than would be tolerable with a cone.

The stratagem of cusping cannot be expected to be a satisfactory solution at entry speeds well in excess of earth parabolic speed. It was reasoned that for such cases one must employ an auxiliary coolant at the apex to prevent drastic shape changes. For example, one might cool the cone by transpiration of a gas through porous walls at the apex (see, e.g., refs. 23 through 25) or by feeding, at an appropriate rate, a fluid or a solid ablator through a hole at the apex. To investigate the performance of such an apex cooling system, the Teflon models shown in figures 24, 25, and 26 were constructed and tested in the arc-jet wind tunnel (see appendix G). The apexes of these models have holes of three different sizes through which Teflon rods of the same diameter as the holes could be fed during the tests. Time-sequence photographs of the models during the tests are shown in figures 27, 29, and 31. The model dimension changes with time and the feed rates for the rods are given in figures 28, 30, and 32. The remarkable fact to note is that this scheme permits the ablation of the conical body to occur with but small change in shape of the cone surface. These tests indicate that such schemes may be very attractive for application to vehicles at high entry speeds. An interesting fact of these particular tests is that the mass of rod fed per unit time was essentially independent of rod diameter. This suggests that only small diameter rods need be used so that the mass penalty due to rod ablation resulting from normal shock radiation at the face of the rod, which varies roughly as the cube of the rod diameter, can be kept small. Of course, it must be noted that the arc-jet test conditions are considerably different from those which would occur in flight and could, therefore, not be representative of high entry velocities. The results are nevertheless encouraging that some solution to the shape-change problem can be effected.

#### CONCLUDING REMARKS

The analyses employed in this study are clearly of an approximate nature so that the results should be regarded as comparative rather than absolute. The results do point up future problems of importance for high-speed entries. Some salient factors to note are the following: Laminar boundary-layer flows on vehicles result in an order of magnitude less mass loss than turbulent flows at reasonable reentry Reynolds numbers. Much research on the stability of laminar flows at hyperbolic entry speeds must be done in this regard. For optimum conical vehicles, convective heat transfer is an order of magnitude more important than radiative heat transfer, so that to properly assess heating problems at high entry speeds, one must determine convective heating with greater accuracy than one need determine the radiative heating. Nonequilibrium radiative heating is a much less important factor than equilibrium radiative heating.

In addition, if the advantages indicated for conical, or near-conical, vehicles for atmosphere entry at the very high speeds considered are to be realized, changes in heat shield shape due to ablation must be controlled in

some manner to prevent the serious nose blunting which would normally occur during entry. This requirement will demand ingenuity in design.

Finally, for some entry trajectories of interest (e.g., steep entries with turbulent boundary-layer flow) heating rates may greatly exceed those we have been accustomed to in the past. Accordingly there is considerable danger that many of the ablative materials usually considered to be attractive may fail structurally because of excessive thermal stress and so be useless for such severe applications.

Ames Research Center  
National Aeronautics and Space Administration  
Moffett Field, Calif., July 12, 1963

## APPENDIX A

### SYMBOLS

A	area; without subscript, base area of cone
a	area of shock cone to base of cone
B	ballistic parameter
$b_0, b_1, b_2, b_3$	constants
C, c	constants
$C_D$	drag coefficient
$C_F$	friction coefficient
$C_H$	over-all heat-transfer coefficient
$c_p$	specific heat at constant pressure
D	drag
d	diameter of ablation rod
E	kinetic energy
$\dot{E}$	time rate of radiation
Ei	exponential integral
e	Napierian logarithm base
F	total frictional force
$G_1, G_2, G_3, G_4$	constants
g	ratio of total enthalpy, $\frac{h_T}{h_{T_e}}$
H	aerodynamic heat input in kinetic energy units
h	enthalpy
K	ablative coolant parameter
k	thermal conductivity

$l$	model length
$M$	mach number
$m$	mass
$Pr$	Prandtl number
$p$	pressure
$q$	heating rate per unit surface area
$R$	gas constant
$Re$	Reynolds number
$r$	radius
$St$	Stanton number
$T$	temperature
$t$	time
$U$	velocity normal to shock
$U_{1,2}$	a particular velocity, 13,700 m/sec
$u$	velocity in boundary layer
$V$	vehicle velocity
$v$	volume of shock layer
$X$	distance along axis of revolution measured forward of body base
$x$	distance along the cone surface from apex
$Y$	altitude
$y$	distance perpendicular to cone surface
$Z_e$	equilibrium heat-transfer function of $V_E \sin \theta_W$
$z$	compressibility factor
$\alpha$	function of ablation material
$\beta$	inverse of scale height
$\Gamma$	gamma function

$\gamma$	flight-path angle measured from local horizontal
$\Delta m$	total ablated mass
$\Delta\theta$	difference between bow shock angle and cone angle
$\delta$	increment
$\xi$	energy required to ablate a unit mass
$\eta$	energy fraction
$\theta_C$	half-angle of cone
$\theta_W$	shock angle
$\Lambda$	function of $V_E$ , $\theta_C$ , $\xi$ , and $\eta$
$\lambda$	nondimensional height within a boundary layer
$\mu$	absolute viscosity
$\nu$	kinematic viscosity
$\xi$	ablation parameter, $KV_E^2$
$\rho$	air density at any altitude $Y$
$\bar{\rho}$	air density ratio, $\frac{\rho}{\rho_0}$
$\sigma$	asymptotic value of $\frac{C_H}{C_{H_0}}$
$\Phi$	function of $B$
$\chi$	the product of $B\bar{\rho}$
$\Psi$	functions of $\theta_C$
$\Omega$	functions of $\xi$
$\omega$	an arbitrary variable

#### Powers

$i$	arbitrary
$j_1, j_2$	velocity dependence power in laminar convection



$k_1, k_2$	velocity dependence power in turbulent convection
$n$	general exponential in power series
$p$	density dependence power in equilibrium radiation
$q_1, q_2$	velocity dependence power in equilibrium radiation
$s$	velocity dependence power in nonequilibrium radiation
'	at reference conditions

#### Subscripts

$b$	body (or body base as in $r_b$ )
$cl$	collision limit
$E$	at entrance into atmosphere
$e$	equilibrium radiation
$e_1$	equilibrium radiation at $U < 13,700$ m/sec
$e_2$	equilibrium radiation at $U > 13,700$ m/sec
$fm$	free molecule
$i$	incompressible
$l$	laminar convection
$l_0$	laminar convection in absence of ablation
$l_1$	laminar convection for $V < 13,000$ m/sec
$l_2$	laminar convection for $V > 26,000$ m/sec
$lim$	limit
$max$	maximum
$n$	nonequilibrium radiation
$o$	sea level
$opt$	optimum
$sp$	stagnation point

$t$	turbulent convection
$t_0$	turbulent convection in absence of ablation
$t_1$	turbulent convection for $V \sin \theta_W < 7,500$ m/sec
$t_2$	turbulent convection for $V \sin \theta_W > 7,500$ m/sec
$\tau$	total
$w$	at cone wall
$\epsilon$	at edge of boundary layer
$2$	conditions behind the shock
$\infty$	free stream

## APPENDIX B

### EQUILIBRIUM RADIATIVE HEATING

#### Dependence on Velocity and Air Density

It is by no means obvious that an equation of the form of equation (16) can be used to represent the dependence on density and velocity of the radiative output per unit volume of the gas behind a normal shock wave. In particular, if the exponents  $q$  and  $p$  are subject to large and continuous variations and are themselves functions of  $U$  and  $\bar{\rho}$ , the usefulness of this representation would be seriously limited. However, it has been previously shown (e.g., in ref. 10) that plotting  $(1/\bar{\rho}^{1.7})(d\dot{E}_e/dv)$  logarithmically against velocity results in a reduction of available experimental and theoretical data to a fairly narrow band whose center is nearly a straight line for velocities from 5 to 13 km/sec. The theoretical lines in such a presentation show a definite swerving behavior in this speed range, indicative of local variations in the value of  $q$  (see fig. 7, ref. 10), but never deviate too far from a straight line.

Since we are concerned in this paper with a broader velocity range than that considered in reference 10, we plotted the collected theoretical data applicable to this broader speed range in figure 33. Here the  $\log_{10}(d\dot{E}_e/dv)$  is plotted against  $\log_{10}U$  for several altitudes, thus deferring for the moment the consideration of the effect of altitude. The symbols represent the theoretical data and were based on the results of references 5, 26, and 27. It is seen that three distinct regions of velocity dependence are suggested by the data, each of which can be fitted by a straight line segment. The low velocity range extends from about 4 to 8 km/sec; the intermediate range is from 8 to 13.7 km/sec; and the high range extends to at least 30 km/sec. Thus, the two lower speed ranges correspond to the complete velocity range of reference 10, and the two slopes represent, to an acceptable degree, the principal swerve in the theoretical curves shown in that reference. In the integrations of total heat input for the present paper, the existence of a different velocity dependence in the lowest speed range was ignored because of the comparatively small values of radiative heating in this speed range; the middle region was assumed to extend to zero velocity.

In fairing the lines on figure 33, certain restrictions were imposed:

(1) The line segments in each velocity range were required to have the same slope at all altitudes. (2) The intersections of the lines for the upper two velocity ranges were required to occur at a constant velocity, independent of altitude. These restrictions were made so as to make  $q$  independent of  $\bar{\rho}$  and so that a single speed,  $U_{1,2} = 13,700$  m/sec, would be the transition speed from one set of curves to the other at all altitudes. These restrictions did not seriously impair the fit of the lines to the data, the worst error being a factor of 2 and occurring at high altitude (and therefore at comparatively low radiative intensity).

While the theory for the lower-two speed regions is well supported by the data of reference 10, the radiative intensities in the highest speed region are entirely based on the theory of reference 27 for which there is no experimental

verification. This theory treats air at temperatures extending above 200,000° K, well beyond the highest temperatures (50,000° K) considered in the present paper. Above 100,000° K, the theory predicts that the radiative energy output is essentially independent of temperature. Between 20,000° K and 100,000° K, the temperature dependence may be represented by  $T^{3.5}$ . At still lower temperatures, according to data given in references 5 and 26, the dependence is approximated by  $T^{10.7}$ . Thus the slope change in figure 33 at  $U_{1,2} = 13,700$  m/sec is primarily a result of the change of temperature exponent which is predicted to change further and go to zero at still higher speeds and temperatures. Although these predictions should perhaps be viewed with caution pending experimental verification, it is noted that analysis of several meteor entries (ref. 28) indicated that the magnitude of the radiation predicted by the theory is perhaps correct.

The altitude or density dependence may now be considered. The radiative intensity at a velocity of 13,700 m/sec is plotted on logarithmic coordinates in figure 34 for the four altitudes of figure 33 as a function of the density ratio  $\bar{\rho}$ . A straight line is a remarkably good fit to these data, which, together with the previous figure, indicates the appropriateness of the form of equation (16). The slope of the line gives  $p = 1.80$ . The fact that this plot is made for the juncture velocity of the two upper speed regions means that this slope is valid for velocities both above and below this velocity. At other velocities, lines parallel to that shown are obtained. (If it had not been possible to find a common velocity at all altitudes for the intersection of the lines of the two families, this would have implied that  $p$  is different in the two velocity regions.) The evaluation of the constants  $C_{e1}$ ,  $C_{e2}$ ,  $p$ ,  $q_1$ , and  $q_2$  from figures 33 and 34 is straightforward and gives the values recorded in the text as equation (17).

#### Calculation of Shock-Wave Angles

For purposes of calculating the volume of gas radiating to the body and defining local flow properties at the boundary-layer edge for the convective heating estimates, the following approximate analysis of hypervelocity flow over pointed cones was made. The gas was assumed to have the properties of real air at equilibrium. The shock layer was assumed to be of uniform density and velocity, consistent with the knowledge that the entropy is uniform and the shock layer is very thin. Under these assumptions, continuity of flow requires that

$$\frac{\rho V}{\rho_2 V_2} \left( 1 + \frac{\tan \Delta\theta}{\tan \theta_C} \right)^2 \cos \theta_C = 2 \frac{\tan \Delta\theta}{\tan \theta_C} + \left( \frac{\tan \Delta\theta}{\tan \theta_C} \right)^2 \quad (B1)$$

where  $\rho_2$  and  $V_2$  are the density and total velocity behind the shock wave. This is solved for  $\tan \Delta\theta$  to obtain

$$\frac{\tan \Delta\theta}{\tan \theta_C} = \sqrt{\frac{1}{1 - \frac{\rho V}{\rho_2 V_2} \cos \theta_C}} - 1 \quad (B2)$$

Given the cone angle  $\theta_C$  and the free-stream density and velocity,  $\rho$  and  $V$ , equation (B2) is solved iteratively with the aid of real gas shock-wave tables or charts such as those given in reference 29. A first-approximation estimate of the standoff angle  $\Delta\theta$  permits the downstream flow properties to be obtained so that  $\rho V/\rho_2 V_2$  can be evaluated. Inserted in equation (B2), this leads to a new value of  $\Delta\theta$ , and the iteration is continued to convergence (usually one more cycle).

Standoff angles computed by this technique are shown in figure 35 for velocities of 6 to 22 km/sec, cone half-angles of  $15^\circ$ ,  $30^\circ$ , and  $55^\circ$ , and an altitude of 50 km. A result of these computations was that the velocity ratio  $V_2/V$  was given almost exactly by  $\cos \theta_W$  and within 9 percent by  $\cos \theta_C$ , so that equation (B2) may be approximated by

$$\frac{\tan \Delta\theta}{\tan \theta_C} = \sqrt{\frac{1}{1 - \frac{\rho}{\rho_2}}} - 1 \quad (B3)$$

or, for  $\rho/\rho_2 \ll 1$ ,  $\Delta\theta \approx (1/2)(\tan \theta_C)(\rho/\rho_2)$  radians, a result which is analogous to that obtained in studies of shock-wave standoff distance for blunt bodies (see, e.g., ref. 30).

Since the standoff angle is a function of the density ratio across the bow wave, it follows that  $\Delta\theta$  will vary in a complicated fashion with free-stream velocity and altitude. The most general way to give the results of the present calculations is to show the dependence on density ratio, as is done in figure 35, where the circular points represent the values obtained at the conditions cited in the previous paragraph. For comparison, two points obtained by the exact theory of Taylor and Maccoll (see ref. 31) are shown for an ideal gas with a ratio of specific heats equal to 1.4 at infinite Mach number (square symbols). Since, at the highest speeds considered here, the density ratio at the bow wave tends to values between 15 and 18, a working curve was drawn showing approximate values of  $\Delta\theta$  as a function of cone angle for free-stream velocities greater than 20 km/sec, figure 36. For simplicity, this curve was assumed to be universally applicable in the equilibrium radiative heating integrations.

Also shown in figure 36 is an interpolated curve from the present calculations for a lower speed, 9.2 km/sec, and an altitude of 50 km. This curve is compared with points taken from reference 32 for speeds near 9.2 km/sec and a free-stream pressure of  $0.001 p_0$  which approximates the pressure at 50 km altitude. The method of Taylor and Maccoll for real air at equilibrium was used in the calculations of this reference. While agreement is by no means exact, it is within 20 percent at the worst point. The reasons for the disagreement are not clear.

A final comment on the behavior of the curves of figure 36 in the vicinity of  $\theta_C = 0$  is in order. Although the lower curve seems to be going into the origin, we know that at  $\theta_C = 0$ ,  $\Delta\theta = \sin^{-1}(1/M)$ , and the wave angle can never be less than the Mach angle (i.e.,  $\theta_C + \Delta\theta \geq \sin^{-1}(1/M)$ ). Since the Mach angles at the speeds considered range from a few tenths of a degree to  $1^\circ$  or  $2^\circ$ , this

limitation need not be considered until  $\theta_C < 2^\circ$ . For cone angles smaller than  $2^\circ$  (an academic case), the curves must turn up and terminate at  $\Delta\theta = \sin^{-1}(1/M)$ .

### Evaluation of Equilibrium Energy Fraction

In the integral of equation (22a) the value of  $e^{-(B/2)(q_1-1)\bar{\rho}}$  when  $\bar{\rho}$  is of the order of unity or larger is so small that with negligible error we may write for  $p$  greater than zero

$$\int_{\bar{\rho}=0}^1 e^{-(B/2)(q_1-1)\bar{\rho}} \bar{\rho}^{p-1} d\bar{\rho} \approx \int_0^\infty e^{-(B/2)(q_1-1)\bar{\rho}} \bar{\rho}^{p-1} d\bar{\rho} = \frac{\Gamma(p)}{B^p \left(\frac{q_1-1}{2}\right)^p} \quad (B4)$$

wherein  $\Gamma(p)$  is the familiar gamma function (see, e.g., ref. 33). Similarly, we may write

$$\int_{\bar{\rho}=\bar{\rho}_{1,2}}^1 e^{-(B/2)(q_1-1)\bar{\rho}} \bar{\rho}^{p-1} d\bar{\rho} \approx \frac{\Gamma(p)}{B^p \left(\frac{q_1-1}{2}\right)^p} - \int_0^{\bar{\rho}_{1,2}} e^{-(B/2)(q_1-1)\bar{\rho}} \bar{\rho}^{p-1} d\bar{\rho} \quad (B5)$$

wherein

$$\bar{\rho}_{1,2} = \frac{2}{B} \ln \left( \frac{V_E \sin \theta_W}{U_{1,2}} \right) \quad (B6)$$

The right-hand integral of equation (B5) may be evaluated by expanding the exponential in a power series. Thus,

$$\int_0^{\omega_1} e^{-c\omega} \omega^i d\omega = \int_0^{\omega_1} \sum_{n=0}^{\infty} \frac{(-c\omega)^n}{n!} \omega^i d\omega = \omega_1^{i+1} \sum_{n=0}^{\infty} \frac{(-c\omega_1)^n}{n!(n+i+1)} \quad (B7)$$

With these formulations, then, the equilibrium energy fraction can be put in the form of equation (24)

$$\eta_e = \frac{r_b \psi_e Z_e}{B^{0.8}}$$

if we put

$$y_e = \frac{\sin^3 \theta_W (\tan^2 \theta_W - \tan^2 \theta_C)}{\sin^2 \theta_C \tan^3 \theta_C} \quad (B8)$$

$$Z_e = c_{e1} \frac{(V_E \sin \theta_W)^{q_1-3}}{6 \left( \frac{q_1-1}{2} \right)^p} \Gamma(p) ; \quad V_E \sin \theta_W < U_{1,2} \quad (B9a)$$

and

$$Z_e = c_{e1} \frac{(V_E \sin \theta_W)^{q_1-3}}{6 \left( \frac{q_1-1}{2} \right)^p} \left\{ \Gamma(p) - \left[ (q_1-1) \ln \frac{V_E \sin \theta_W}{U_{1,2}} \right]^p \sum_{n=0}^{\infty} \frac{\left[ -(q_1-1) \ln \frac{V_E \sin \theta_W}{U_{1,2}} \right]^n}{n! (p+n)} \right\}$$

$$+ c_{e2} \frac{(V_E \sin \theta_W)^{q_2-3}}{6 \left( \frac{q_2-1}{2} \right)^p} \left[ (q_2-1) \ln \frac{V_E \sin \theta_W}{U_{1,2}} \right]^p \sum_{n=0}^{\infty} \frac{\left[ -(q_2-1) \ln \frac{V_E \sin \theta_W}{U_{1,2}} \right]^n}{n! (p+n)} ;$$

$$V_E \sin \theta_W > U_{1,2} \quad (B9b)$$

From the relations of equations (17) and (23), then,

$$Z_e = 0.0701 \left( \frac{V_E \sin \theta_W}{10^4} \right)^{12.45} ; \quad \frac{V_E \sin \theta_W}{10^4} < 1.37 \quad (B10a)$$

$$Z_e = 0.0701 \left( \frac{V_E \sin \theta_W}{10^4} \right)^{12.45} \left[ 1 - 1.074 x_1^{1.8} \left( \frac{1}{1.8} - \frac{x_1}{2.8} + \frac{x_1^2}{2!(3.8)} - \frac{x_1^3}{3!(4.8)} + \dots \right) \right]$$

$$+ 19.45 \left( \frac{V_E \sin \theta_W}{10^4} \right)^{2.05} x_2^{1.8} \left( \frac{1}{1.8} - \frac{x_2}{2.8} + \frac{x_2^2}{2!(3.8)} - \frac{x_2^3}{3!(4.8)} + \dots \right) ;$$

$$\frac{V_E \sin \theta_W}{10^4} > 1.37 \quad (B10b)$$

wherein

$$\left. \begin{aligned} x_1 &= 14.45 \ln \left( \frac{V_E \sin \theta_W}{13,700} \right) \\ x_2 &= 4.05 \ln \left( \frac{V_E \sin \theta_W}{13,700} \right) \end{aligned} \right\} \quad (B11)$$



## APPENDIX C

### NONEQUILIBRIUM RADIATIVE HEATING

The treatment of nonequilibrium radiative heating in this paper is based on the conceptual model of the nonequilibrium region described in references 34 and 10, and on the experimental observations of nonequilibrium air radiation of reference 10. Although the research on nonequilibrium air radiation is at the present writing still very new, it appears to be approaching a satisfactory definition of the radiative intensities for speeds normal to the shock wave up to 13,000 meters/sec. For the higher speeds treated in the present paper, it was necessary to extrapolate.

The data of reference 10 are reproduced in figure 37 on logarithmic coordinates as a function of velocity normal to the shock wave. They define a line with a slope of approximately 4, and are represented by the equation

$$\frac{d\dot{E}_n}{da} = 1.15 \times 10^{-11} U^{4.08} \quad (C1)$$

The line defined by equation (25a) of the text,

$$\frac{d\dot{E}_n}{da} = 0.74 \times 10^{-22} U^7 \quad (C2)$$

was adopted on the basis of data available earlier, and is plotted for comparison. For a speed of 11,000 meters/sec, it is seen to indicate about four times the radiative intensity given by the latest data. In view of the finding of the analysis (see text) that the nonequilibrium radiation makes a relatively small contribution to the total heating, no revision to the analysis on the basis of equation (C1) was made. The conservatism implied by use of equation (C2) at the higher speeds may be considered desirable in view of the present velocity limit of the experiments.

In spite of the density independence of equations (C1) and (C2), various effects are known to contribute to a cut-off of the nonequilibrium radiation at very high altitudes, as discussed in references 34 and 10. The contributing effects include the flow energy limitation, truncation of the nonequilibrium region by the presence of the body, cooling of the shock layer by a thick viscous boundary layer, and collision limiting. For simplicity, these effects are lumped in the present analysis into a single effect, referred to as collision limiting, and assumed to begin reducing the radiation at altitudes just above 50 km. This choice appears reasonable based on information given in the references cited above.

## Evaluation of Nonequilibrium Energy Fraction

The integrals of equation (30) are

$$\int_{\bar{\rho}_{cl}}^1 e^{-B\left(\frac{s-1}{2}\right)\bar{\rho}} \frac{d\bar{\rho}}{\bar{\rho}} = \text{Ei} \left[ -\frac{B(s-1)}{2} \right] - \text{Ei} \left[ -\frac{B(s-1)}{2} \bar{\rho}_{cl} \right] \quad (\text{C3})$$

wherein values of the exponential integral  $\text{Ei}(-w)$  may be obtained from published tables (e.g., ref. 33), and

$$\int_{\bar{\rho}_{fm}}^{\bar{\rho}_{cl}} e^{-B\left(\frac{s-1}{2}\right)\bar{\rho}} d\bar{\rho} = \frac{e^{-B\left(\frac{s-1}{2}\right)\bar{\rho}_{fm}} - e^{-B\left(\frac{s-1}{2}\right)\bar{\rho}_{cl}}}{B\left(\frac{s-1}{2}\right)} \approx \frac{1 - e^{-B\left(\frac{s-1}{2}\right)\bar{\rho}_{cl}}}{B\left(\frac{s-1}{2}\right)} \quad (\text{C4})$$

since  $\bar{\rho}_{fm}$  is very small. The constant given by equations (26) and (31) can be used to put  $\eta_n$  in the form of equation (32)

$$\eta_n = \Psi_n \Phi_n \left( \frac{V_E}{10^4} \right)^4$$

if we define

$$\Psi_n = \frac{\sin^6 \theta_W \tan^2 \theta_W}{\sin^2 \theta_C \tan^2 \theta_C} \quad (\text{C5})$$

and

$$\Phi_n = 3B \times 10^{-7} \left[ \text{Ei}(-3B) - \text{Ei}(-3B \times 10^{-3}) + \frac{1 - e^{-3B \times 10^{-3}}}{3B \times 10^{-3}} \right] \quad (\text{C6})$$

## APPENDIX D

### LAMINAR CONVECTIVE HEATING

#### Theoretical Method

The laminar convective heat-transfer coefficients for zero ablation,  $C_{H_{H_2O}}$ , were calculated by the method of Kemp, Rose, and Detra (ref. 35) modified as described in this appendix. Numerical examples for cone half-angles of  $15^\circ$ ,  $30^\circ$ , and  $55^\circ$  at velocities of 6, 10, 14, 18, 22 and 26 km/sec and at altitudes of 20, 35, 50, and 75 km were then calculated. With the set of theoretical data so obtained, the form of a suitable empirical equation to represent these data was determined (eq. (33)) and the empirical constants were evaluated.

Reference 35 (eq. (21)) gives the approximate relation on which the heat-transfer estimates were based which for cones may be written<sup>1</sup>

$$\frac{\sqrt{2} \ g_{\lambda_w}}{1 - g_w} = 0.648 \left( \frac{\rho_\epsilon \mu_\epsilon}{\rho_w \mu_w} \right)_{sp}^{0.438} \quad (D1)$$

where  $g = h_\tau/h_{\tau_\epsilon}$ ,  $h_\tau = h + (u^2/2)$ ,  $h$  is static enthalpy,  $g_{\lambda_w} = (\partial g/\partial \lambda)_w$ ,  $\lambda$  is a transformed coordinate normal to the body surface,  $\epsilon$  and  $w$  indicate conditions at the boundary-layer edge and at the wall, respectively, and  $\rho$ ,  $u$ , and  $\mu$  have their usual boundary-layer significance. An approximation suggested in this reference is the evaluation of the ratio  $\rho_\epsilon \mu_\epsilon / \rho_w \mu_w$  at the stagnation point for subsequent application to all points on the surface. This is said to introduce errors no larger than a few percent compared to more exact procedures in several instances where they have been compared. Equation (D1) also assumes that the Lewis number is 1.0.

Since, for a Lewis number of 1.0,

$$q = \frac{k_w}{c_{p_w}} \left( \frac{\partial h}{\partial y} \right)_w \quad (D2)$$

(where  $k_w$  and  $c_{p_w}$  are the gas conductivity and specific heat at the wall, and  $q$  is the local heat-transfer rate per unit area), and the relation between  $y$  and  $\lambda$  is as given in reference 35, equation (D1) may be written for cones as

$$q = \frac{\sqrt{3}}{2} 0.648 \sqrt{\frac{\rho_w u_\epsilon}{x \mu_w}} \left( \frac{k_w}{c_{p_w}} \right) \left( h_\infty + \frac{V^2}{2} - h_w \right) \left( \frac{\rho_\epsilon \mu_\epsilon}{\rho_w \mu_w} \right)_{sp}^{0.438} \quad (D3)$$

---

<sup>1</sup>To avoid conflict with the symbols used in this report, certain of the symbols in the equations to follow have been changed from the original form. The quantities  $H$  and  $\eta$  of reference 35 are denoted herein as  $h_\tau$  and  $\lambda$ .

Integrated over the surface of the cone to obtain  $dH/dt$  and divided by  $(1/2)\rho V^3 A$  to obtain  $C_{H_{lO}}$ , this becomes

$$C_{H_{lO}} = \frac{2}{\sqrt{3}} 0.648 \frac{\sqrt{\rho_w u_\epsilon x_b / \mu_w}}{\rho V r_b} \left( \frac{k_w}{c_{p_w}} \right) \left[ \frac{h_\infty + (V^2/2) - h_w}{V^2/2} \right] \left( \frac{\rho_\epsilon \mu_\epsilon}{\rho_w \mu_w} \right)_{sp}^{0.438} \quad (D4)$$

where  $x_b$  and  $r_b$  are the slant length and base radius of the cone and

$$\frac{h_\infty + (V^2/2) - h_w}{V^2/2} \approx 1$$

for high velocities.

Equation (D4) may be put in terms of the free-stream Reynolds number  $\rho V r / \mu$  to obtain

$$C_{H_{lO}} = \frac{(2/\sqrt{3})0.648}{Pr_w \sqrt{\rho V r_b / \mu}} \sqrt{\frac{\rho_w}{\rho} \frac{\mu_w}{\mu}} \cot \theta_C \left( \frac{\rho_\epsilon \mu_\epsilon}{\rho_w \mu_w} \right)_{sp}^{0.438} \quad (D5)$$

where  $Pr_w$  is the Prandtl number at the wall, and  $u_\epsilon/V = \cos \theta_C$  has been used (see appendix B). Properties without subscripts are evaluated in the free stream ahead of the bow shock wave.

## Discussion

In the application of equation (D4),  $u_\epsilon$  was taken to be the value for a sharp cone, corresponding to an assumption of small tip blunting. In cases where tip blunting occurs to an appreciable extent,  $u_\epsilon$  becomes lower than it would be for a sharp tip, while nothing else in equation (D4) is affected, so that the convective heat transfer is predicted to diminish. In this respect, the results of the present analysis are conservatively high.

The accuracy of the heating estimates obtained on the basis of equation (D1) cannot be assessed at the present time, but they could be in appreciable error. It is noted that equation (D1) is obtained by modifying a stagnation point solution on the basis of an empirical observation. Therefore, if it is applied to conditions outside the range of its evaluation, as it is here, it may be inaccurate. Thus, values of  $(\rho_\epsilon \mu_\epsilon / \rho_w \mu_w)_{sp}$  as low as 0.0035 were encountered in the calculations, while reference 35 recommends equation (D1) for the range of this parameter from 0.15 to 0.55. Similarly, values of  $u_\epsilon^2 / h_{T_\epsilon} = 2 \cos^2 \theta_C$  up to 1.86 were treated, where reference 35 discusses values up to 1.50. Because of the uncertainties present, a new theoretical study of real air laminar convection

to cones has been started at Ames Research Center, and initial results indicate that the present estimates are probably inaccurate at worst by a factor of 2.

### Computation of Results, and Fitting the Empirical Equation

The gas properties required in equation (D5) for stagnation temperatures up to  $47,000^\circ\text{K}$  were taken from references 36, 37, and 38. Reference 36 gives the thermodynamic properties of air for temperatures up to  $100,000^\circ\text{K}$ , and reference 37 gives the viscosity and other properties up to  $15,000^\circ\text{K}$ . Reference 38 is an extension of reference 37 to  $30,000^\circ\text{K}$  for pure nitrogen, and shows that the transport properties do not differ greatly between air and pure nitrogen in the temperature range up to  $15,000^\circ\text{K}$ . The nitrogen data were therefore used at the higher temperatures and extrapolated where necessary. The extrapolation, which certainly should not be considered reliable to more than one significant figure, was performed on a logarithmic plot of viscosity versus enthalpy. A family of curves was plotted with pressure as parameter, so that the shapes of all the curves could be used to guide the extrapolation.

A wall temperature of  $3,000^\circ\text{K}$ , representative of the temperatures attained by carbon, quartz, and the charring ablators, was selected for evaluation of the air properties at the wall. However, it can be shown from equation (D5) that  $\text{CH}_2\text{O}$  is not a sensitive function of the wall temperature.

The factor  $(\rho_\epsilon \mu_\epsilon / \rho_w \mu_w)_{sp}^{0.438}$  in equation (D5) is independent of cone angle, and is shown plotted in figure 38 as a function of velocity for four altitudes from 20 km to 75 km. It decreases continuously with increasing velocity. The altitude dependence is small at low velocities, but becomes appreciable at the higher velocities. Since an empirical expression in which the density dependence is a function of the velocity was undesirably complex for our purposes, and in view of the convenience of exponential forms, a single curve independent of the density, shown in figure 38, was taken to represent  $(\rho_\epsilon \mu_\epsilon / \rho_w \mu_w)_{sp}^{0.438}$ . The equation of this line is

$$\left( \frac{\rho_\epsilon \mu_\epsilon}{\rho_w \mu_w} \right)_{sp}^{0.438} = (3.4 \times 10^6) V^{-5/3} \quad (D6)$$

It can be seen from the figure that this expression does not apply at speeds much below 10 km/sec, and is very approximate throughout the range.

The dependence of heat-transfer coefficient on cone angle, according to equation (D5), is entirely contained in the radical,  $\sqrt{(\rho_w/\rho)(\mu_w/\mu)\cot\theta_C}$ . The factor  $\rho_w/\rho$  may be expressed

$$\frac{\rho_w}{\rho} = \frac{p_w}{p} \frac{T}{z_w T_w} = \left[ (\sin^2 \theta_C) \frac{V^2}{RT} + 1 \right] \frac{T}{z_w T_w} \quad (D7)$$

which for large values of  $V \sin \theta_C = U$  reduces to

$$\frac{\rho_w}{\rho} = \frac{V^2 \sin^2 \theta_C}{Rz_w T_w} \quad (D8)$$

and the radical becomes

$$\sqrt{\frac{\rho_w}{\rho} \frac{\mu_w}{\mu} \cot \theta_C} = V \sqrt{\frac{\mu_w/\mu}{2Rz_w T_w} \sin 2\theta_C} \quad (D9)$$

where  $\sqrt{(\mu_w/\mu)/2Rz_w T_w}$  is nearly independent of cone angle, speed, and altitude and is equal to approximately 0.0016 sec/m for  $T_w = 3000^\circ \text{ K}$ .

Substitution of equations (D6) and (D9) into (D5), along with values for the viscosity in the free stream, the wall Prandtl number, and  $\rho_o$ , results in the final expression for  $CH_{l_o}$  given in the text as equations (33) and (38),

$$CH_{l_o} = \frac{19.8 \sqrt{\sin 2\theta_C}}{V^{1.17} \sqrt{\bar{\rho} r_b}} \quad (D10)$$

Values of  $CH_{l_o}$  given by equation (D5) are plotted against velocity in figures 39 and 40 as points, and are treated as data to be fitted. They show the heat-transfer coefficient to be nearly independent of velocity at the lower velocities, and then to diminish with further increases in velocity. The curves described by equation (D10) disagree with these data at the low velocities, but agree approximately at the higher velocities. Disagreement (in opposite directions) also occurs at the highest and lowest altitudes considered (fig. 40). All of these trends can be foreseen from figure 38. At speeds below 13 km/sec, a reasonable fit is obtained by taking  $CH_{l_o}$  independent of velocity,  $j = 0$  in equation (33). The level lines shown in this region correspond to the low-speed coefficients of equation (33), given as equation (37). It may be said that these fitted equations describe the calculated data adequately, in view of present uncertainties in the method of calculation.

In applying these equations, a smooth transition was made between the low-speed regime with  $j = 0$  and the high-speed regime with  $j = 1.17$ . The transition curve, described in the text, was a four term series in powers of  $V$ , with constants selected to match the levels and slopes of the two heating equations at 13,000 m/sec and 26,000 m/sec, respectively.

## Evaluation of Laminar-Convective Energy Fraction

To solve equation (44) we make the following assumptions:

(a) Because when  $\bar{\rho} \geq 1$ , the exponential

$$e^{-B\bar{\rho}} \quad (D11)$$

is very nearly zero for vehicles of interest to this paper, it is satisfactory to substitute unity for

$$1 + \xi_7 e^{-B\bar{\rho}} \quad (D12)$$

(b) Because in the range  $0 < \bar{\rho} < \bar{\rho}_{fm}$  for vehicles of interest to this paper  $V \cong V_E$ , then for the denominator of the first integral the expression  $1 + \xi_7 e^{-B\bar{\rho}}$  may be replaced with  $1 + \xi_7$ .

With these simplifications equation (44) becomes, if we let

$$\chi = B\bar{\rho} \quad (D13)$$

$$\begin{aligned} \eta_L = & \frac{\sqrt{B} c_L (1 - \sigma_L)}{2V_E^j \sqrt{r_b} \sin^2 \theta_C} \int_0^\infty \frac{e^{-(1-\frac{j}{2})\chi} d\chi}{(1 + \xi_7 e^{-\chi}) \sqrt{\chi}} \\ & + \frac{\sqrt{B} c_L \sigma_L}{2V_E^j \sqrt{r_b} \sin^2 \theta_C} \int_0^\infty \frac{e^{-(1-\frac{j}{2})\chi} d\chi}{\sqrt{\chi}} - \frac{\sqrt{B} c_L}{2V_E^j \sqrt{r_b} \sin^2 \theta_C} \int_B^\infty \frac{e^{-(1-\frac{j}{2})\chi} d\chi}{\sqrt{\chi}} \\ & - \left( \frac{1 - \sigma_L}{1 + \xi_7} + \sigma_L \right) \frac{\sqrt{B} c_L}{2V_E^j \sqrt{r_b} \sin^2 \theta_C} \int_0^{B\bar{\rho}_{fm}} \frac{e^{-(1-\frac{j}{2})\chi} d\chi}{\sqrt{\chi}} + \frac{1}{2} \int_0^{B\bar{\rho}_{fm}} e^{-\chi} d\chi \end{aligned} \quad (D14)$$

The first and third integrals can be evaluated numerically; the second is a gamma function; the fourth can be evaluated as a series after expanding the exponential as a series; and, although the fifth can be integrated directly, it is preferable to express it in series form also. The solution may be written as

$$\begin{aligned}
\eta_l = & \frac{c_l(1 - \sigma_l)}{2V_E^j \sin^2 \theta_C} \sqrt{\frac{B}{r_b}} \Omega_l + \frac{c_l \sigma_l}{2V_E^j \sin^2 \theta_C} \sqrt{\frac{B}{r_b}} \left[ \frac{2\Gamma\left(\frac{3}{2}\right)}{\sqrt{1 - \left(\frac{j}{2}\right)}} \right] \\
& - \frac{c_l}{2V_E^j \sin^2 \theta_C} \sqrt{\frac{B}{r_b}} \Phi_l - \left( \frac{1 - \sigma_l}{1 + \xi_l} + \sigma_l \right) \frac{c_l \sqrt{B \bar{\rho}_{fm}}}{2V_E^j \sin^2 \theta_C} \sqrt{\frac{B}{r_b}} \sum_{n=0}^{\infty} \frac{\left[ \left( \frac{j}{2} - 1 \right) B \bar{\rho}_{fm} \right]^n}{n! \left( \frac{1}{2} + n \right)} \\
& - \frac{1}{2} \sum_{n=1}^{\infty} \frac{(-B \bar{\rho}_{fm})^n}{n!}
\end{aligned} \tag{D15}$$

wherein

$$\Omega_l = \int_0^{\infty} \frac{e^{-(1-\frac{j}{2})x} dx}{(1 + \xi_l e^{-x}) \sqrt{x}} \tag{D16}$$

and

$$\Phi_l = \int_B^{\infty} \frac{e^{-(1-\frac{j}{2})x} dx}{\sqrt{x}} \tag{D17}$$

Since (see ref. 33)  $\Gamma(3/2) = 0.8862$ , then equation (D15) may be written

$$\begin{aligned}
\eta_l = & \frac{c_l}{2V_E^j \sin^2 \theta_C} \sqrt{\frac{B}{r_b}} \left[ (1 - \sigma_l) \Omega_l + 1.7724 \frac{\sigma_l}{\sqrt{1 - (j/2)}} - \Phi_l \right] \\
& - \frac{1}{2} \left( \frac{c_l}{V_E^j \sin^2 \theta_C} \right)^2 \left( \frac{1 - \sigma_l}{1 + \xi_l} + \sigma_l \right)^2 \left( \frac{B}{r_b} \right) \\
& + \frac{1 - 2j}{12} \left( \frac{c_l}{V_E^j \sin^2 \theta_C} \right)^4 \left( \frac{1 - \sigma_l}{1 + \xi_l} + \sigma_l \right)^4 \left( \frac{B}{r_b} \right)^2 + \dots
\end{aligned} \tag{D18}$$

For vehicles of interest in this report the final term shown above in this equation is always negligibly small but the preceding term can be important for "small light" entry bodies (very large  $B/r_b$ ). The value of  $\Phi_l$  is only important for "large heavy" entry bodies (very small  $B$ ). Values of  $\Omega_{l1}$  and  $\Omega_{l2}$ , and  $\Phi_{l1}$  and  $\Phi_{l2}$  (corresponding to  $j_1$  and  $j_2$  of eqs. (37) and (38)) are given in tables IV and III, respectively.



Equation (D18) can be written in the form of equations (45) and (46) if we set

$$\left. \begin{aligned} \Psi_{l_1} &= \frac{c_{l_1}}{2 \sin^2 \theta_C} = 1.76 \times 10^{-4} \frac{\sqrt{\sin 2\theta_C}}{\sin^2 \theta_C} \\ \Psi_{l_2} &= \frac{c_{l_2}}{2 \sin^2 \theta_C} = 2.07 \times 10^{-4} \frac{\sqrt{\sin 2\theta_C}}{\sin^2 \theta_C} \end{aligned} \right\} \quad (\text{D19})$$

Values for these functions are given in table I.

## APPENDIX E

### TURBULENT CONVECTIVE HEAT TRANSFER

#### Method of Estimation

Turbulent heat-transfer rates for pointed cones at flight speeds up to 30,000 m/sec were estimated by use of Colburn's modified Reynolds analogy, reference 39, and the reference enthalpy method. The latter is a generalization to the case of a dissociating gas at high temperature of the reference temperature or  $T'$  method described in reference 40. The  $T'$  method has been compared with measurements of skin friction and heat transfer for turbulent boundary layers in subsonic, supersonic, and hypersonic flow of air in or near the ideal gas temperature range, and is found to represent existing experiments unusually well (see, e.g., refs. 41 and 42). Of course, no experience exists for the much higher speeds considered here, and, in light of the purely empirical nature of the method, the degree of accuracy of these estimates cannot be presently determined. However, the excellent experience at supersonic Mach numbers below 10 encourages us to expect realistic values of heat-transfer prediction in the higher speed range.

The  $T'$  equation of reference 40 is

$$\frac{T'}{T_\epsilon} = 1 + 0.035 M_\epsilon^2 + 0.45 \left( \frac{T_w}{T_\epsilon} - 1 \right) \quad (E1)$$

which may, for the ideal gas considered in that reference, be written in the form

$$\frac{T'}{T_\epsilon} = 1 + 0.175 \left( \frac{T_{sp}}{T_\epsilon} - 1 \right) + 0.45 \left( \frac{T_w}{T_\epsilon} - 1 \right) \quad (E2)$$

where  $T_{sp}$  is the stagnation point temperature. These equations define the temperature  $T'$  within the boundary layer at which to evaluate the density and viscosity so that the incompressible skin friction equation is applicable to the compressible flow boundary layer considered. The generalization to high temperature flow of equation (E2) is assumed to be

$$\frac{h'}{h_\epsilon} = 1 + 0.175 \left( \frac{h_{sp}}{h_\epsilon} - 1 \right) + 0.45 \left( \frac{h_w}{h_\epsilon} - 1 \right) \quad (E3)$$

which reduces to equation (E2) for a gas with constant specific heat. Here,  $(h_{sp}/h_\epsilon) - 1 = (1/2)(u_\epsilon^2/h_\epsilon)$ .<sup>1</sup> Given  $h'$  as defined by equation (E3) and the

---

<sup>1</sup>Although the details will not be given here, it can be shown starting from equation (E3) that the reference enthalpy is approximately a fixed fraction of the stream total enthalpy for any cone angle, the fraction being a direct function of the cone angle.

local static pressure on the cone, the state of the gas at the reference enthalpy condition is fully specified and the reference density  $\rho'$  may be obtained from reference 36 and the reference viscosity  $\mu'$  may be obtained from reference 37 or 38. The Reynolds number  $Re'$  given by  $\rho' u_\epsilon x / \mu'$  is then inserted in the incompressible turbulent skin-friction formula to obtain  $C_F'$ , which is related to the average skin friction over the surface  $C_F$  by

$$C_F \frac{1}{2} \rho_\epsilon u_\epsilon^2 = C_F' \frac{1}{2} \rho' u_\epsilon^2$$

or

$$C_F \rho_\epsilon = C_F' \rho'$$

The variation with Reynolds number of average skin friction coefficient on a flat plate in incompressible flow was taken to be that given by the Kármán-Schoenherr formula

$$\frac{0.242}{\sqrt{C_{F_i}}} = \log_{10} Re C_{F_i} \quad (E4)$$

which can be very closely approximated for Reynolds numbers from  $3 \times 10^6$  to  $10^9$  by the power law formula

$$C_{F_i} = \frac{0.0317}{Re^{0.148}} \quad (E5)$$

The turbulent skin friction values for a flat plate were modified by the factor 1.047, derived in appendix C of reference 39, to make them applicable to cones.

The Colburn modification of the Reynolds analogy

$$St = \frac{C_F}{2Pr_w^{2/3}} \quad (E6)$$

was then applied to obtain the dimensionless heat-transfer parameter, the Stanton number, defined by

$$St = \frac{dH/dt}{\rho_\epsilon u_\epsilon (h_{sp} - h_w) A_w} \quad (E7)$$

where  $A_w$  is the wetted area of the cone. From  $dH/dt$ ,  $C_{H_{t_0}}$  may be obtained from its definition, equation (4) of the text.

The above steps describe the procedure used. A summary equation approximating these steps may be written

$$C_{H_{t_0}} = \frac{0.0166}{(\rho' u_{\epsilon} x_b / \mu')^{0.148}} \frac{\rho'}{\rho} \frac{\cot \theta_C}{Pr_w^{2/3}} \quad (E8)$$

in which  $u_{\epsilon}/V = \cos \theta_C$  and  $(h_{sp} - h_w)/V^2 \approx 1/2$  have been applied along with the approximation given by equation (E5) for the Kármán-Schoenherr formula.

#### Expression in Terms of Free-Stream Variables

Equations (E8) and (E3) describe, in reasonably simple terms, the heat-transfer coefficient for the turbulent boundary-layer case, but they are not suitable for incorporation in the optimization analysis of this paper because they are expressed in terms of  $\rho'$  and  $\mu'$ , the variation of which with speed, cone angle, and free-stream density is not immediately evident. The point of departure for finding  $C_{H_{t_0}}$  as a function of  $V$ ,  $\theta$ , and  $\bar{\rho}$  was not equation (E8), but was based on the observation that for any altitude and base radius, the Stanton number was a nearly linear function of  $\theta_C$ , almost independent of velocity. This is shown in figure 41 for an altitude of 35 km. The equation for Stanton number obtained from plots of this kind for altitudes of 20, 35, and 50 km is

$$St = \frac{2.47}{10^5} \frac{\theta_C}{r_b^{0.148} \bar{\rho}^{0.165}} \quad (E9)$$

where  $\theta_C$  is in degrees and  $r_b$  in meters. The fact that the exponent of  $\bar{\rho}$  is here found empirically to differ a little from 0.148 reflects the dependence of the Stanton number on  $\rho'/\rho$  and  $\mu'/\mu$  which vary with altitude for any given cone angle.

From equations (E7), (E9), and (4) in the text,

$$\begin{aligned} C_{H_{t_0}} &= \frac{2.47}{10^5} \frac{\theta_C}{r_b^{0.148} \bar{\rho}^{0.165}} \frac{\rho_{\epsilon} u_{\epsilon} (h_{sp} - h_w) A_w}{(1/2) \rho V^3 A} \\ &= \frac{2.47}{10^5} \frac{\theta_C}{r_b^{0.148} \bar{\rho}^{0.165}} \frac{\rho_{\epsilon}}{\rho} \cot \theta_C \end{aligned} \quad (E10)$$

where  $u_{\epsilon}/V = \cos \theta_C$ ,  $h_{sp} - h_w \approx V^2/2$ , and  $A_w/A = 1/\sin \theta_C$  have been applied. In addition, the density ratio across the shock wave,  $\rho_{\epsilon}/\rho$ , may be correlated in terms of the velocity component normal to the shock wave,  $V \sin \theta_w = U$ , as shown in figure 42. Two regions exist. For  $U < 7500$  m/sec, the density ratio increases with increasing speed approximately as

$$\frac{\rho_{\epsilon}}{\rho} = \frac{0.0356}{\bar{\rho}^{0.039}} (V \sin \theta_w)^{0.66} \quad (E11)$$

For  $U > 7500$  m/sec, the density ratio becomes a slowly decreasing function of increasing velocity.

$$\frac{\rho_e}{\rho} = \frac{54.5}{\bar{\rho}^{0.039}} (V \sin \theta_W)^{-0.16} \quad (E12)$$

The accuracy of these expressions in relation to calculations for normal shock waves in equilibrium air may be examined in figure 42. Inserting these relations into equation (E10) leads to the expressions for  $CH_{t_0}$  given as equations (50) and (51) of the text.

The values of  $CH_{t_0}$  computed from the working equations (50) and (51) are compared in figure 43 for a cone angle of  $30^\circ$  and a 1-meter base radius with the values computed by the complete estimation procedure based on equations (E3) and (E6). The representation given by the working equations is generally adequate although, for this cone angle, uniformly a little high. The values of convective heat-transfer coefficient estimated for a laminar boundary layer on a  $30^\circ$  cone are reproduced on this figure for comparison and are computed to be smaller than those for a turbulent boundary layer by factors ranging from 3 to 40, depending on the speed and altitude.

#### Evaluation of Turbulent Convective Energy Fraction

To solve equations (53a) and (53b) we make the assumption that when  $\bar{\rho} \geq 1$  the exponential  $e^{-B\bar{\rho}}$  is so small that we may substitute unity for  $(1 + \xi_t e^{-B\bar{\rho}})$ . With this simplification equations (53a) and (53b) become

for

$$V \leq \frac{7500}{\sin \theta_W}$$

$$\begin{aligned} \eta_t = \frac{B^{0.204}}{r_b^{0.148}} & \left[ \frac{c_{t_1}}{V_E^{k_1}} \left( \frac{\theta_C \cos \theta_C}{2 \sin^{k_1} \theta_W \sin^3 \theta_C} \right) \int_{\chi=0}^{\infty} \left( \frac{1 - \sigma_t}{1 + \xi_t e^{-\chi}} + \sigma_t \right) \frac{e^{-(1+\frac{k_1}{2})\chi}}{\chi^{0.204}} d\chi \right. \\ & \left. - \frac{c_{t_1}}{V_E^{k_1}} \left( \frac{\theta_C \cos \theta_C}{2 \sin^{k_1} \theta_W \sin^3 \theta_C} \right) \int_B^{\infty} \frac{e^{-(1+\frac{k_1}{2})\chi}}{\chi^{0.204}} d\chi \right] \quad (E13) \end{aligned}$$

and for

$$V \geq \frac{7500}{\sin \theta_W}$$

$$\begin{aligned}
\eta_t = & \frac{B^{0.204}}{r_b^{0.148}} \left[ \frac{c_{t1}}{V_E^{k_1}} \left( \frac{\theta_C \cos \theta_C}{2 \sin^{k_1} \theta_W \sin^3 \theta_C} \right) \int_{\chi=2 \ln \left( \frac{V_E \sin \theta_W}{7500} \right)}^{\infty} \left( \frac{1 - \sigma_t}{1 + \xi_t e^{-\chi}} + \sigma_t \right) \frac{e^{-(1+\frac{k_1}{2})\chi}}{\chi^{0.204}} d\chi \right. \\
& + \frac{c_{t2}}{V_E^{k_2}} \left( \frac{\theta_C \cos \theta_C}{2 \sin^{k_2} \theta_W \sin^3 \theta_C} \right) \int_0^{2 \ln \left( \frac{V_E \sin \theta_W}{7500} \right)} \left( \frac{1 - \sigma_t}{1 + \xi_t e^{-\chi}} + \sigma_t \right) \frac{e^{-(1+\frac{k_2}{2})\chi}}{\chi^{0.204}} d\chi \\
& \left. - \frac{c_{t1}}{V_E^{k_1}} \left( \frac{\theta_C \cos \theta_C}{2 \sin^{k_1} \theta_W \sin^3 \theta_C} \right) \int_B^{\infty} \frac{e^{-(1+\frac{k_1}{2})\chi}}{\chi^{0.204}} d\chi \right] \quad (E14)
\end{aligned}$$

where

$$\chi = B\bar{\rho}$$

In equation (E14), the first two integral terms, in addition to being functions of  $\sigma_t$  and  $\xi_t$ , are functions of  $\theta_C$  and  $V_E$  in a way which is not easily separable. For the purposes of this paper it was deemed advisable to leave the summation in this inseparable form so that a two-entry table is required for tabulation, and each table, in turn, must be made up for a particular value of  $\sigma_t$  and  $\xi_t$ . Accordingly, we may put in the form of equation (55)

$$\eta_t = \frac{B^{0.204}}{r_b^{0.148}} \left[ \Lambda_t - \Phi_t \Psi_t \left( \frac{V_E}{10^4} \right)^{0.66} \right]$$

if we set

$$\Psi_t = \frac{1}{2} c_{t1} \times 10^{-4k_1} \left( \frac{\theta_C \cos \theta_C}{\sin^{k_1} \theta_W \sin^3 \theta_C} \right) = 0.202 \times 10^{-3} \left( \frac{\theta_C \sin^{0.66} \theta_W \cos \theta_C}{\sin^3 \theta_C} \right) \quad (E15)$$

$$\Phi_t = \int_B^{\infty} \frac{e^{-0.67\chi}}{\chi^{0.204}} d\chi \quad (E16)$$

while for

$$V \leq \frac{7500}{\sin \theta_W}$$

$$\Lambda_t = \frac{c_{t1}}{2V_E^{k_1}} \left( \frac{\theta_C \cos \theta_C}{\sin^{k_1} \theta_W \sin^3 \theta_C} \right) \int_0^{\infty} \left( \frac{1 - \sigma_t}{1 + \xi_t e^{-\chi}} + \sigma_t \right) \frac{e^{-(1+\frac{k_1}{2})\chi}}{\chi^{0.204}} d\chi \quad (E17)$$

and for

$$V \geq \frac{7500}{\sin \theta_W}$$

$$\begin{aligned} \Lambda_t = & \frac{c_{t_1}}{2V_E k_1} \left( \frac{\theta_C \cos \theta_C}{\sin^{k_1} \theta_W \sin^3 \theta_C} \right) \int_{\chi=2\ln\left(\frac{V_E \sin \theta_W}{7500}\right)}^{\infty} \left( \frac{1 - \sigma_t}{1 + \xi_t e^{-\chi}} + \sigma_t \right) \frac{e^{-(1+\frac{k_1}{2})\chi}}{\chi^{0.204}} d\chi \\ & + \frac{c_{t_2}}{2V_E k_2} \left( \frac{\theta_C \cos \theta_C}{\sin^{k_2} \theta_W \sin^3 \theta_C} \right) \int_{\chi=0}^{2\ln\left(\frac{V_E \sin \theta_W}{7500}\right)} \left( \frac{1 - \sigma_t}{1 + \xi_t e^{-\chi}} + \sigma_t \right) \frac{e^{-(1+\frac{k_2}{2})\chi}}{\chi^{0.204}} d\chi \end{aligned} \quad (E18)$$

## APPENDIX F

### RELATION OF THE LIMITING REYNOLDS NUMBER TO THE BALLISTIC

#### COEFFICIENT, CONE ANGLE, AND ENTRY VELOCITY

Since the relationship between flight velocity and air density is a function of the entry velocity and ballistic coefficient  $B$  (eq. (8)), it is evident that the Reynolds number based on free-stream properties will be governed by these factors and the body size.

$$Re_{\infty} = \frac{\rho V r_b}{\mu} = \frac{\rho_o V_E r_b}{\mu} \bar{\rho} e^{-(B/2)\bar{\rho}} \quad (F1)$$

For an isothermal atmosphere in which the free-stream viscosity is constant, and for cases where  $r_b$  is not importantly diminished by ablation, the maximum value of  $Re_{\infty}$  on the trajectory can be found by setting the derivative  $dRe_{\infty}/d\bar{\rho}$  equal to zero to obtain

$$Re_{\infty \max} = \frac{2}{Be} \frac{\rho_o V_E r_b}{\mu} \quad (F2)$$

where  $e$  is the Napierian base. Equation (F2) is plotted in figure 44 for an entry velocity of 30 km/sec and  $r_b = 1$  meter, for which case values of  $Re_{\infty \max}$  in excess of 10 million occur at  $B$  less than about 265. It is of interest that the peak Reynolds number according to equation (F1) occurs at a velocity  $V = V_E/e$ , and at a density  $\bar{\rho} = 2/B$ . The Reynolds number profile defined by equation (F1) is plotted in figure 45 as a function of the velocity ratio  $V/V_E$ .

It remains to relate the free-stream Reynolds number defined by equation (F1) to the Reynolds number based on boundary-layer edge properties and slant length,  $Re_{\epsilon} = \rho_{\epsilon} u_{\epsilon} x / \mu_{\epsilon}$ . All flow-field properties needed for this purpose are obtainable from the calculations of the conical flow field described in appendix B, with the use of air properties tabulated in references 36, 37, and 38. Ratios of local to free-stream Reynolds number obtained from these calculations are shown in figure 46.

Since the present purpose was to define limiting values of  $B$  below which the local Reynolds number will exceed 5, 10, or 20 million, the following procedure was applied. Assume for the moment that the Reynolds number ratios of figure 46 are functions of cone angle only, independent of speed and altitude. Then the maximum of the local Reynolds number will occur simultaneously with the maximum of the free-stream Reynolds number, and

$$Re_{\epsilon \max} = Re_{\max} = Re_{\infty \max} \frac{Re_{\epsilon}}{Re_{\infty}} = \frac{2}{Be} \frac{\rho_o V_E r_b}{\mu} \frac{Re_{\epsilon}}{Re_{\infty}} \quad (F3)$$



If  $Re_{\epsilon_{\max}}$  is not to exceed the limiting Reynolds number  $Re_{lim}$  of the text, then the former is replaced in equation (F3) by the latter to give the value

$$B = \frac{2}{eRe_{lim}} \frac{\rho_o V_E r_b}{\mu} \frac{Re_{\epsilon}}{Re_{\infty}} \quad (F4)$$

corresponding to the specified Reynolds number limitation. Lower values of  $B$  will result in local Reynolds numbers exceeding  $Re_{lim}$ .

As may be seen from figure 46, the assumption that  $Re_{\epsilon}/Re_{\infty}$  is a constant for any cone angle is reasonable for cone angles up to  $40^\circ$  at speeds up to 25 km/sec, and to higher speeds for smaller cone angles. Obviously, large departures from constant  $Re_{\epsilon}/Re_{\infty}$  occur on the  $40^\circ$  and  $55^\circ$  cones at speeds above 20 to 25 km/sec. The error resulting from the assumption of constant  $Re_{\epsilon}/Re_{\infty}$  in this latter range is not important for present purposes, however, because the optimum cone angle in the very high entry speed range is less than  $33^\circ$  (see fig. 10). Hence, the value of  $B$  calculated from equation (F4) by use of this assumption will be in serious error only for conditions well away from the optimum, and the effect on conditions near the optimum will be small. It is of interest to note that the effect of the nonconstancy of  $Re_{\epsilon}/Re_{\infty}$  on the dashed curves of figure 9 is to cause them to rise more rapidly than shown for  $\theta_C$  greater than the optimum. The significance of this is that the turbulent flow boundary is raised to higher values of  $B$  for the large angled cones. Since these cone angles would presumably not be used, this may be of academic interest only. It is clear that by use of equation (F1) and figure 46, values of maximum local Reynolds number free of the above assumption can be obtained if desired.

## APPENDIX G

### ARC-JET TESTS OF TEFLON MODELS

Tests to examine qualitatively the extent of the change in dimensions of Teflon models due to laminar convective heating were made in an electrically heated arc-jet stream. The Mach number of the stream was 3.3 and the enthalpy level, 3500 Btu/lb ( $8.1 \times 10^6$  m<sup>2</sup>/sec<sup>2</sup>). Total pressure was set at one atmosphere. The Reynolds number based on model base diameter was 2140 and, accordingly, the flow was laminar. The jet diameter was 2.75 inches (6.8 cm). Stream surveys indicated the enthalpy and stagnation pressure were constant within 5 percent over a 2-inch core (5 cm). This assured uniform flow conditions over the conical test bodies which were 1.5 inches (3.8 cm) in diameter.

The test conditions in this stream are far less intense, of course, than a typical flight vehicle would experience at hyperbolic entry speeds (e.g., in flight with a ballistic parameter of 200, heat rates would be as much as 50 times those in these tests) and the jet enthalpy is so low that radiative heating of these models is trivial. However, the model test results should be indicative of the manner in which convective heating promotes the initial blunting of the apex in flight.

For the flow conditions listed above for the present ablation tests, the following table lists the magnitude of the stagnation-point heat-transfer rates at 1 second after flow was started.

Model designation	$q_{sp}, \frac{\text{Btu/sec}}{\text{ft}^2}$	$q_{sp}, \frac{\text{kg}}{\text{sec}^2}$
Passive type; c = 0	930	$1.05 \times 10^7$
c = .1	1440	$1.63 \times 10^7$
c = .2	1660	$1.88 \times 10^7$
c = .3	1850	$2.10 \times 10^7$
Extrusion type; 1/16-diameter rod	930	$1.05 \times 10^7$
1/8-diameter rod	930	$1.05 \times 10^7$
1/4-diameter rod	930	$1.05 \times 10^7$

Figure 47 shows the principal dimensions of the passive type models tested. Basically, all of the passive type models are members of the same cusped-cone family. The degree of sharpness of the nose of the cusped cone is determined by the parameter c (see equation, fig. 47). For practical reasons of strength, all models were terminated at a tip diameter of 1/64 inch. The notch on the cylindrical afterbody served as a measuring reference station.

The other type of model tested is shown in figure 48. This model consists of a 45° cone with a cylindrical core of various diameters that could be extruded at constant predetermined rates. Extrusion rates were set by adjusting a D.C. motor-driven drive screw prior to each run. An "optimum" extrusion rate was

found by trial. The optimum rate was defined such that the core tip just kept pace with the ablation that occurred on the conical rays. For this case, the profile shape remains essentially constant with time throughout the run.

The profile shape change with time was found for all models by measurements from shadowgraph pictures taken during the run.

## REFERENCES

1. Ehricke, Krafft A.: Interplanetary Operations, Chap. 8, Space Technology, Howard S. Seifert, ed. John Wiley and Sons, N. Y., 1959.
2. Allen, H. Julian: Gas Dynamics Problems of Space Vehicles. Vol. 2, Proc. NASA-University Conference on the Science and Technology of Space Exploration. NASA SP-11, no. 54, 1962, pp. 251-267.
3. McAdams, William H.: Heat Transmission. Second ed., McGraw-Hill Book Co., N. Y., 1942, pp. 162-164.
4. Allen, H. Julian, and Eggers, A. J., Jr.: A Study of the Motion and Aerodynamic Heating of Ballistic Missiles Entering the Earth's Atmosphere at High Supersonic Speeds. NACA Rep. 1381, 1958. (Supersedes NACA TN 4047.)
5. Kivel, B., and Bailey, K.: Tables of Radiation From High Temperature Air. AVCO-Everett Res. Lab. Res. Rep. 21, Dec. 1957.
6. Meyerott, Roland E.: Radiation Heat Transfer to Hypersonic Vehicles. Lockheed Aircraft Corp. LMSD 2264-R1, Sept. 5, 1958.
7. Camm, J. C., Kivel, B., Taylor, R. L., and Teare, J. D.: Absolute Intensity of Non-Equilibrium Radiation in Air and Stagnation Heating at High Altitudes. AVCO-Everett Res. Lab. Res. Rep. 93, Dec. 1959.
8. Page, William A., Canning, Thomas N., Craig, Roger A., and Stephenson, Jack D.: Measurements of Thermal Radiation of Air From the Stagnation Region of Blunt Bodies Traveling at Velocities Up to 31,000 Feet Per Second. NASA TM X-508, 1961.
9. Canning, Thomas N.: Recent Developments in the Chemistry and Thermodynamics of Gases at Hypervelocities. Vol. 2, Proc. NASA-University Conference on the Science and Technology of Space Exploration. NASA SP-11, no. 56, 1962, pp. 283-290.
10. Page, William A.: Shock-Layer Radiation of Blunt Bodies Traveling at Lunar Return Entry Velocities. IAS Paper 63-41, Jan., 1963.
11. Eggers, Alfred J., Jr., Allen, H. Julian, and Neice, Stanford E.: A Comparative Analysis of the Performance of Long-Range Hypervelocity Vehicles. NACA Rep. 1382, 1958.
12. Chapman, Dean R.: An Approximate Analytical Method for Studying Entry Into Planetary Atmospheres. NASA TR R-11, 1959.
13. Minzner, R. A., Champion, K. S. W., and Pond, H. L.: The ARDC Model Atmosphere, 1959. Air Force Cambridge Research Center, AFCRC TR 59-267, Aug. 1959. (Also available as AFCRC TN 56-204.)

14. Adams, Mac C.: Recent Advances in Ablation. ARS Jour., vol. 29, no. 9, Sept. 1959, pp. 625-632.
15. Riddell, Fredrick R., and Winkler, Howard B.: Meteorites and Re-Entry of Space Vehicles at Meteor Velocities. ARS Jour., vol. 32, no. 10, Oct. 1962, pp. 1523-1530.
16. Bloxsom, D. E., and Rhodes, B. V.: Experimental Effect of Bluntness and Gas Rarefaction on Drag Coefficients and Stagnation Heat Transfer on Axisymmetric Shapes in Hypersonic Flow. Jour. Aero/Space Sci., vol. 29, no. 12, Dec. 1962, pp. 1429-1432.
17. Savin, Raymond C., Gloria, Hermilo R., and Dahms, Richard G.: The Determination of Ablative Properties of Materials in Free-Flight Ranges. NASA TN D-1330, 1962.
18. Lundell, John H., Winovich, Warren, and Wakefield, Roy M.: Simulation of Convective and Radiative Entry Heating. Arthur M. Krill, ed. Advances in Hypervelocity Techniques. Proc. Second Symposium on Hypervelocity Techniques. Plenum Press, N. Y., 1962, pp. 729-748.
19. Eggers, Alfred J., Jr.: The Possibility of a Safe Landing. Chap. 13, Space Technology, Howard S. Seifert, ed. John Wiley and Sons, N. Y., 1959.
20. Nininger, H. H.: Out of the Sky. Dover Pub., N. Y., 1952.
21. Cepřecha, Zď.: Multiple Fall of Přibram Meteorites Photographed. I. Double-Station Photographs of the Fireball and Their Relations to the Found Meteorites. Bulletin of the Astronomical Institutes of Czechoslovakia. Vol. 12, no. 2, 1961, pp. 21-47.
22. Howe, John T., and Viegas, John R.: Solutions of the Ionized Radiating Shock Layer Including Reabsorption and Foreign Species Effects and Stagnation Region Heat Transfer. NASA TR R-159, 1963.
23. Dorrance, William H., and Dore, Frank J.: The Effect of Mass Transfer on the Compressible Turbulent Boundary-Layer Skin Friction and Heat Transfer. Jour. Aero. Sci., vol. 21, no. 6, June 1954, pp. 404-410.
24. Rubesin, Morris W.: An Analytical Estimation of the Effect of Transpiration Cooling on the Heat-Transfer and Skin-Friction Characteristics of a Compressible Turbulent Boundary Layer. NACA TN 3341, 1954.
25. Gross, J. F., Hartnett, J. P., Masson, D. J., and Gazley, Carl, Jr.: A Review of Binary Boundary Layer Characteristics. Rand Corp. RM-2516, June 18, 1959.
26. Meyerott, R. E., Sokoloff, J., and Nicholls, R. W.: Absorption Coefficients of Air. LMSD-288052, Lockheed Missiles and Space Division, Sept. 1959.

27. Armstrong, B. H.: Mean Absorption Coefficients of Air, Nitrogen, and Oxygen From 22,000° to 220,000° K. LMSD-49759, Lockheed Missiles and Space Division, July 15, 1959.
28. Allen, H. Julian: Hypersonic Aerodynamic Problems of the Future. Presented to Fluid Mechanics Panel, AGARD, Brussels, Belgium, April 3-6, 1962.
29. Hochstim, Adolph R.: Gas Properties Behind Shocks at Hypersonic Velocities. I - Normal Shocks in Air. Convair Rep. ZPh (GP)-002, Jan. 1957.
30. Seiff, Alvin: Recent Information on Hypersonic Flow Fields. Vol. 2, Proc. NASA-University Conference on the Science and Technology of Space Exploration. NASA SP-11, no. 55, 1962, pp. 269-282.
31. Ames Research Staff: Equations, Tables, and Charts for Compressible Flow. NACA Rep. 1135, 1953.
32. Romig, Mary F.: Conical Flow Parameters for Air in Dissociation Equilibrium. Convair Res. Rep. no. 7, May 15, 1960.
33. Jahnke, Eugene, and Emde, Fritz: Tables of Functions With Formulae and Curves. Dover Pub., N. Y., 1945.
34. Teare, J. D., Georgiev, S., and Allen, R. A.: Radiation From the Non-Equilibrium Shock Front. AVCO Res. Rep. 112, Oct. 1961.
35. Kemp, Nelson H., Rose, Peter H., and Detra, Ralph W.: Laminar Heat Transfer Around Blunt Bodies in Dissociated Air. Jour. Aero/Space Sci., vol. 26, no. 7, July 1959, pp. 421-430.
36. Anon.: The Thermodynamic Properties of High Temperature Air. Rep. RE-1R-14, Chance Vought Research Center, June 28, 1961.
37. Hansen, C. Frederick: Approximations for the Thermodynamic and Transport Properties of High-Temperature Air. NASA TR R-50, 1959.
38. Ahtye, Warren F., and Peng, Tzy-Cheng: Approximations for the Thermodynamic and Transport Properties of High-Temperature Nitrogen With Shock-Tube Applications. NASA TN D-1303, 1962.
39. Seiff, Alvin: Examination of the Existing Data on the Heat Transfer of Turbulent Boundary Layers at Supersonic Speeds From the Point of View of Reynolds Analogy. NACA TN 3284, 1954.
40. Sommer, Simon C., and Short, Barbara J.: Free-Flight Measurements of Turbulent-Boundary-Layer Skin Friction in the Presence of Severe Aerodynamic Heating at Mach Numbers From 2.8 to 7.0. NACA TN 3391, 1955.

41. Tendeland, Thorval: Effects of Mach Number and Wall-Temperature Ratio on Turbulent Heat Transfer at Mach Numbers From 3 to 5. NACA TN 4236, 1958.
42. Peterson, John B., Jr.: A Comparison of Experimental and Theoretical Results for the Compressible Turbulent-Boundary-Layer Skin Friction With Zero Pressure Gradient. NASA TN D-1795, 1963.

TABLE I.- FUNCTIONS OF  $\theta_C$   
[Code:  $0.76-n = 0.76 \times 10^{-n}$ ;  $0.76+n = 0.76 \times 10^n$ ]

$\theta_C$	$\sin \theta_W$	$C_D$	$\Psi_e$	$\Psi_n$	$\Psi_{l_1}$	$\Psi_{l_2}$	$\Psi_t$
15	0.267	0.13	0.76-1	0.58-2	1.86-3	2.18-3	0.67-1
20	.354	.23	.83-1	1.81-2	1.21-3	1.42-3	.45-1
25	.438	.36	.90-1	.43-1	.86-3	1.01-3	.33-1
30	.519	.50	.98-1	.81-1	.65-3	.77-3	.26-1
35	.595	.66	1.07-1	1.50-1	.52-3	.61-3	2.03-2
40	.667	.82	1.18-1	2.41-1	.42-3	.50-3	1.65-2
45	.734	1.00	1.31-1	.37	.35-3	.41-3	1.35-2
50	.795	1.17	1.47-1	.52	.29-3	.35-3	1.11-2
55	.848	1.34	1.63-1	.70	.25-3	.30-3	.91-2

TABLE II.- FUNCTIONS OF  $V_E \sin \theta_W$   
[Code:  $0.76-n = 0.76 \times 10^{-n}$ ;  $0.76+n = 0.76 \times 10^n$ ;  $V_E$  in meters/sec]

$V_E \sin \theta_W$	$Z_e$	$V_E \sin \theta_W$	$Z_e$
6,000	2.40-4	18,500	.68+2
6,500	.66-3	19,000	.76+2
7,000	1.66-3	19,500	.84+2
7,500	.39-2	20,000	.94+2
8,000	.88-2	20,500	1.02+2
8,500	1.86-2	21,000	1.11+2
9,000	.38-1	21,500	1.20+2
9,500	.74-1	22,000	1.29+2
10,000	1.40-1	22,500	1.39+2
10,500	2.58-1	23,000	1.48+2
11,000	.46	23,500	1.58+2
11,500	.80	24,000	1.68+2
12,000	1.36	24,500	1.77+2
12,500	2.26	25,000	1.87+2
13,000	.37+1	25,500	1.97+2
13,500	.59+1	26,000	2.07+2
14,000	.92+1	26,500	2.16+2
14,500	1.33+1	27,000	2.25+2
15,000	1.86+1	27,500	2.34+2
15,500	2.44+1	28,000	2.43+2
16,000	.31+2	28,500	2.50+2
16,500	.37+2	29,000	2.56+2
17,000	.46+2	29,500	2.64+2
17,500	.52+2	30,000	2.69+2
18,000	.60+2		



TABLE III.- FUNCTIONS OF B  
[Code:  $0.76-n = 0.76 \times 10^{-n}$ ;  $0.76+n = 0.76 \times 10^n$ ]

B	$\Phi_n$	$\Phi_{l_1}$	$\Phi_{l_2}$	$\Phi_t$	B	$\Phi_n$	B	$\Phi_n$
0	0	1.77	2.75	1.56	25	2.29-5	160	.66-4
1	1.87-6	2.79-1	1.00	.66	30	2.59-5	170	.68-4
2	.33-5	.81-1	.54	.31	35	2.86-5	180	.70-4
3	.46-5	2.54-2	.32	1.49-1	40	.31-4	190	.72-4
4	.58-5	.83-2	1.88-1	.73-1	45	.34-4	200	.73-4
5	.69-5	2.78-3	1.15-1	.36-1	50	.36-4	250	.79-4
6	.80-5	.94-3	.71-1	1.78-2	55	.38-4	300	.83-4
7	.90-5	.32-3	.44-1	.89-2	60	.40-4	350	.86-4
8	.99-5	1.12-4	2.74-2	.44-2	65	.42-4	400	.89-4
9	1.09-5	.39-4	1.73-2	2.23-3	70	.44-4	450	.91-4
10	1.18-5	1.37-5	1.09-2	1.12-3	75	.46-4	500	.93-4
11	1.27-5	.48-5	.69-2	.56-3	80	.47-4	600	.95-4
12	1.36-5	1.71-6	.44-2	2.83-4	85	.49-4	700	.97-4
13	1.44-5	.61-6	2.81-3	1.43-4	90	.50-4	800	.98-4
14	1.52-5	2.15-7	1.80-3	.72-4	95	.52-4	900	.98-4
15	1.60-5		1.15-3	.36-4	100	.53-4	1,000	.99-4
16	1.68-5		.74-3	1.84-5	110	.56-4	2,000	1.00-4
17	1.72-5		.47-3	.93-5	120	.58-4	3,000	1.00-4
18	1.82-5		.31-3	.47-5	130	.60-4		
19	1.89-5		1.97-4	2.39-6	140	.62-4		
20	1.96-5		1.27-4	1.21-6	150	.64-4		

TABLE IV.- FUNCTIONS OF  $\xi_l$   
[Code:  $0.76-n = 0.76 \times 10^{-n}$ ;  $0.76+n = 0.76 \times 10^n$ ]

$\xi_l$	$\Omega_{l_1}$	$\Omega_{l_2}$	$\xi_l$	$\Omega_{l_2}$
0	1.77	2.75	90	2.42-1
5	.46	1.04	100	2.29-1
10	2.82-1	.75	110	2.18-1
15	2.06-1	.61	120	2.09-1
20	1.64-1	.53	130	2.00-1
25	1.37-1	.47	140	1.93-1
30	1.18-1	.43	150	1.86-1
35	1.04-1	.39	200	1.61-1
40	.93-1	.37	250	1.43-1
45	.84-1	.35	300	1.31-1
50	.76-1	.33	350	1.21-1
55	.71-1	.31	400	1.13-1
60	.65-1	2.98-1		
65	.61-1	2.86-1		
70	.57-1	2.76-1		
75	.54-1	2.66-1		
80	.51-1	2.57-1		

TABLE V.- VALUES OF  $\Lambda_t$ [Code:  $0.76-n = 0.76 \times 10^{-n}$ ;  $0.76+n = 0.76 \times 10^n$ ]

(a) Subliming Teflon ablator, $K_t = 4 \times 10^{-8} \text{ sec}^2/\text{m}^2$ , $\sigma_t = 0.1$									
$V_E$ , m/sec	$\theta_C$								
	15°	20°	25°	30°	35°	40°	45°	50°	55°
8,000	0.53-1	0.36-1	2.61-2	2.01-2	1.60-2	1.30-2	1.07-2	0.88-2	0.72-2
10,000	.53-1	.35-1	2.60-2	2.00-2	1.59-2	1.29-2	1.06-2	.87-2	.71-2
12,000	.52-1	.35-1	2.56-2	1.98-2	1.57-2	1.27-2	1.04-2	.85-2	.69-2
14,000	.51-1	.35-1	2.53-2	1.95-2	1.54-2	1.24-2	1.01-2	.82-2	.68-2
16,000	.50-1	.34-1	2.49-2	1.91-2	1.51-2	1.21-2	.98-2	.79-2	.64-2
18,000	.50-1	.34-1	2.46-2	1.87-2	1.47-2	1.17-2	.94-2	.77-2	.62-2
20,000	.49-1	.33-1	2.42-2	1.83-2	1.43-2	1.14-2	.92-2	.75-2	.61-2
22,000	.49-1	.33-1	2.38-2	1.80-2	1.40-2	1.11-2	.90-2	.73-2	.59-2
24,000	.49-1	.33-1	2.34-2	1.76-2	1.37-2	1.09-2	.88-2	.71-2	.58-2
26,000	.48-1	.32-1	2.31-2	1.73-2	1.34-2	1.07-2	.86-2	.70-2	.56-2
28,000	.48-1	.32-1	2.28-2	1.70-2	1.32-2	1.05-2	.84-2	.68-2	.55-2
30,000	.48-1	.32-1	2.25-2	1.68-2	1.30-2	1.03-2	.83-2	.67-2	.54-2
(b) Vaporizing quartz ablator, $K_t = 0.5 \times 10^{-8} \text{ sec}^2/\text{m}^2$ , $\sigma_t = 0.1$									
8,000	.82-1	.56-1	.41-1	.31-1	2.50-2	2.03-2	1.66-2	1.37-2	1.12-2
10,000	.90-1	.61-1	.45-1	.34-1	2.73-2	2.22-2	1.82-2	1.49-2	1.22-2
12,000	.96-1	.65-1	.47-1	.37-1	2.90-2	2.35-2	1.91-2	1.56-2	1.26-2
14,000	.99-1	.67-1	.49-1	.38-1	3.00-2	2.41-2	1.95-2	1.58-2	1.28-2
16,000	1.02-1	.69-1	.50-1	.39-1	3.04-2	2.42-2	1.95-2	1.58-2	1.27-2
18,000	1.03-1	.70-1	.51-1	.39-1	3.03-2	2.41-2	1.94-2	1.56-2	1.26-2
20,000	1.04-1	.70-1	.51-1	.39-1	3.00-2	2.38-2	1.91-2	1.54-2	1.25-2
22,000	1.05-1	.71-1	.51-1	.38-1	2.97-2	2.35-2	1.89-2	1.52-2	1.23-2
24,000	1.05-1	.70-1	.50-1	.38-1	2.92-2	2.31-2	1.86-2	1.50-2	1.21-2
26,000	1.05-1	.70-1	.50-1	.37-1	2.88-2	2.27-2	1.83-2	1.47-2	1.19-2
28,000	1.04-1	.69-1	.49-1	.37-1	2.83-2	2.24-2	1.79-2	1.45-2	1.17-2
30,000	1.04-1	.68-1	.48-1	.36-1	2.78-2	2.20-2	1.76-2	1.42-2	1.15-2



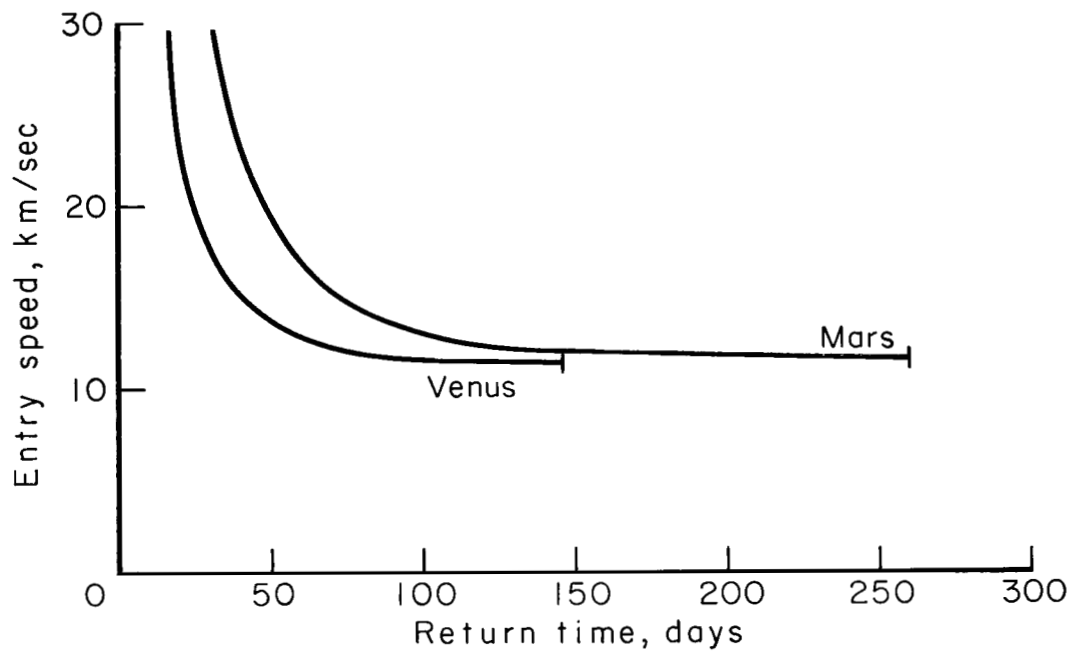


Figure 1.- Earth entry speed for minimum transit time from Mars and Venus.

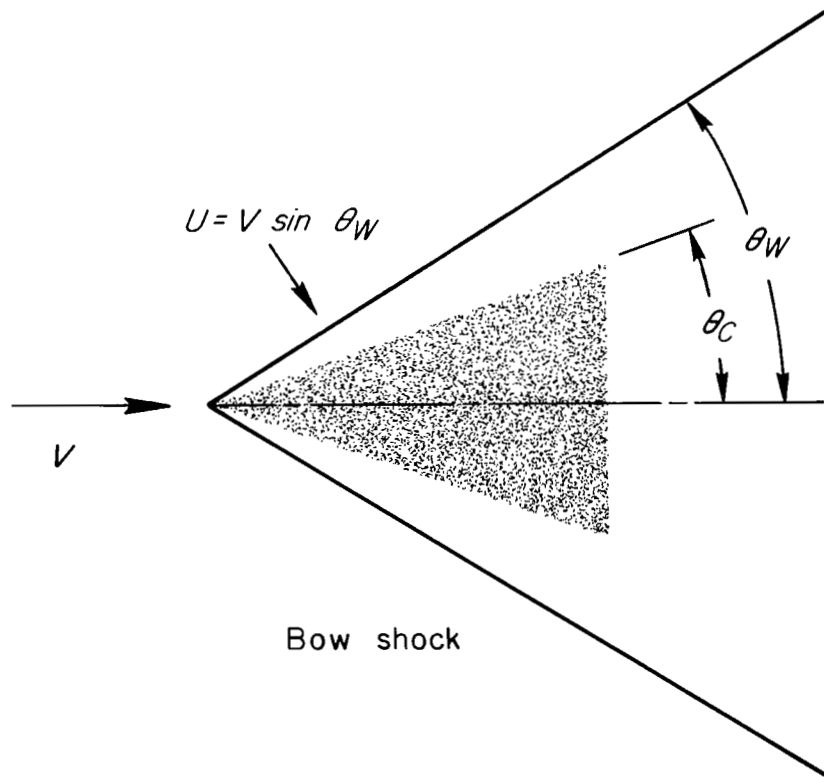


Figure 2.- Velocity vectors for conical bodies.

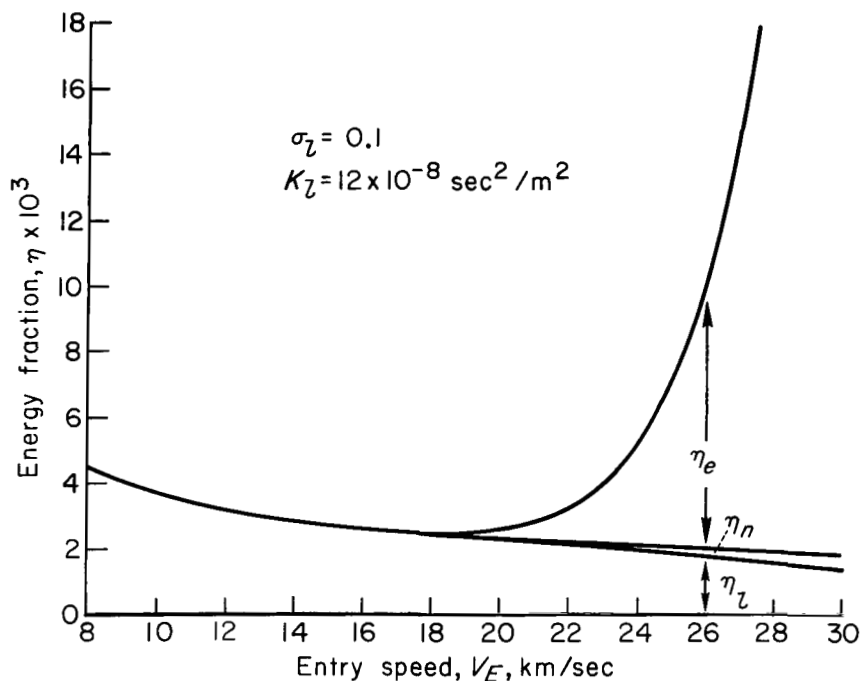


Figure 3.- Variation of the laminar energy fraction with entry speed for a 30° half-angle cone with a ballistic parameter of 200 and a Teflon ablator.

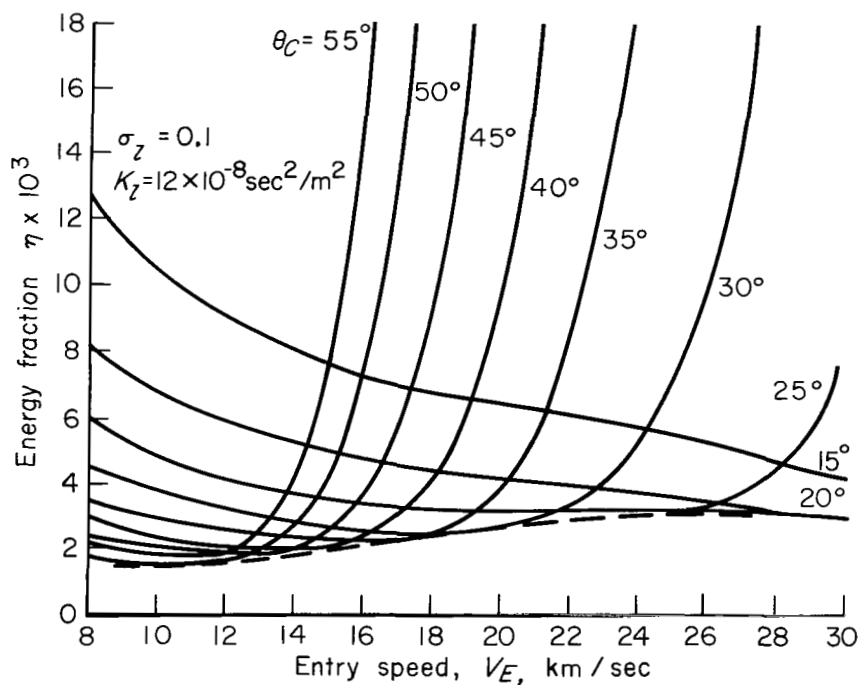
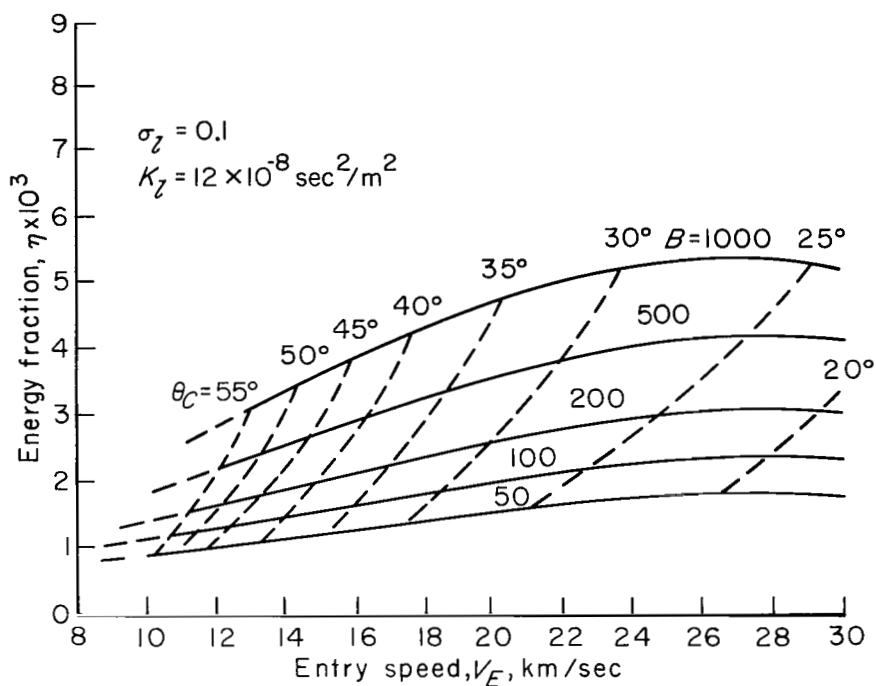
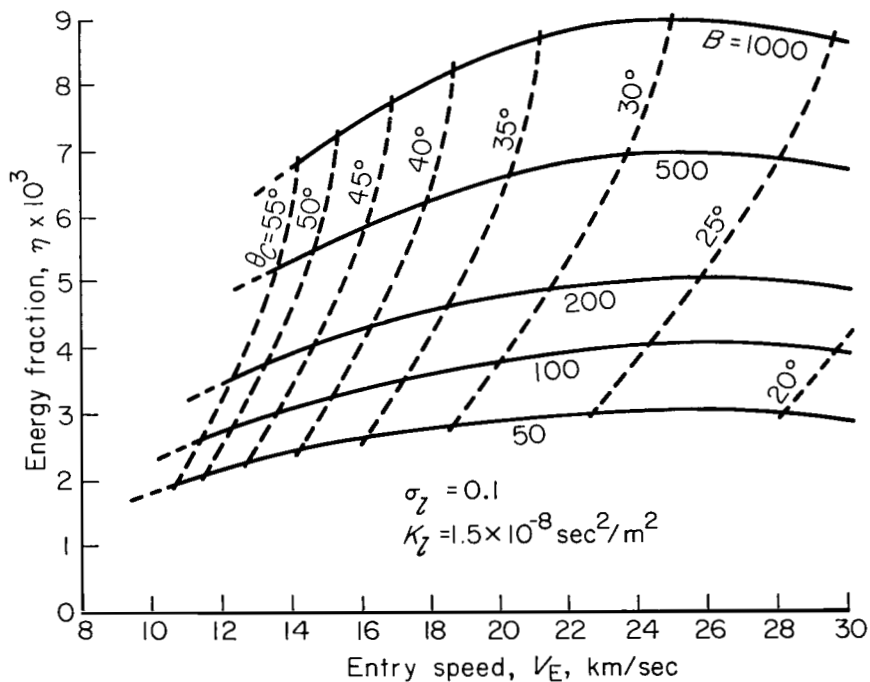


Figure 4.- Variation of the laminar energy fraction with entry speed for cones having a ballistic parameter of 200, Teflon ablators, and various cone half-angles.



(a) Teflon ablator.



(b) Vaporizing quartz ablator.

Figure 5.- Variation of the envelope values of laminar energy fraction with entry speed and ballistic parameter.

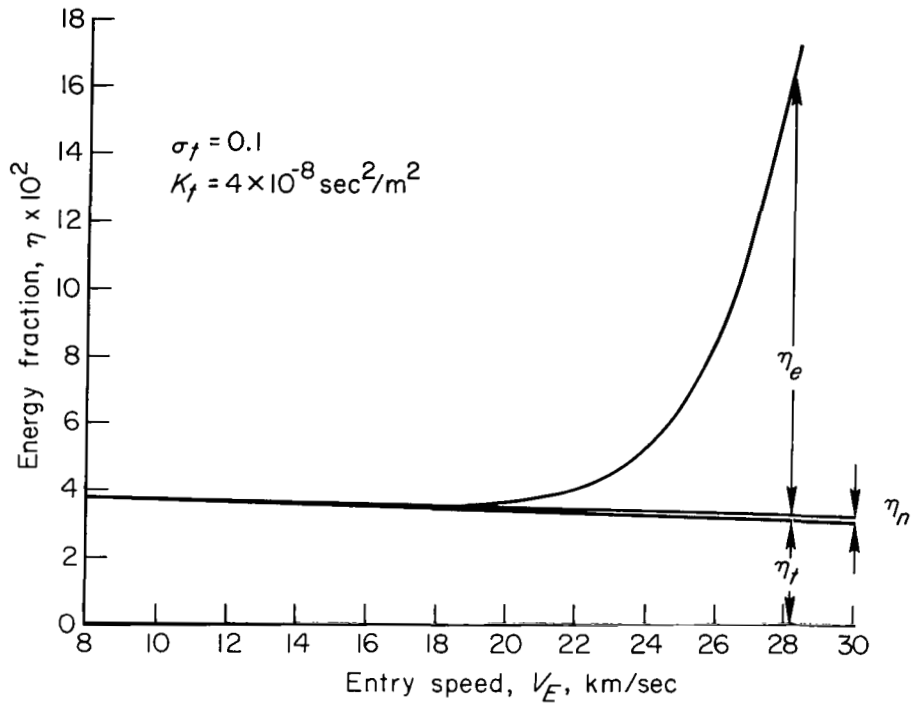


Figure 6.- Variation of the turbulent energy fraction with entry speed for a  $30^\circ$  half-angle cone with a ballistic parameter of 20 and a Teflon ablator.

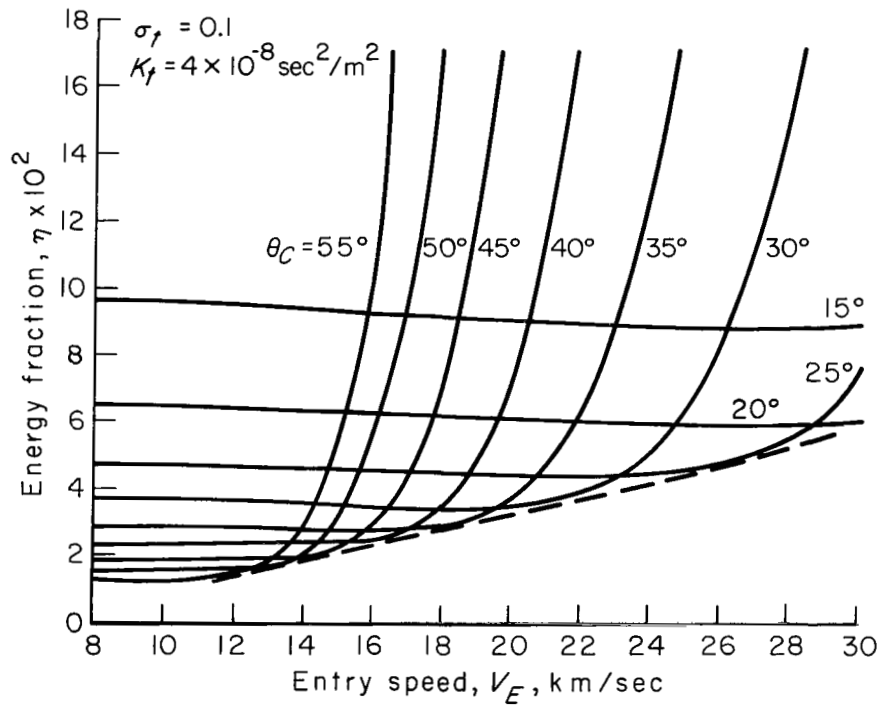
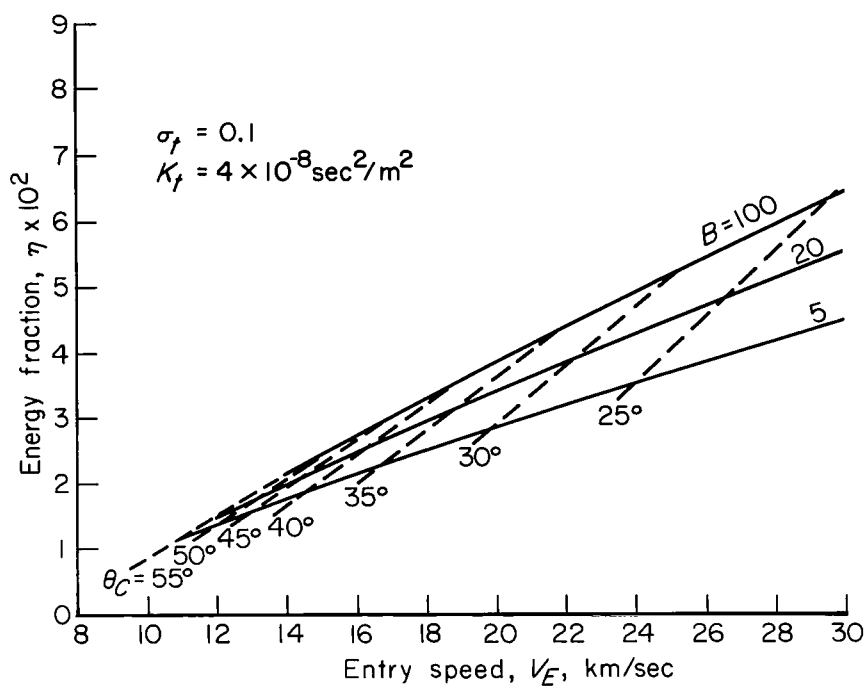
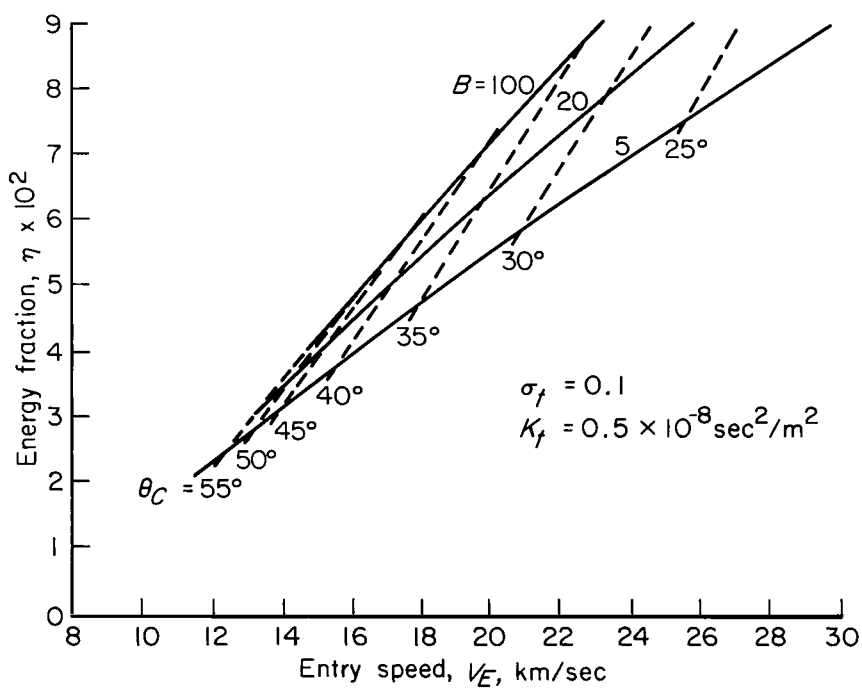


Figure 7.- Variation of the turbulent energy fraction with entry speed for cones having a ballistic parameter of 20, Teflon ablators, and various cone half-angles.



(a) Teflon ablator.



(b) Vaporizing quartz ablator.

Figure 8.- Variation of the envelope values of turbulent energy fraction with entry speed and ballistic parameter.



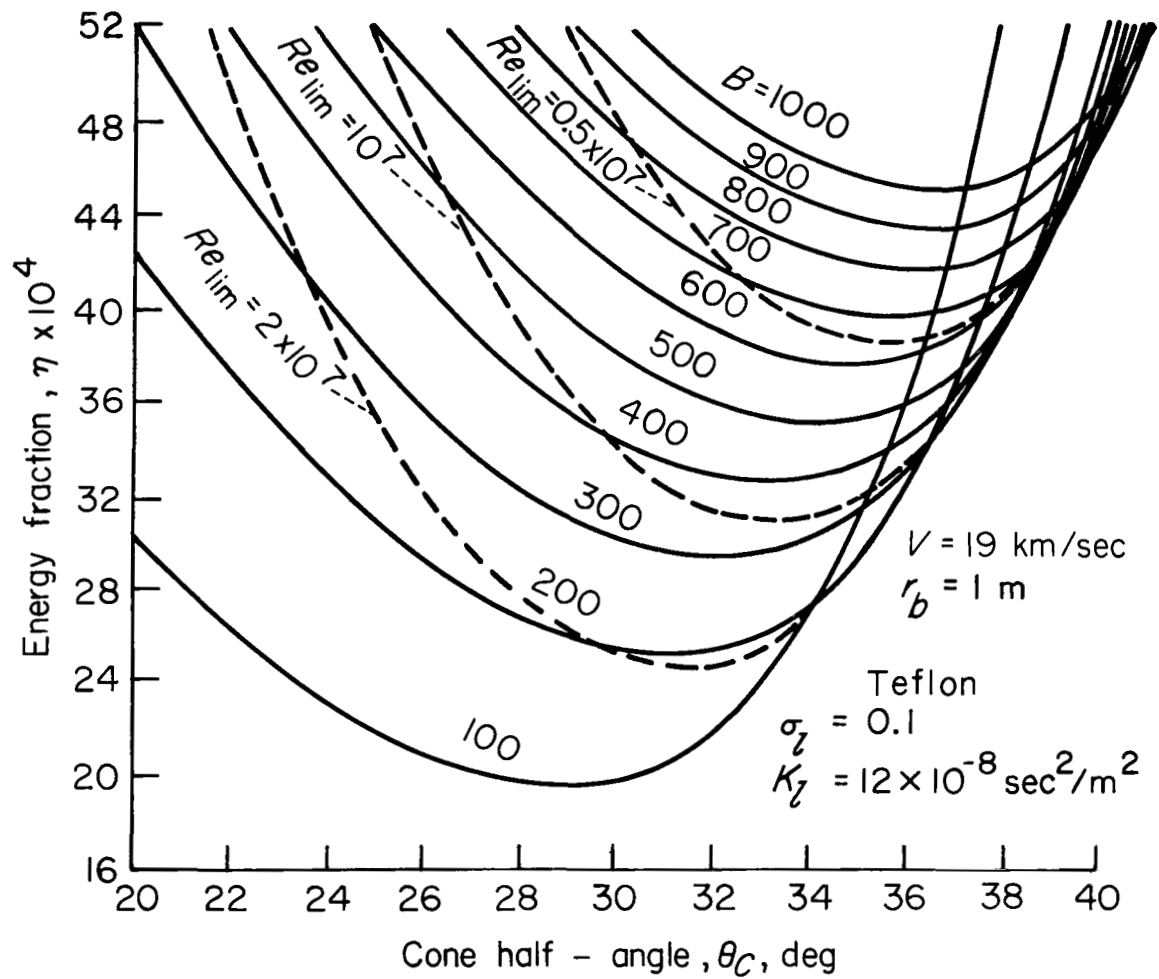


Figure 9.- Example of a plot for obtaining optimum laminar energy fractions and allied factors for three limit Reynolds numbers.

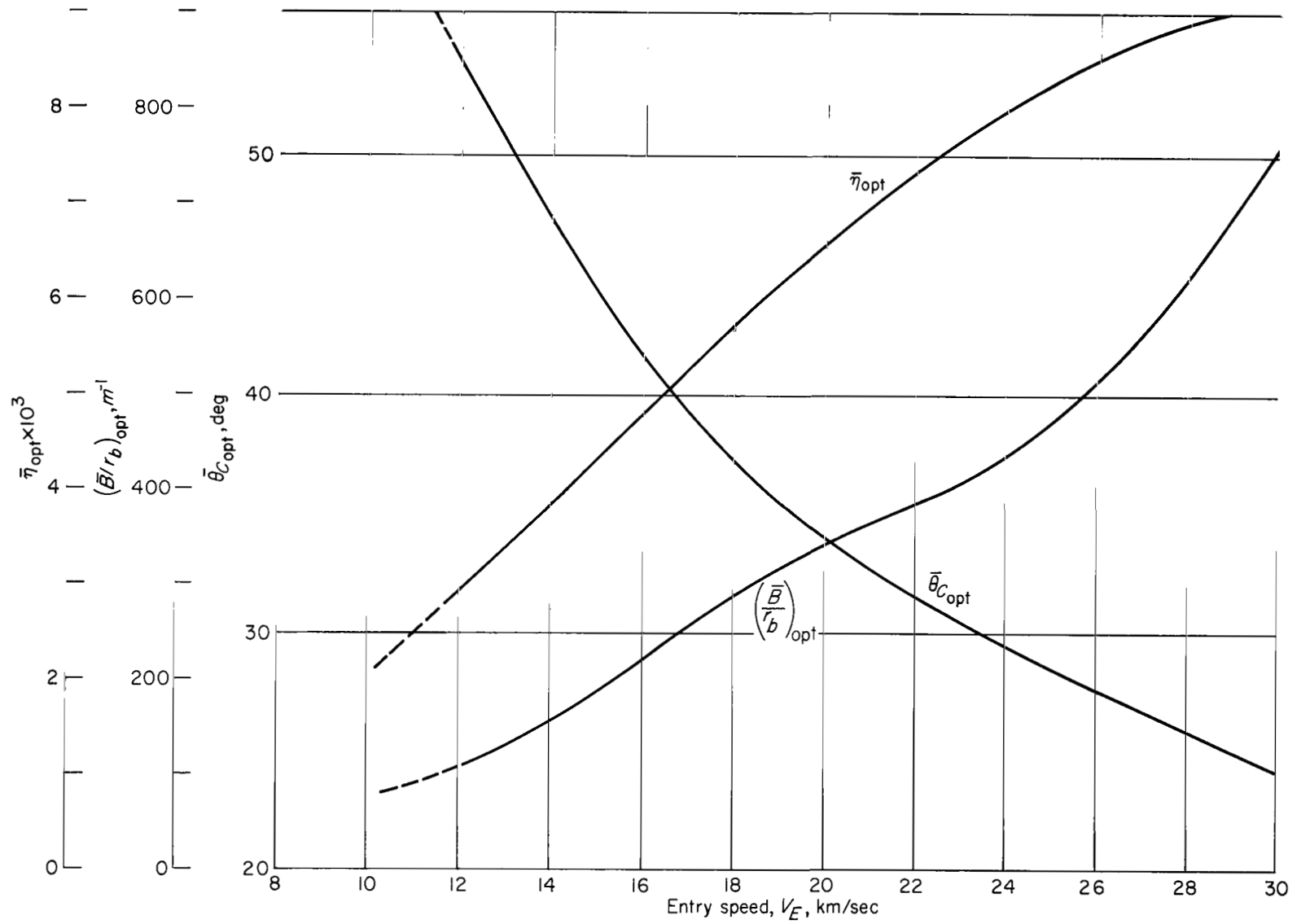


Figure 10.- Constants for evaluation of optimum conical bodies with laminar flow.

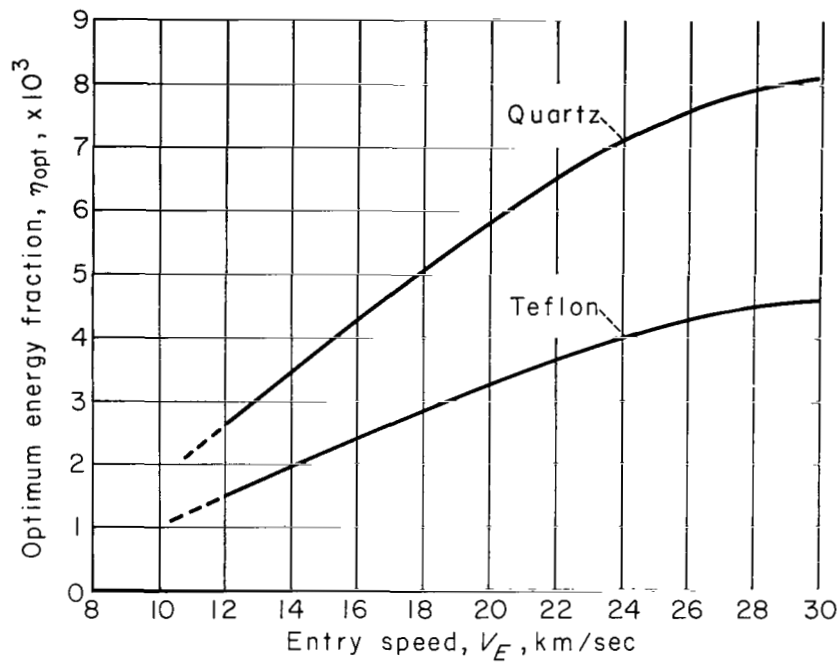


Figure 11.- Comparison of optimum energy fractions of Teflon and vaporizing quartz for a limit Reynolds number of  $10^7$ .

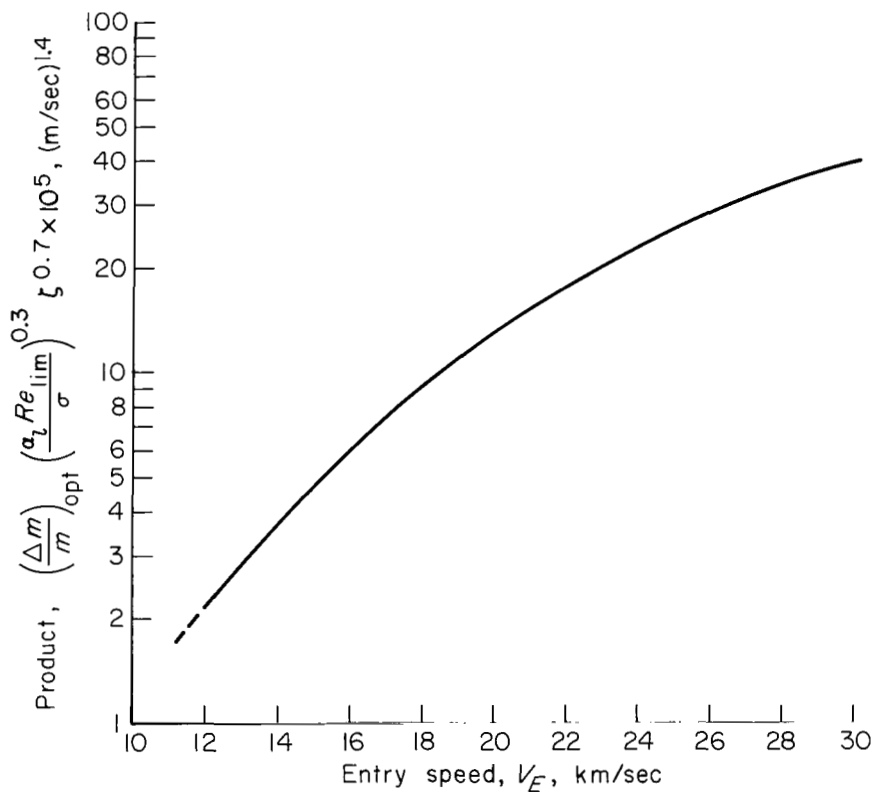


Figure 12.- Generalized mass-loss factor as a function of entry speed.

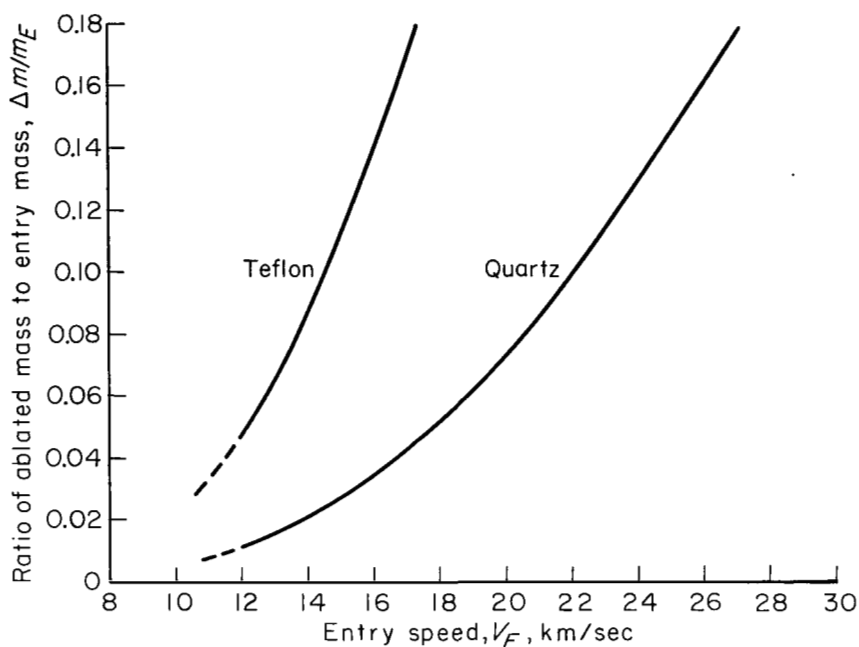


Figure 13.- Comparison of the mass-loss ratios of Teflon and vaporizing quartz for a limit Reynolds number of  $10^7$ .

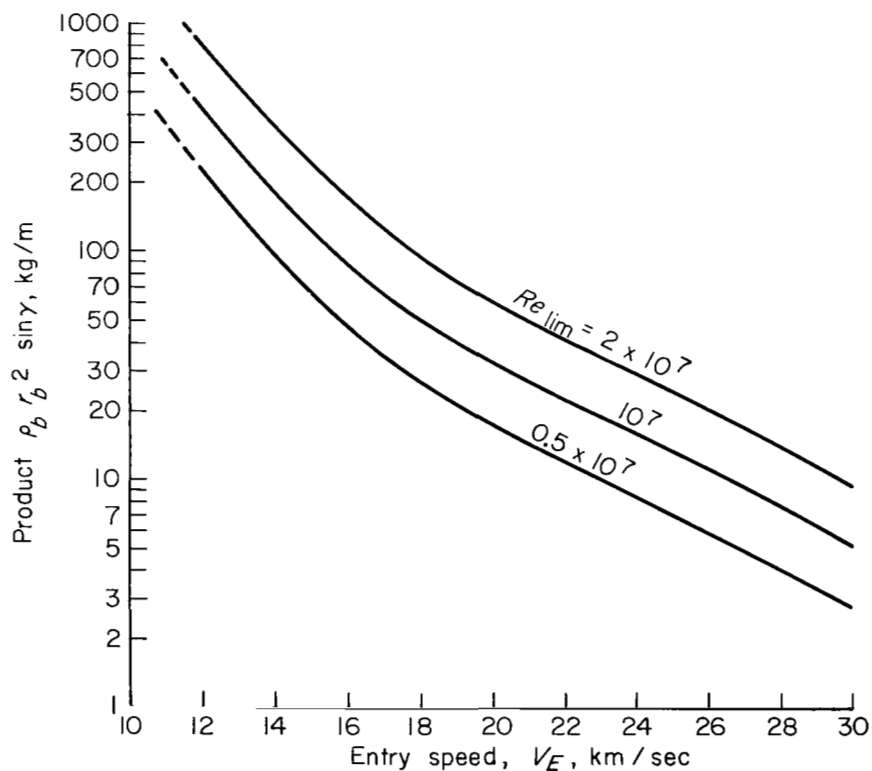


Figure 14.- Variation of a factor involving vehicle density, vehicle size, and trajectory angle with entry speed.

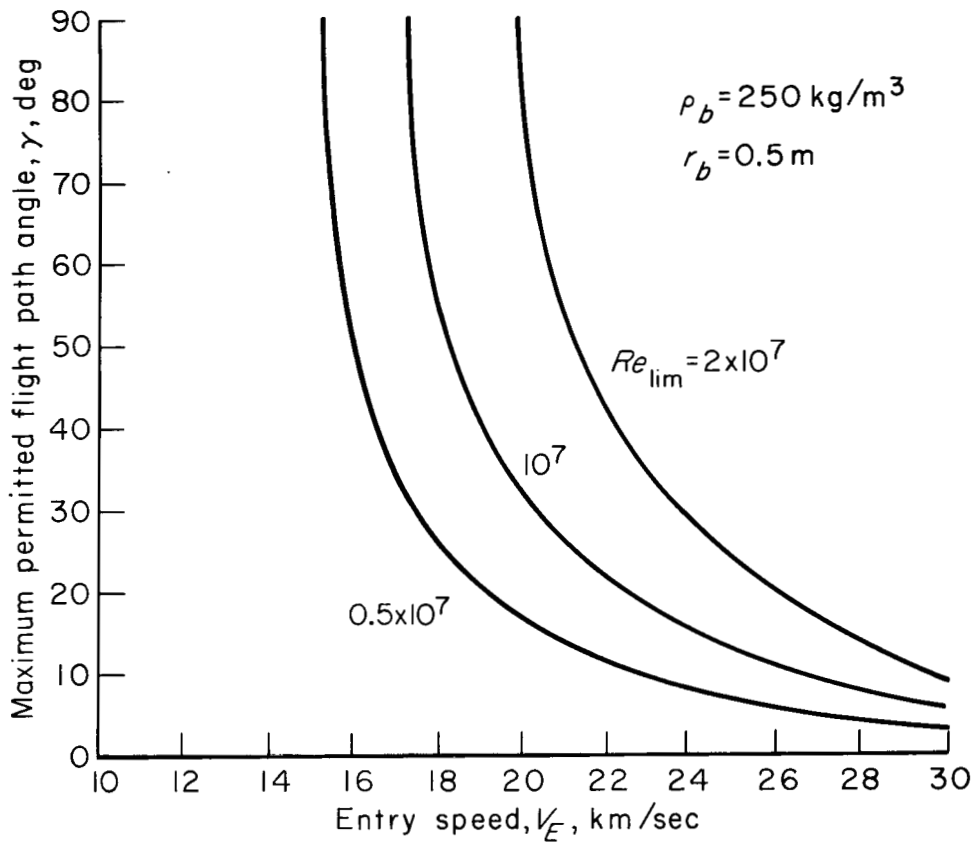


Figure 15.- Trajectory angle requirements for maintenance of laminar flow for an entry body having typical space-probe characteristics.

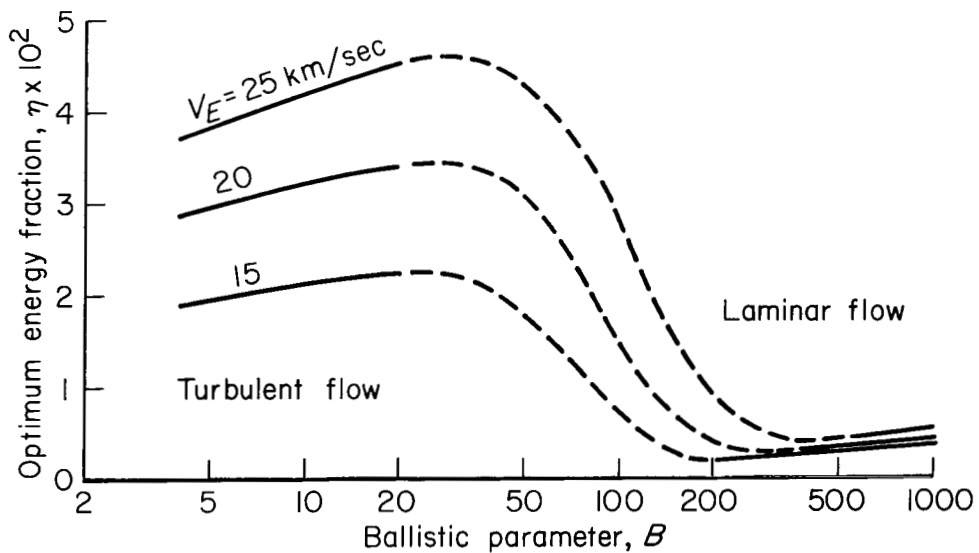


Figure 16.- Variation of minimum energy fraction with ballistic parameter for several entry speeds.

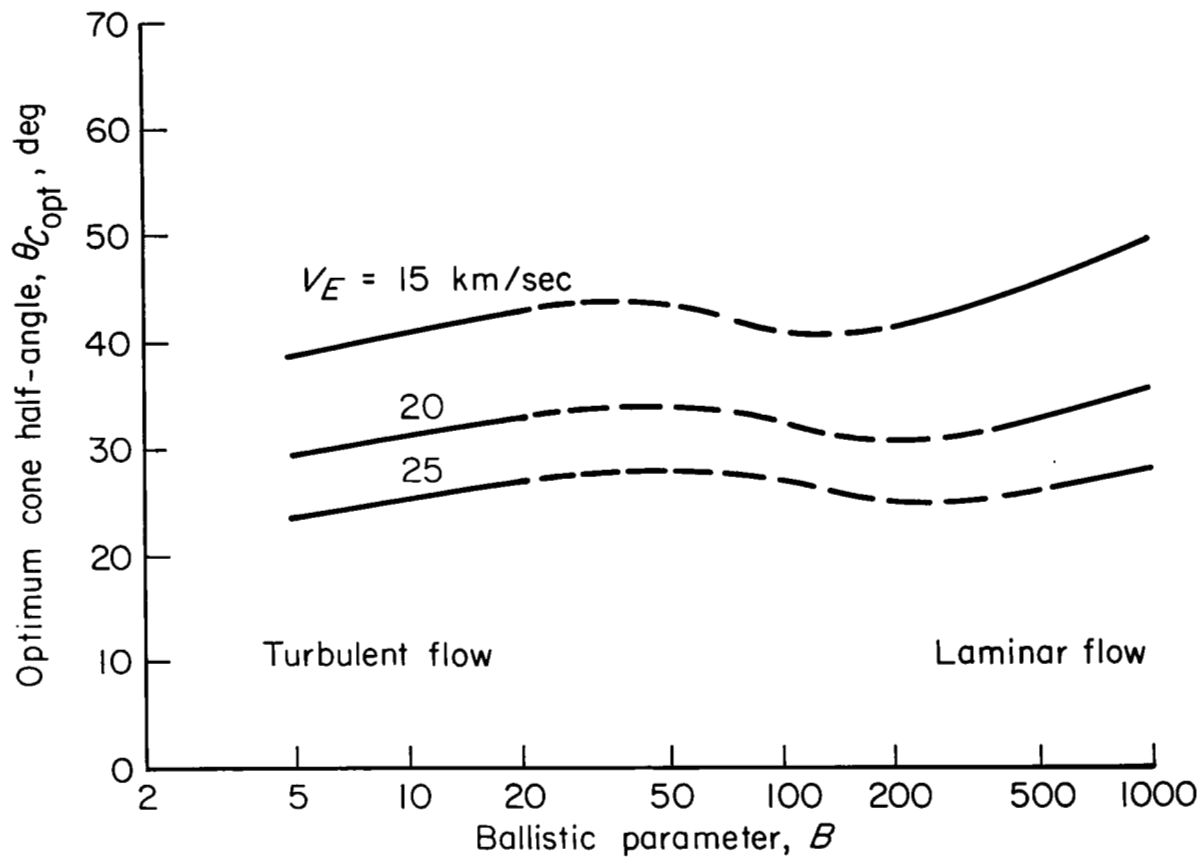
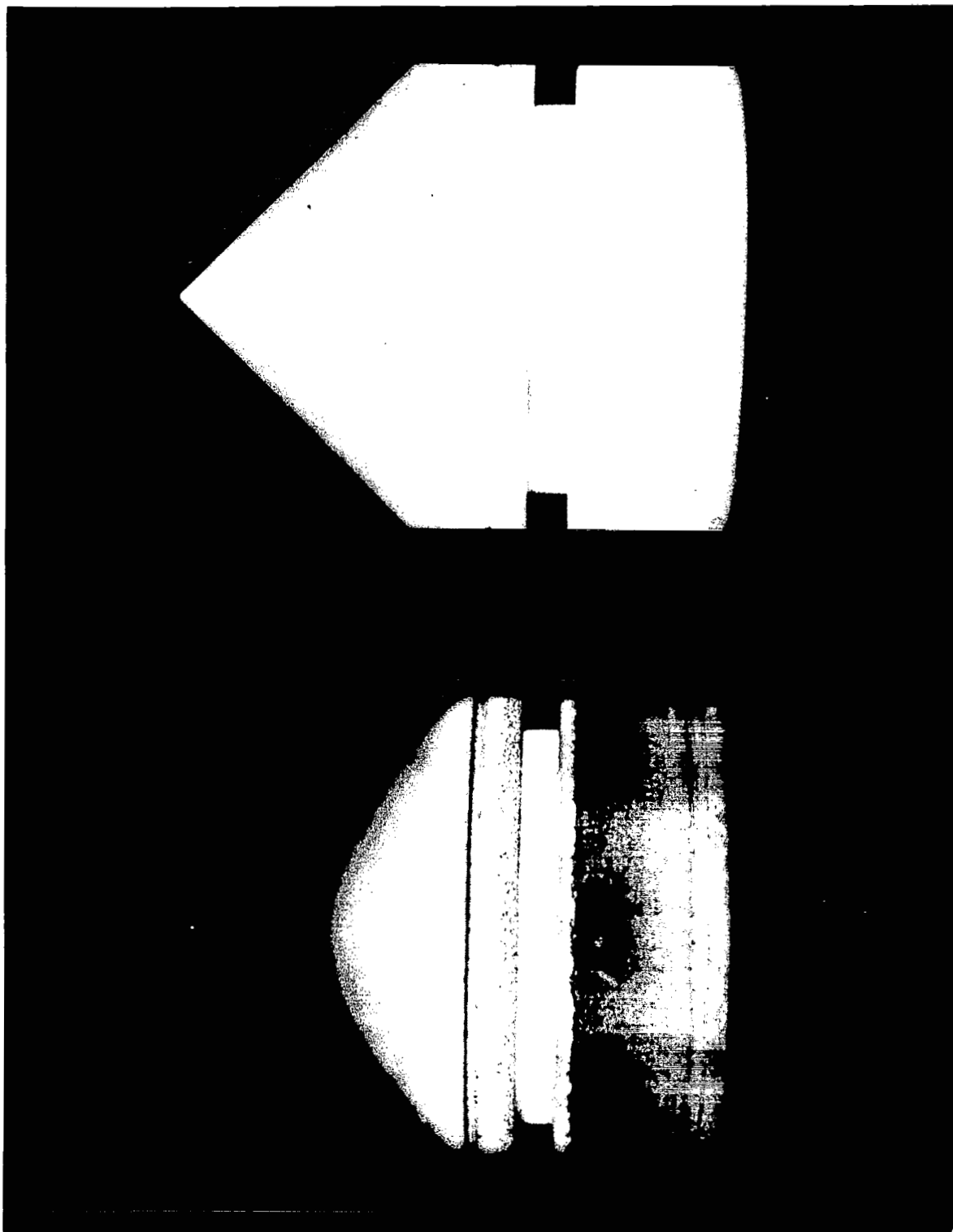


Figure 17.- Variation of cone half-angle corresponding to minimum energy fraction with ballistic parameter for several entry speeds.



A-30693

Figure 18.- Conical body before and after exposure to arc-jet stream;  
 $h_T = 3500$  Btu/lb;  $p_{sp} = 0.114$  atm;  $M = 3.3$ ; exposure time = 18 sec.

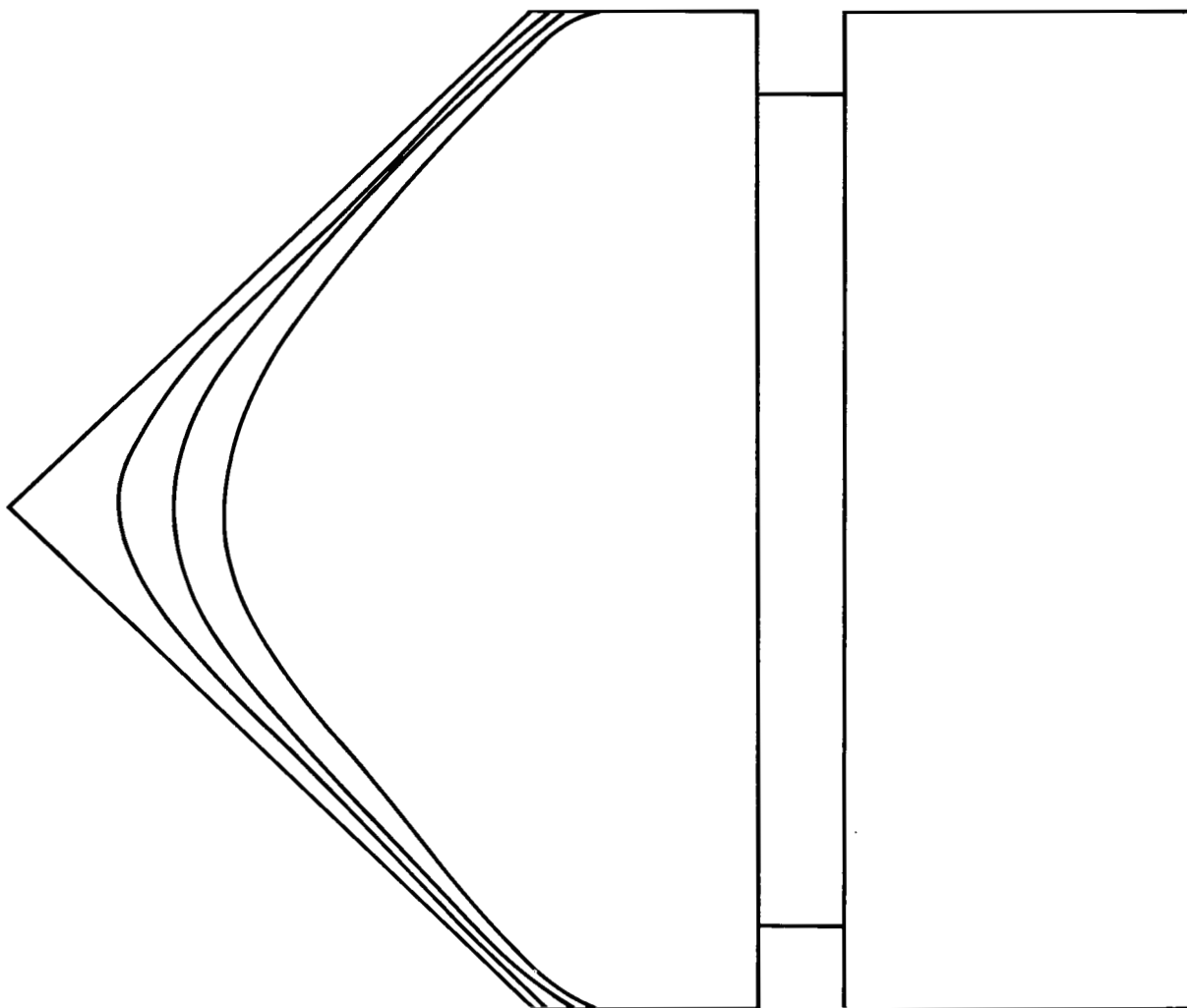
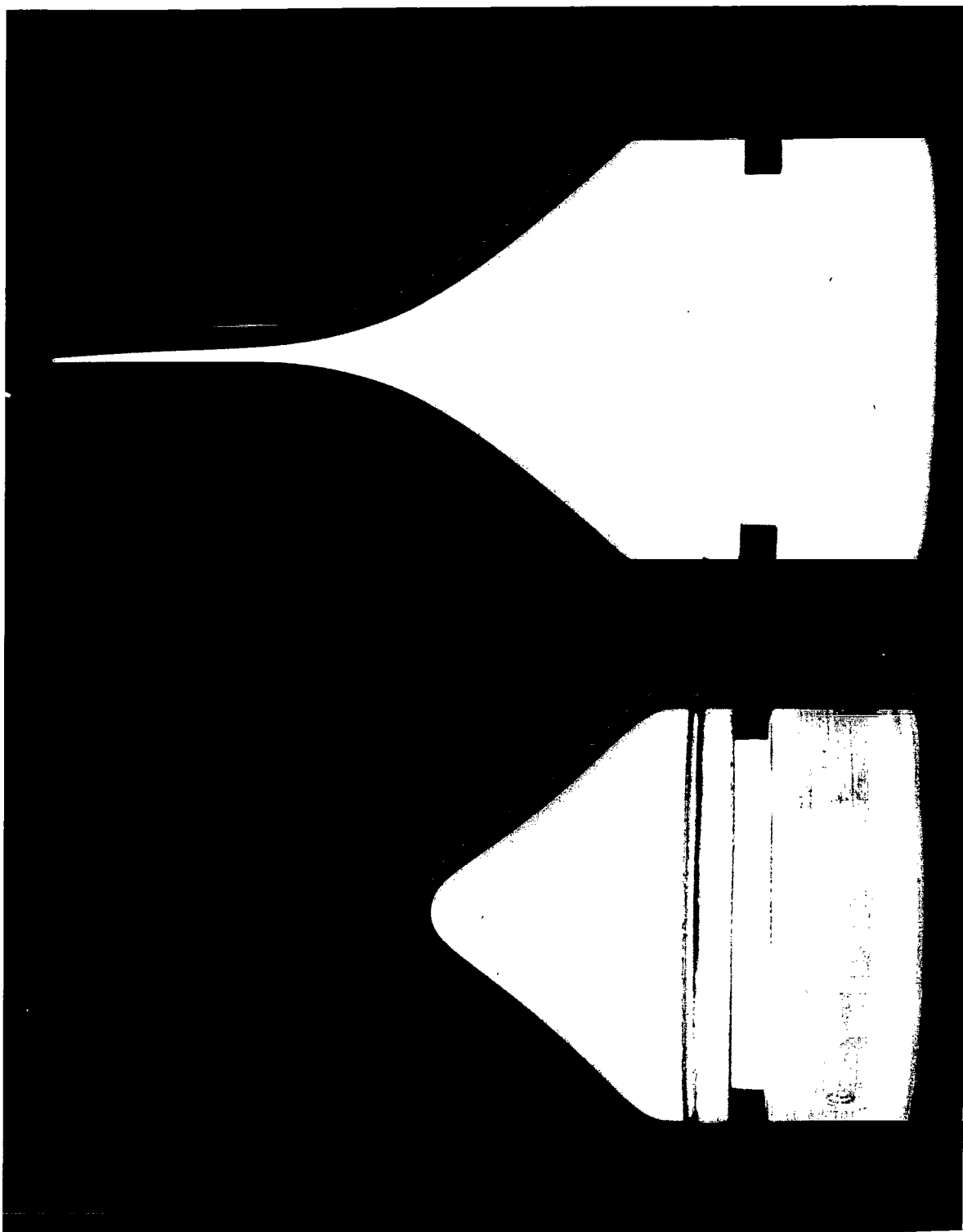


Figure 19.- Profile shape change during ablation for  $45^\circ$  conical body;  
base radius = 0.75 inch; time interval = 6 sec.





A-30694

Figure 20.- Cusped-cone shape ( $c = 0.1$ ) before and after exposure to arc-jet stream;  $h_T = 3500$  Btu/lb;  $p_{sp} = 0.114$  atm;  $M = 3.3$ ; exposure time = 18 sec.

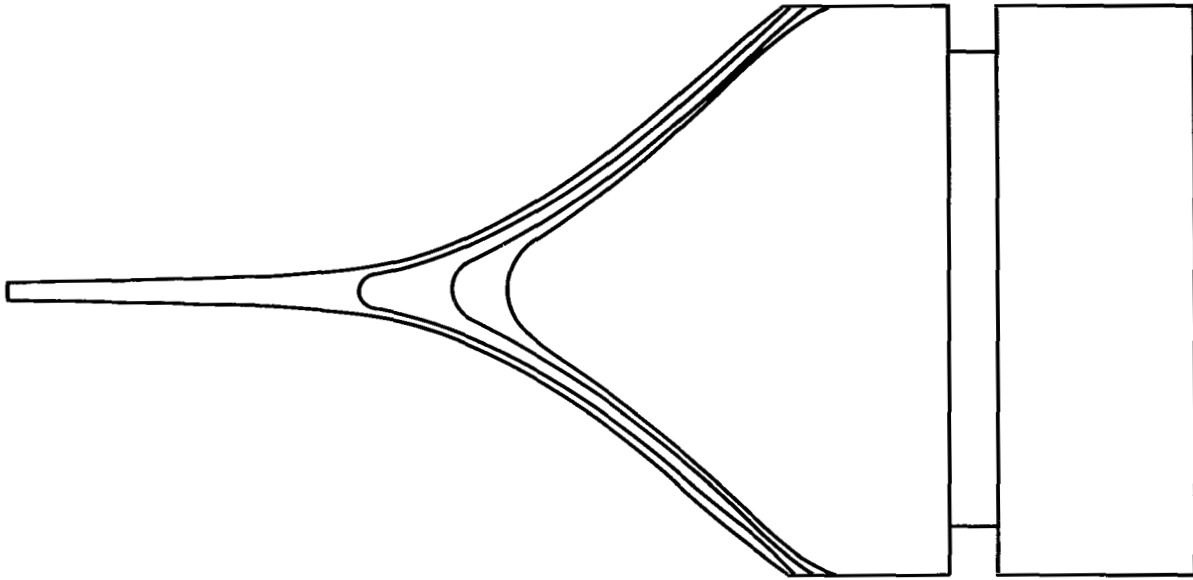
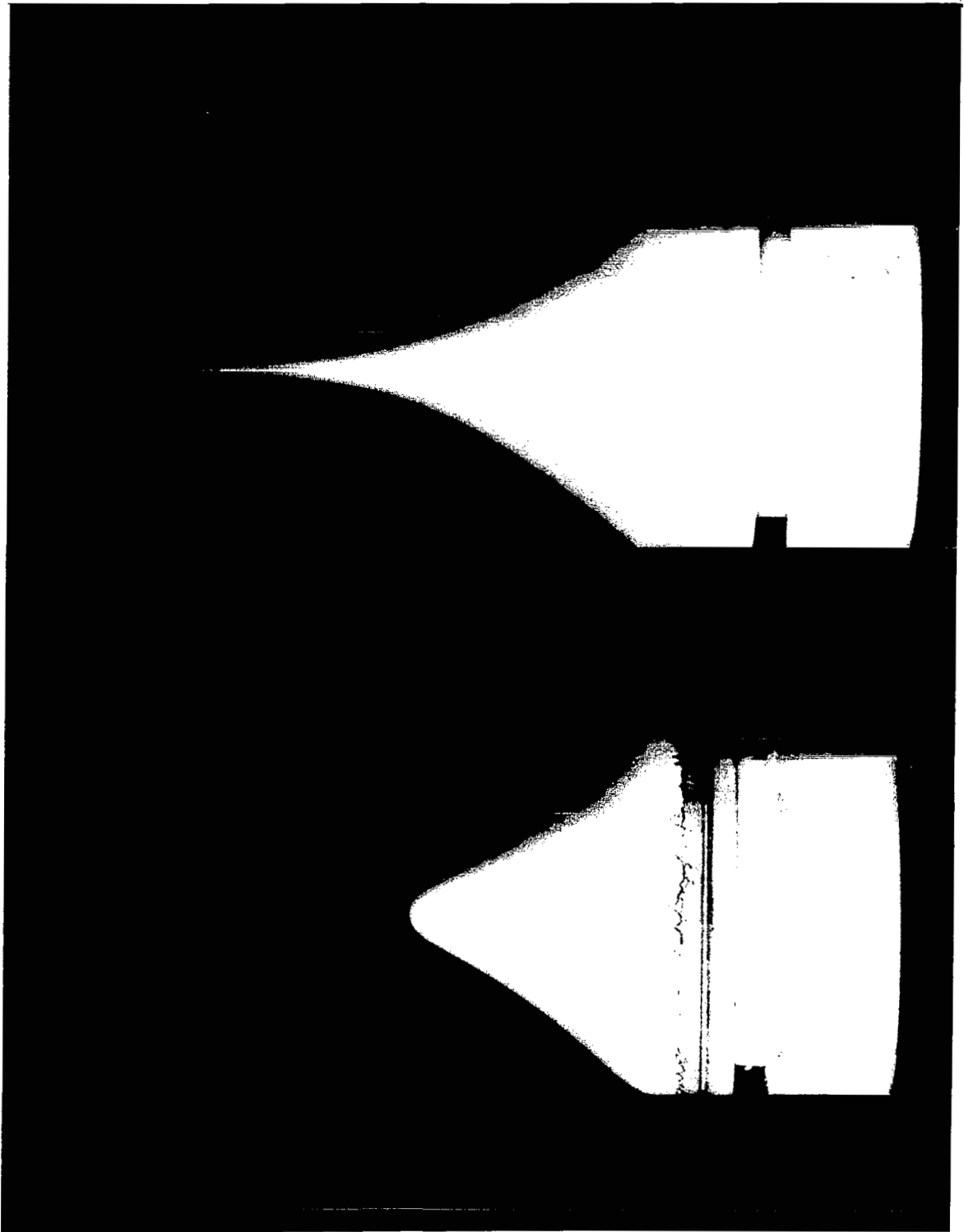


Figure 21.- Profile shape change during ablation for the cusped-cone body  
( $c = 0.1$ ); base radius = 0.75 inch; time interval = 6 sec.



A-30842

Figure 22.- Cusped-cone shape ( $c = 0.3$ ) before and after exposure to arc-jet stream;  $h_T = 3500$  Btu/lb;  $p_{sp} = 0.114$  atm;  $M = 3.3$ ; exposure time = 18 sec.

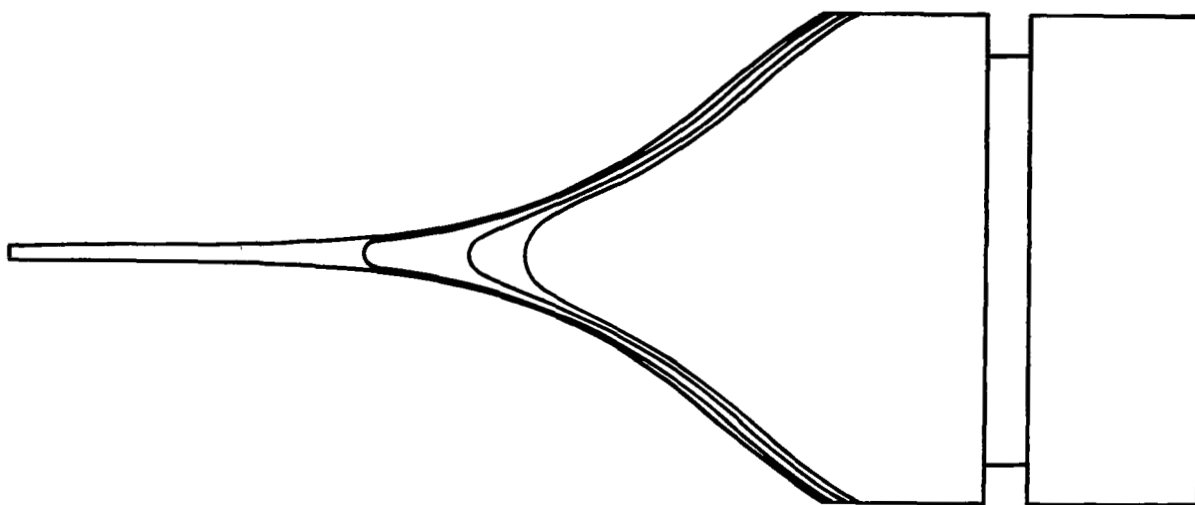
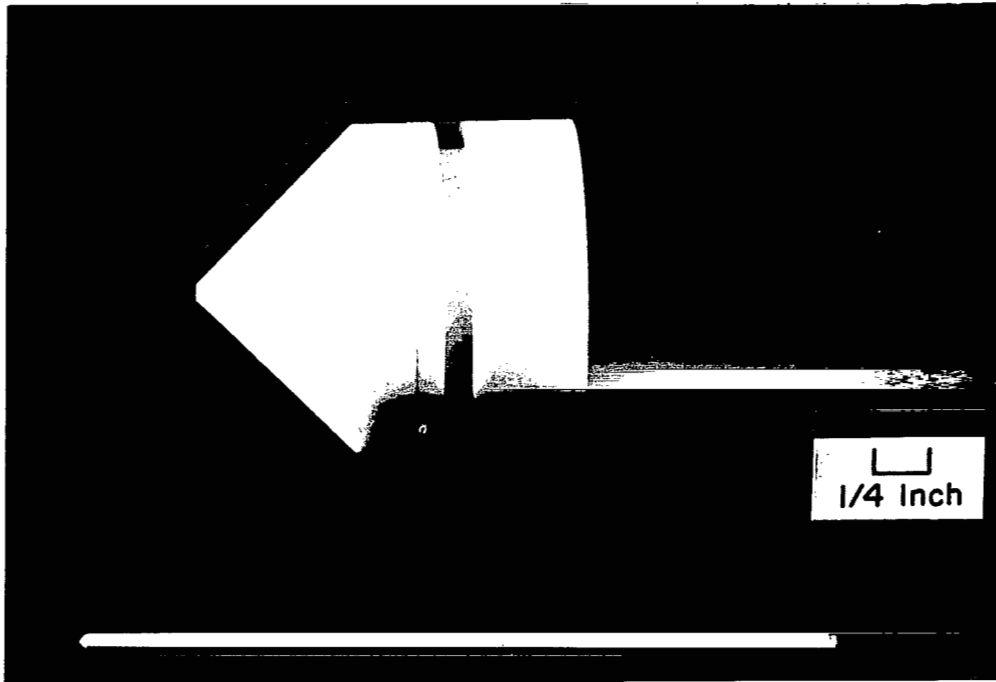
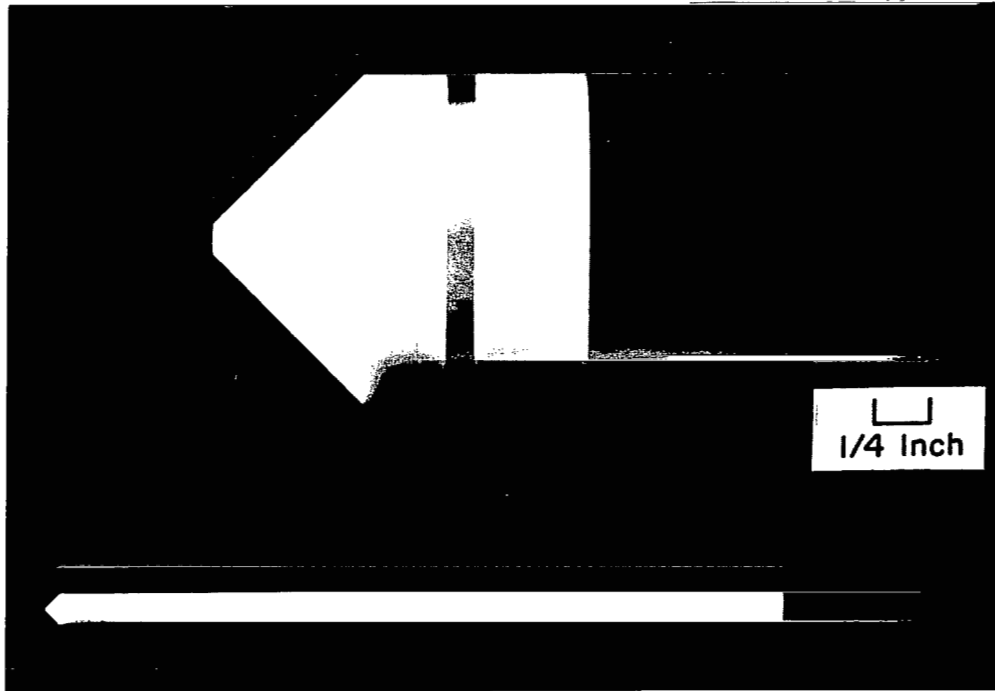


Figure 23.- Profile shape change during ablation for the cusped-cone body  
( $c = 0.3$ ); base radius = 0.75 inch; time interval = 6 sec.



A-30817

Figure 24.- Conical body shape ( $45^\circ$ ) with a 1/16-inch-diameter extruded rod.



A-30818

Figure 25.- Conical body shape ( $45^\circ$ ) with a 1/8-inch-diameter extruded rod.

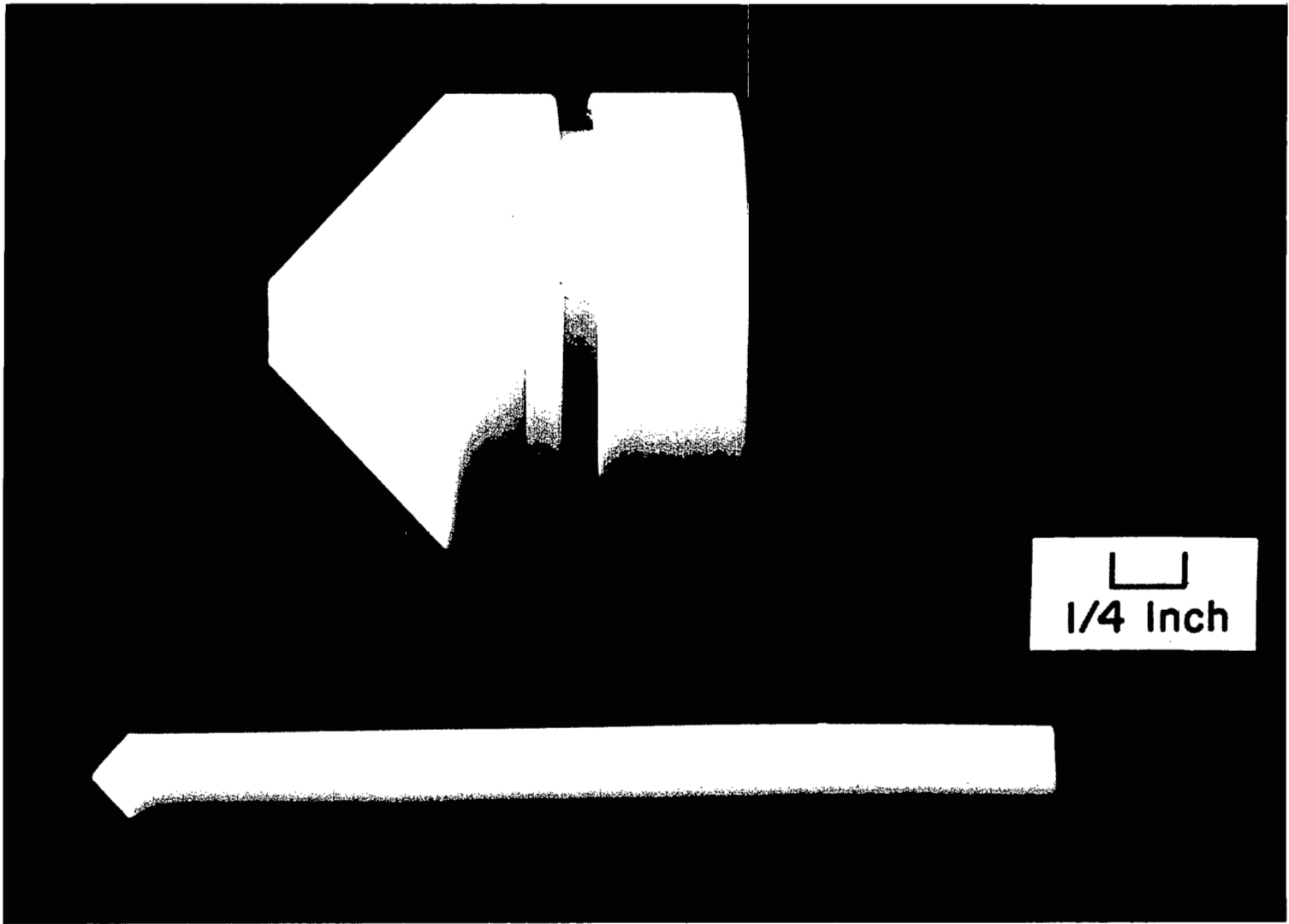
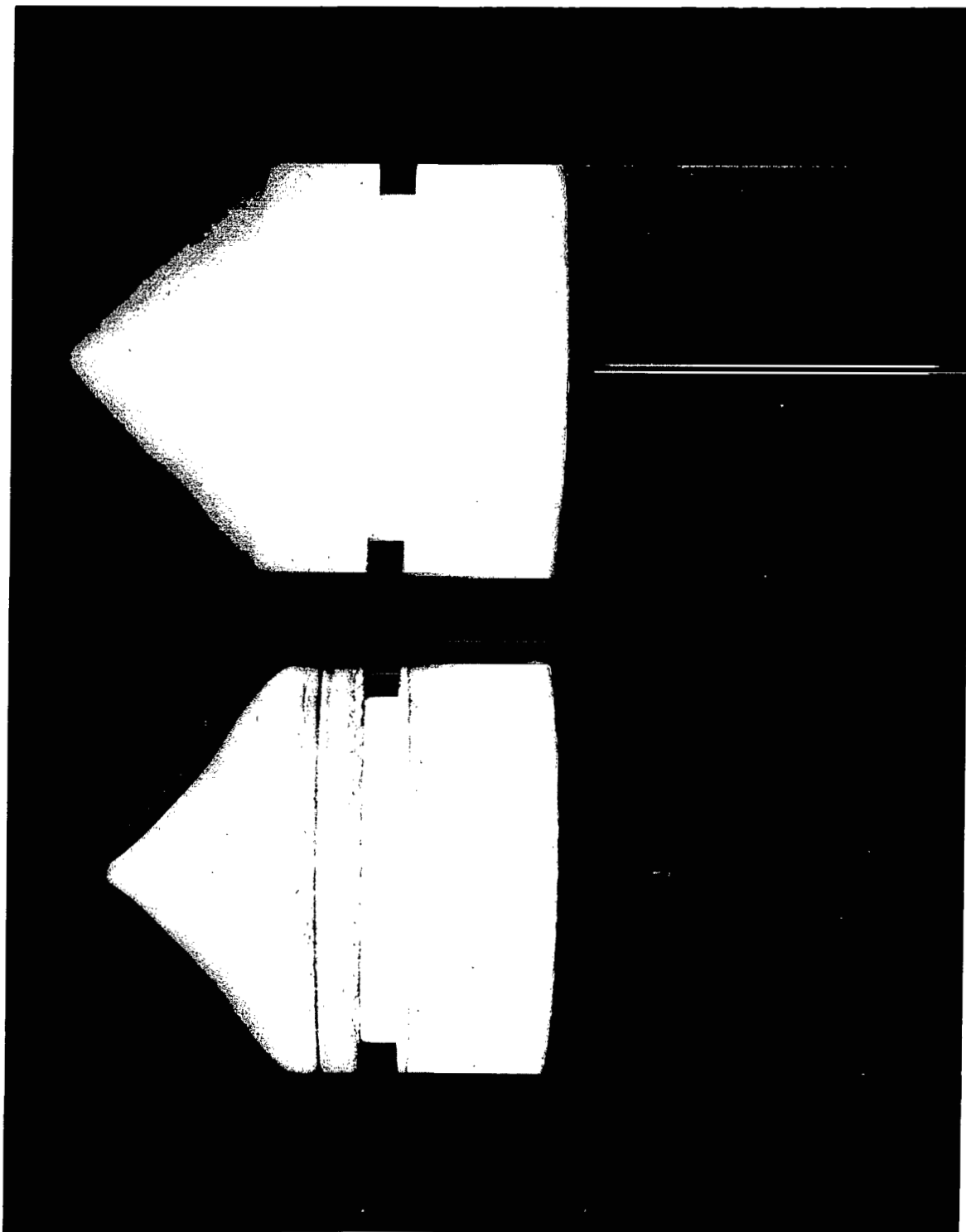


Figure 26.- Conical body shape ( $45^{\circ}$ ) with a 1/4-inch-diameter extruded rod.

A-30819



A-30695.1

Figure 27.- Conical body with a 1/16-inch-diameter rod extruded during exposure to arc-jet stream;  $h_T = 3500$  Btu/lb;  $p_{sp} = 0.114$  atm;  $M = 3.3$ ; exposure time = 18 sec; feed rate = 0.057 in/sec.

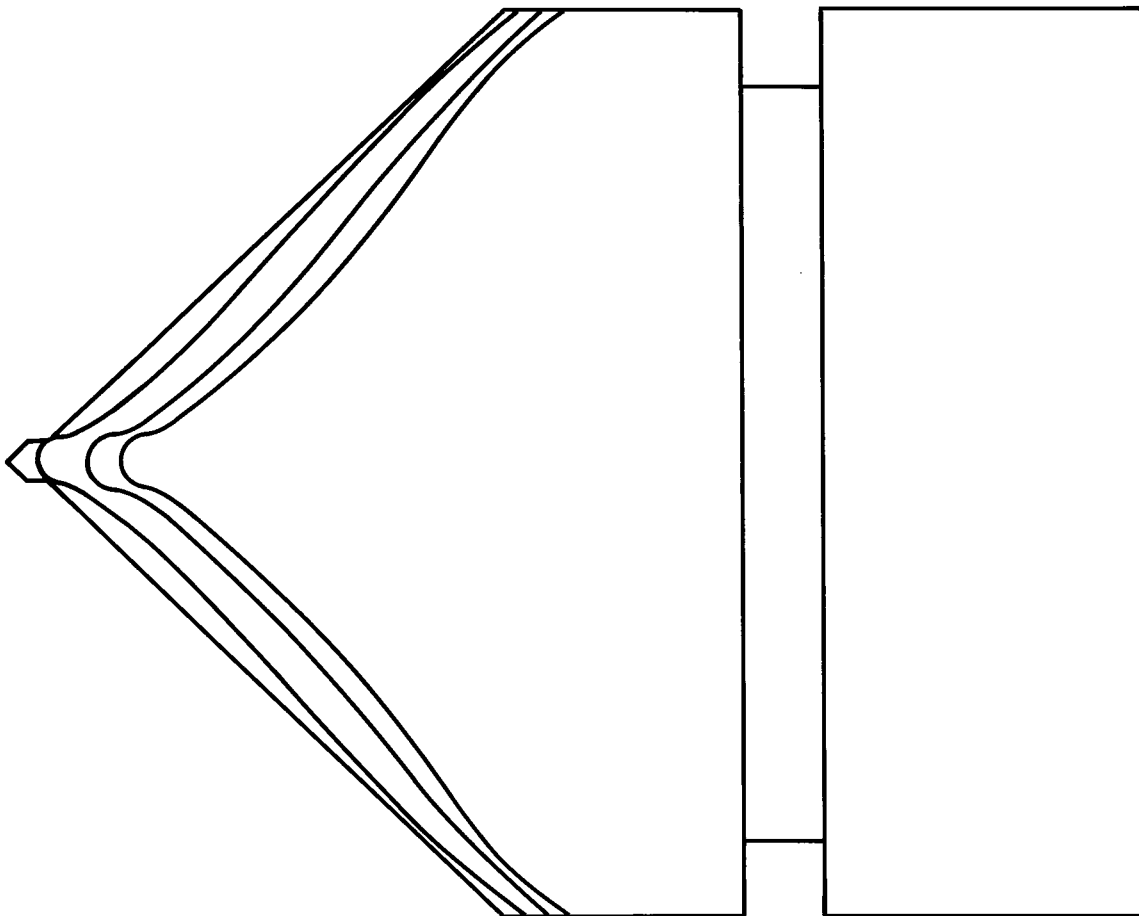
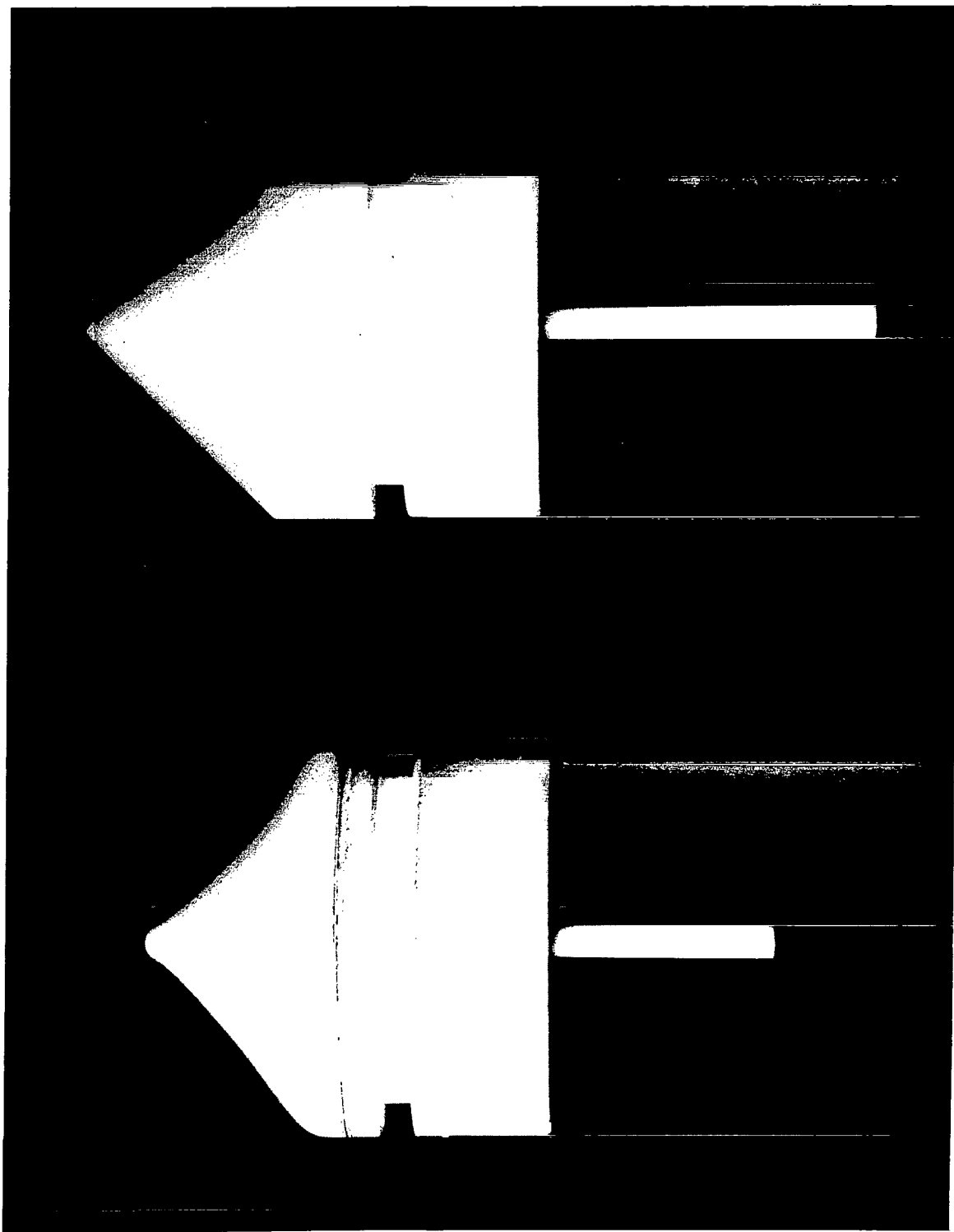


Figure 28.- Profile shape change during ablation for a  $45^\circ$  cone with a  $1/16$ -inch-diameter extruded core; base radius = 0.75 inch; time interval = 6 sec; feed rate = 0.057 in/sec.





A-30840

Figure 29.- Conical body with a 1/8-inch-diameter rod extruded during exposure to arc-jet stream;  $h_T = 3500$  Btu/lb;  $p_{sp} = 0.114$  atm;  $M = 3.3$ ; exposure time = 18 sec; feed rate = 0.034 in/sec.

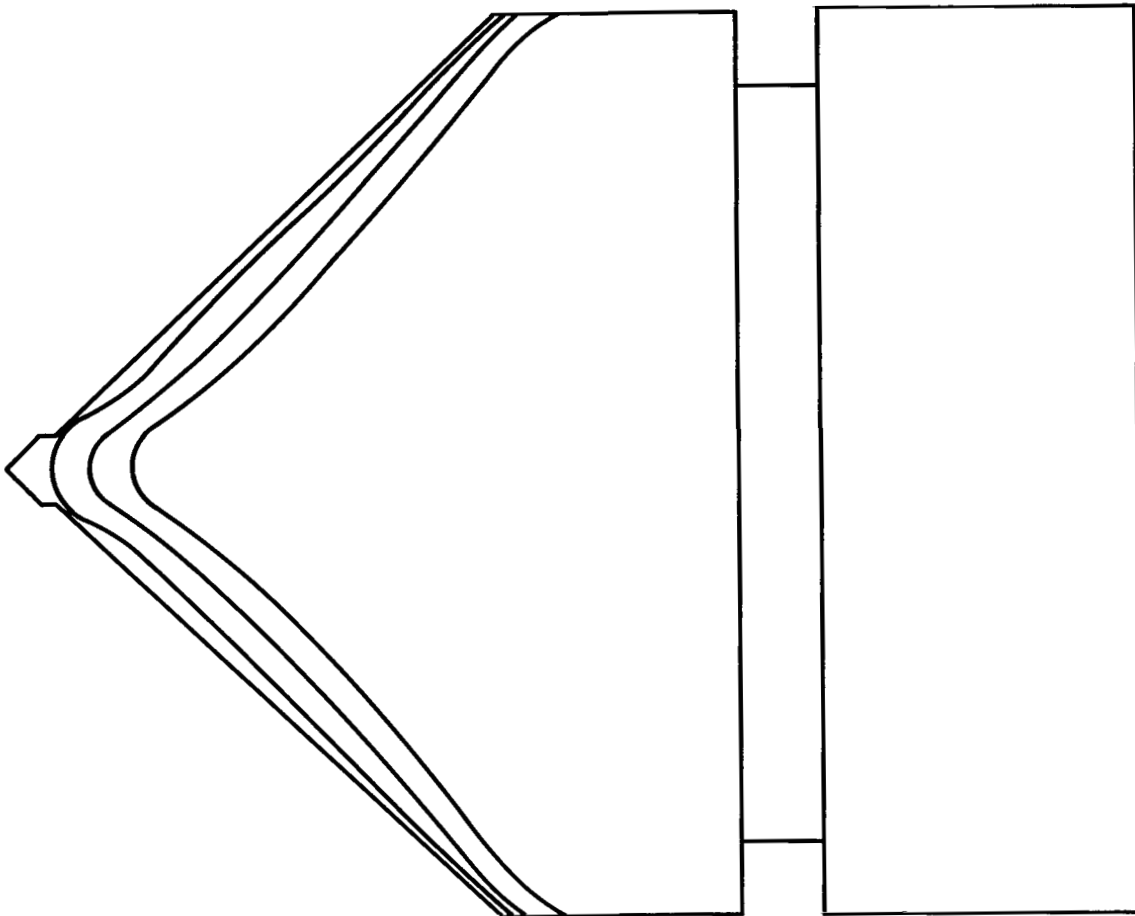
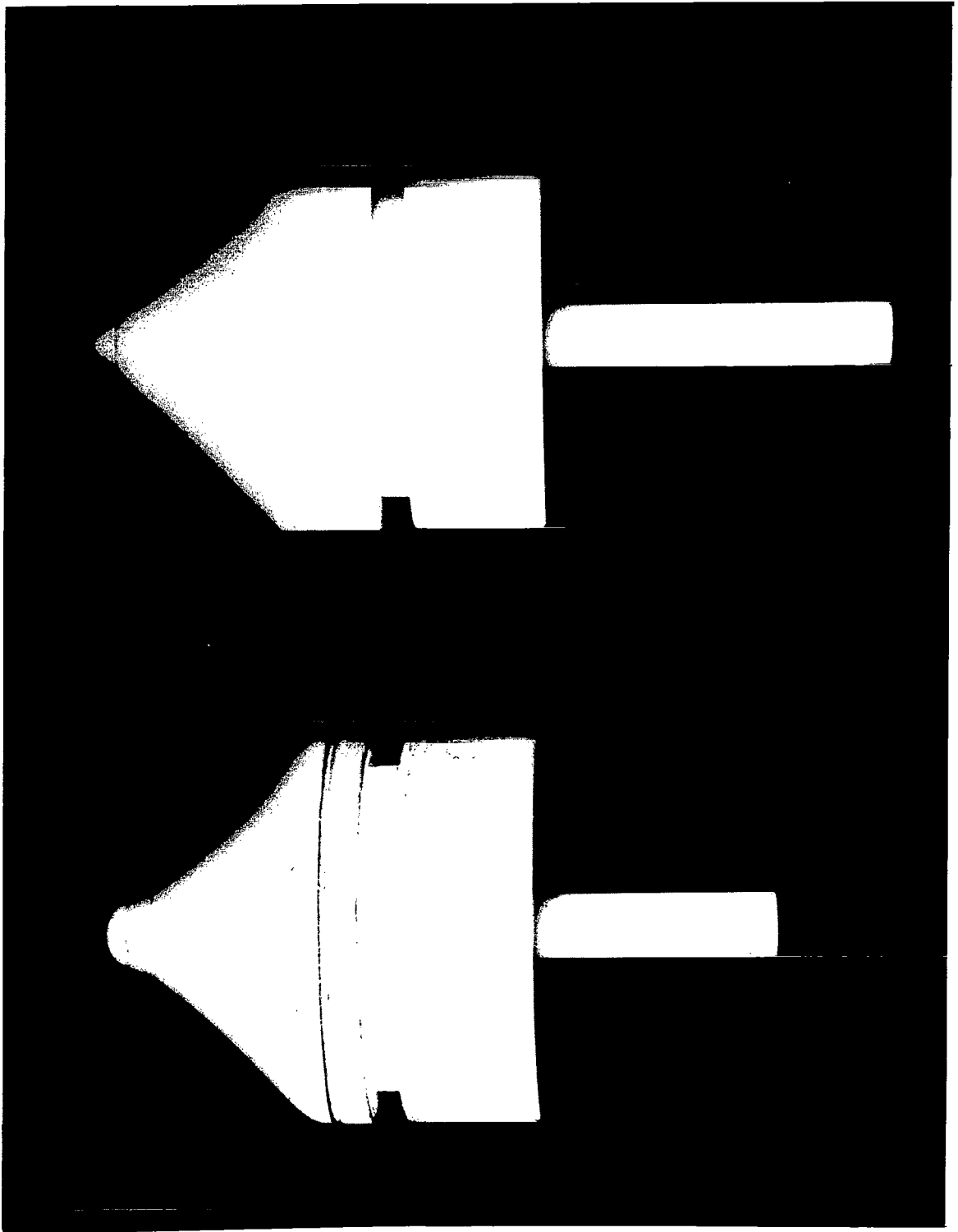


Figure 30.- Profile shape change during ablation for a  $45^\circ$  cone with a  $1/8$ -inch-diameter extruded core; base radius = 0.75 inch; time interval = 6 sec; feed rate = 0.034 in/sec.



A-30839

Figure 31.- Conical body with a 1/4-inch-diameter rod extruded during exposure to arc-jet stream;  $h_r = 3500$  Btu/lb;  $p_{sp} = 0.114$  atm;  $M = 3.3$ ; exposure time = 18 sec; feed rate = 0.024 in/sec.

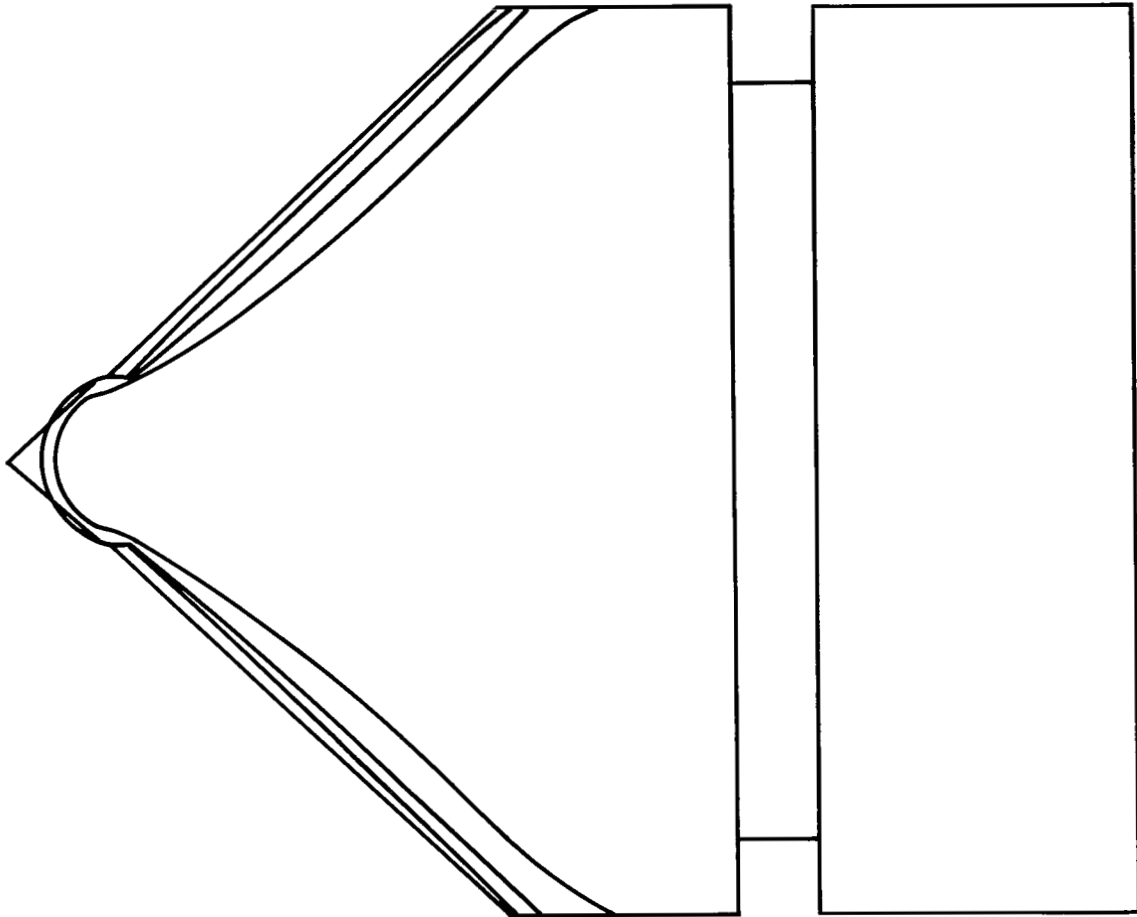


Figure 32.- Profile shape change during ablation for a  $45^\circ$  cone with a  $1/4$ -inch-diameter extruded core; base radius = 0.75 inch; time interval = 6 sec; feed rate = 0.024 in/sec.

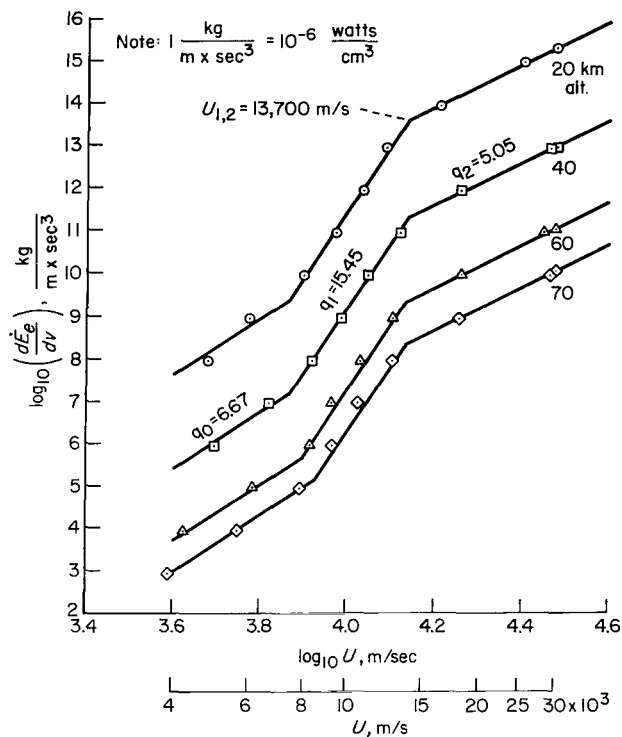


Figure 33.- Equilibrium radiation rate per unit volume of a normal-shock gas cap as a function of flight speed and altitude.

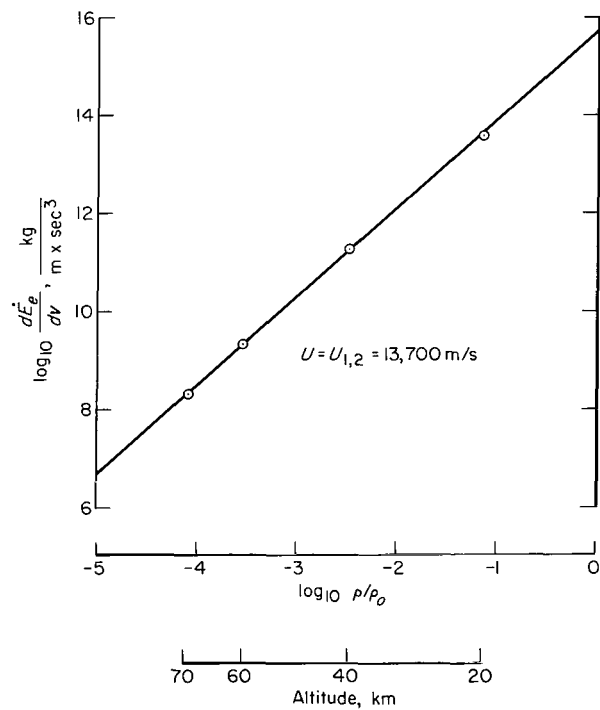


Figure 34.- Dependence of equilibrium radiation on air density.

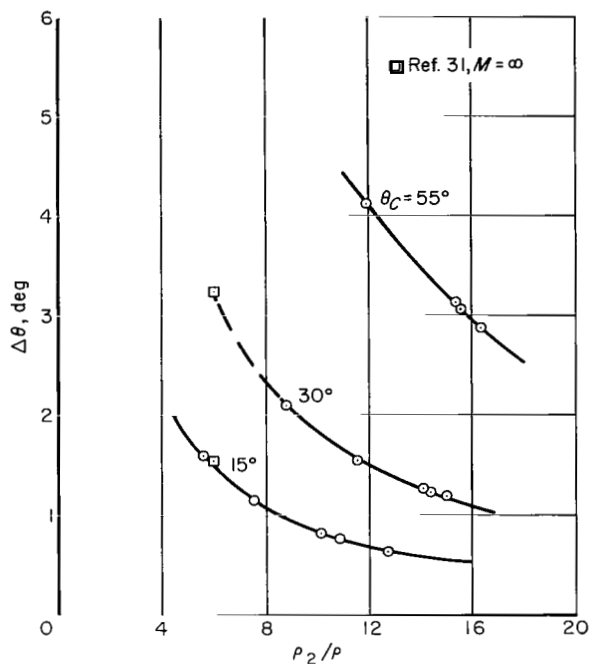


Figure 35.- Dependence of shock-wave-angle increment on cone half-angle and air density jump due to shock compression.

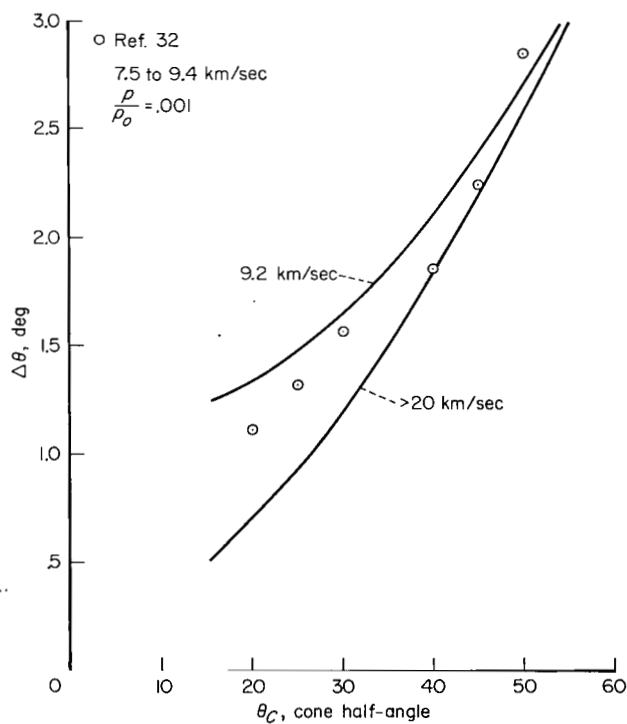


Figure 36.- Approximate shock-wave-angle increment as a function of cone half-angle at high air speeds.

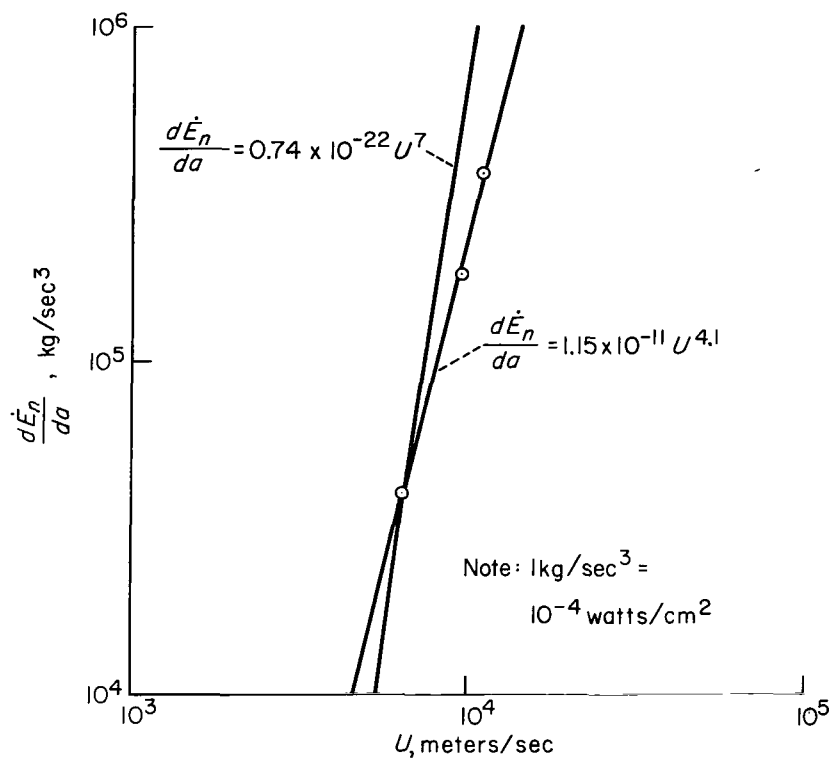


Figure 37.- Nonequilibrium radiation intensity as a function of velocity normal to the shock wave.

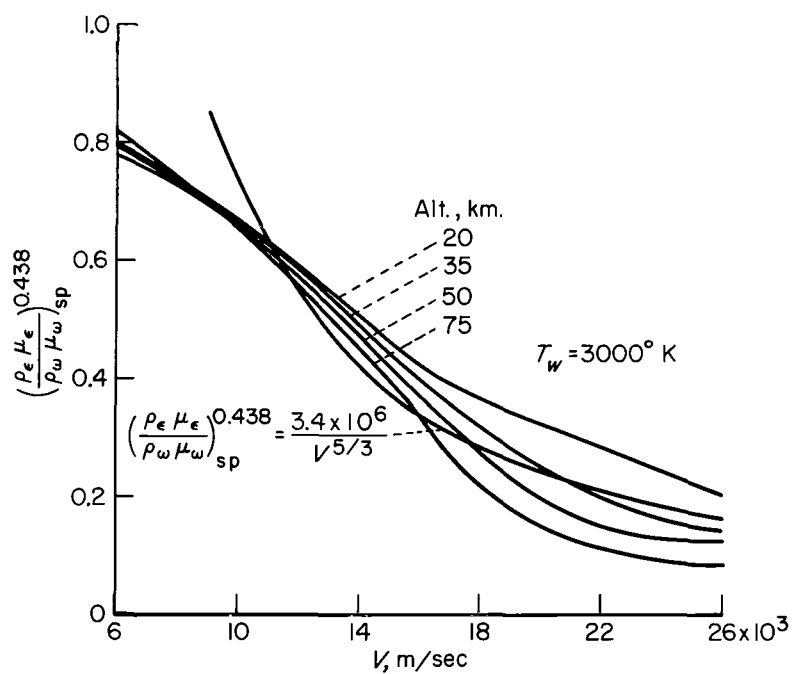


Figure 38.- Variation of the density-viscosity factor as a function of altitude and speed.

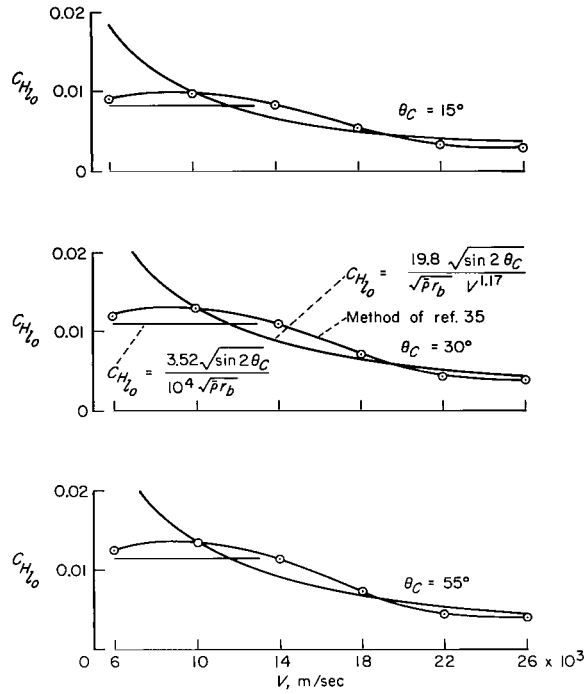


Figure 39.- Variation of heat-transfer coefficient with speed at 50 km altitude for several cone angles and a base radius of 1 meter.

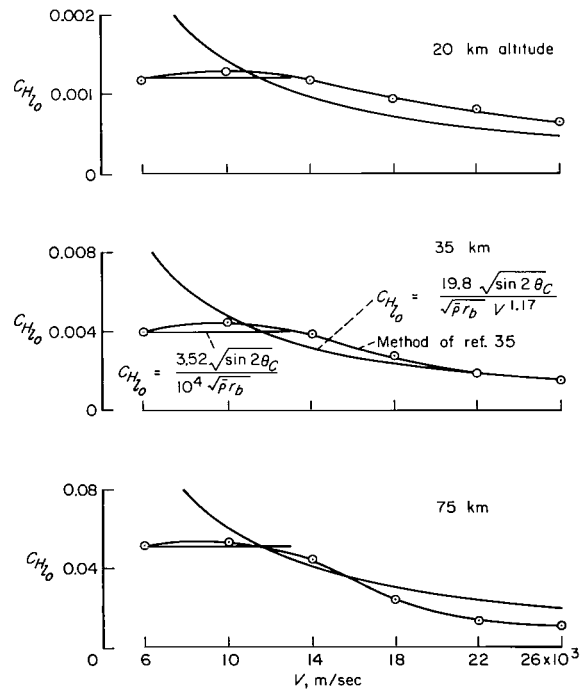


Figure 40.- Variation of heat-transfer coefficient with speed for 30° cone angle at three altitudes for a base radius of 1 meter.



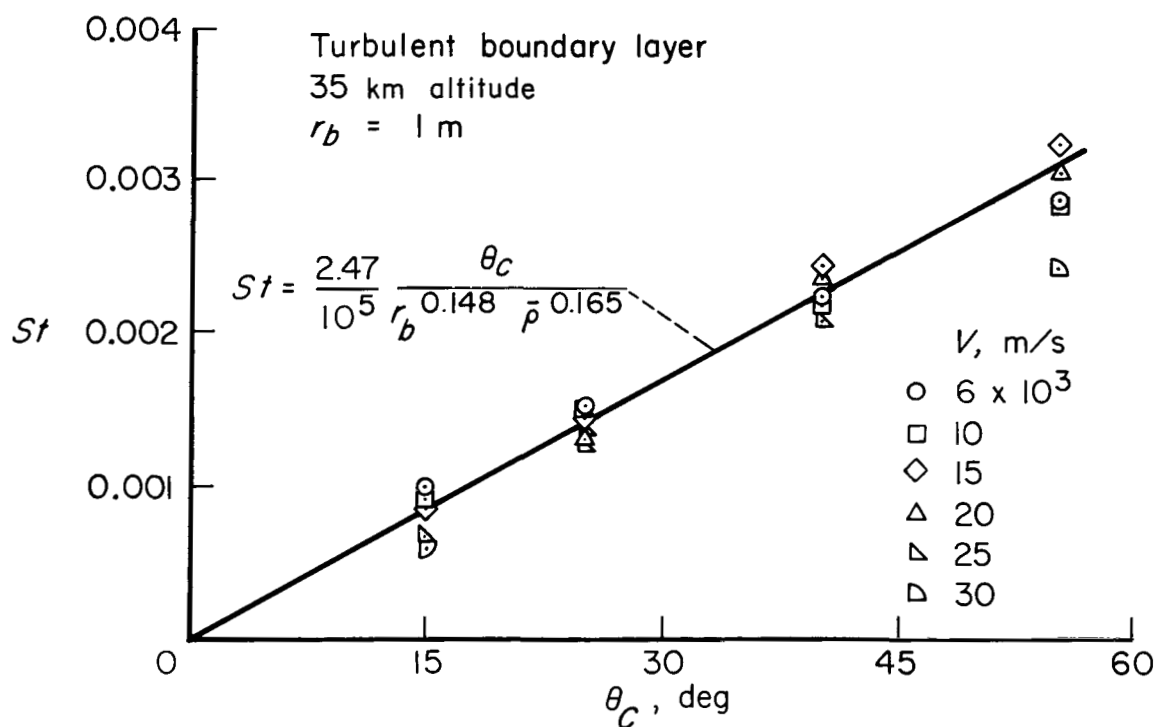


Figure 41.- Stanton number variation with cone angle and speed.

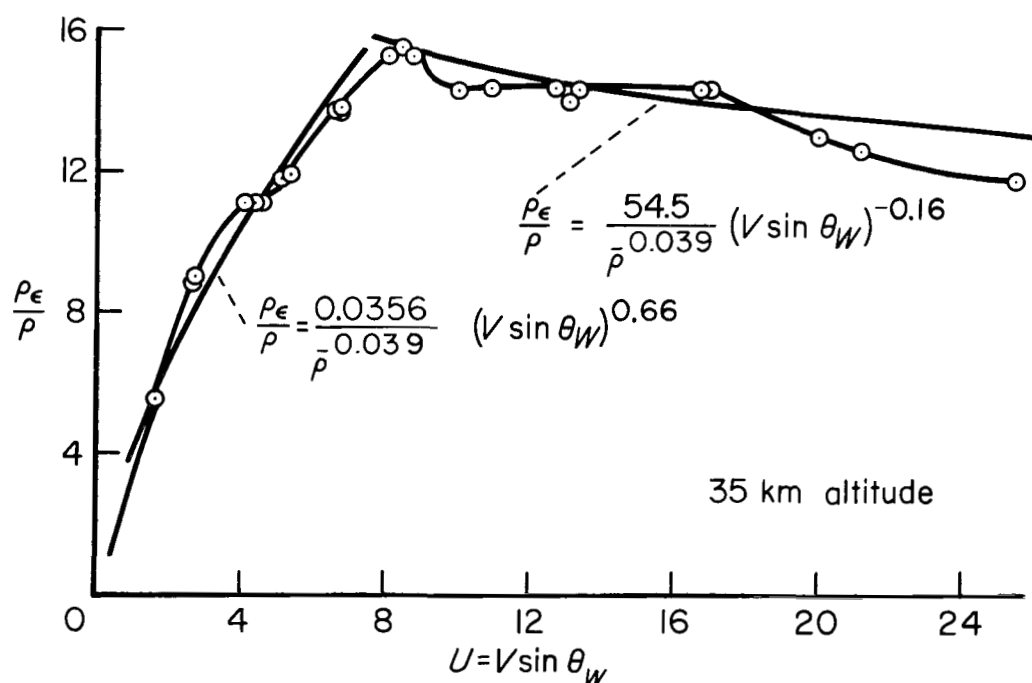


Figure 42.- Density ratio as a function of free-stream velocity component normal to the shock wave.

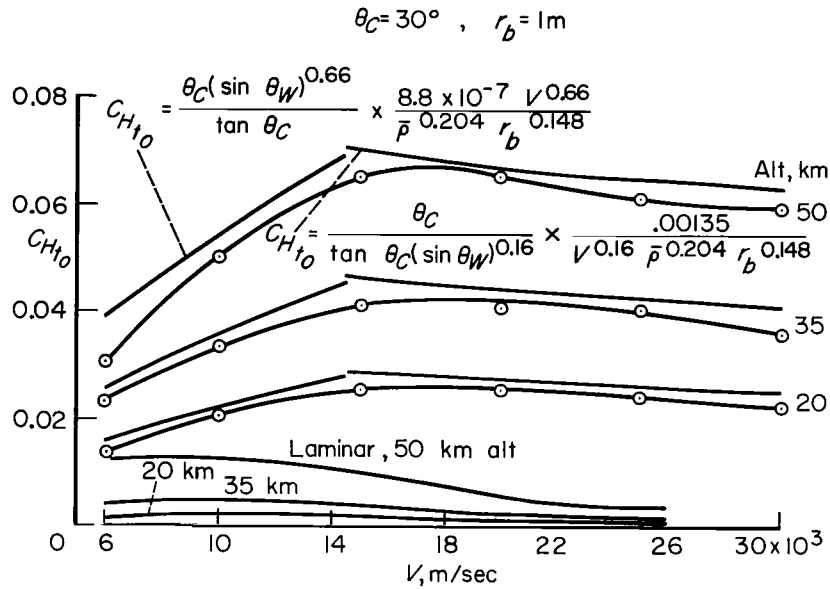


Figure 43.- Estimated heat-transfer coefficients for turbulent boundary layer compared with working equations and laminar boundary-layer values.

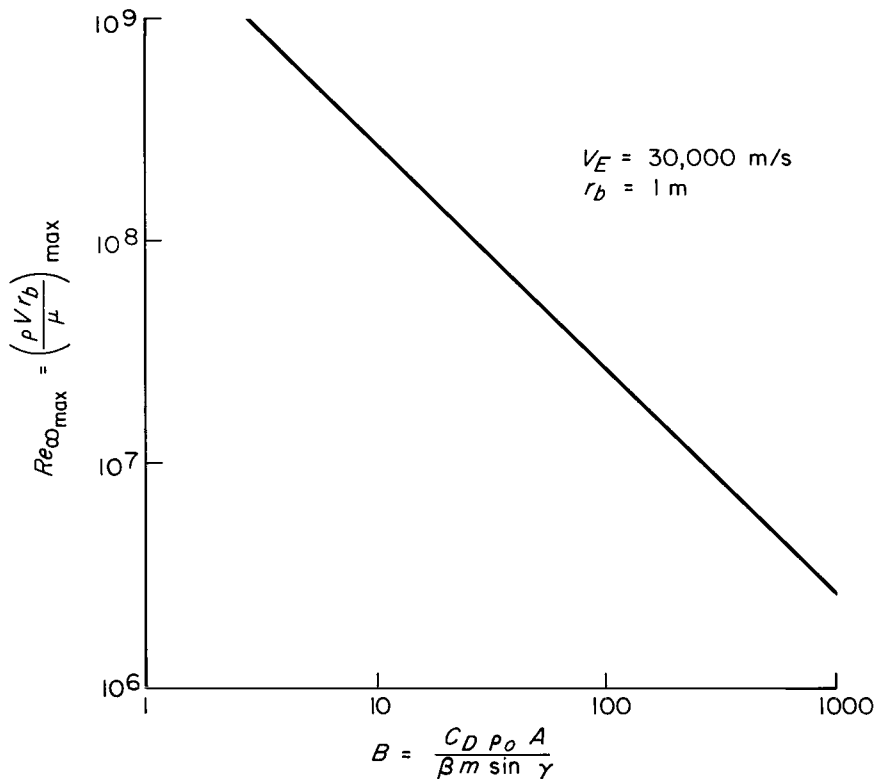


Figure 44.- Maximum free-stream Reynolds number during entry as a function of the ballistic coefficient.

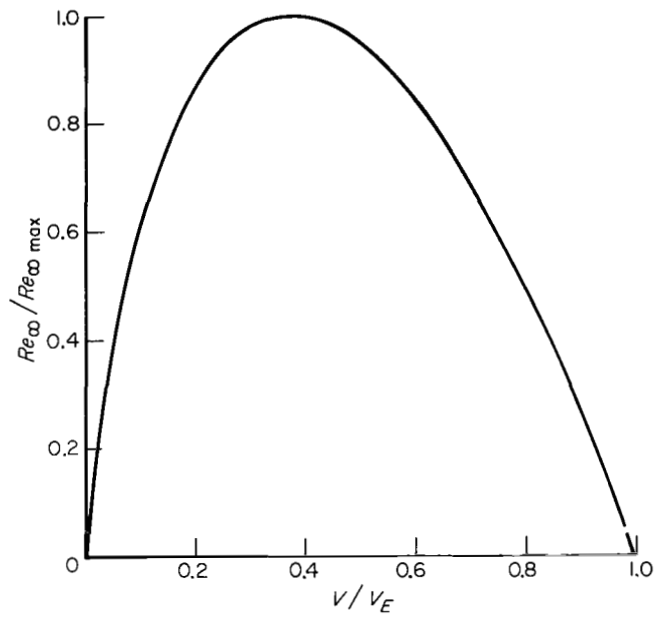


Figure 45.- Variation of free-stream Reynolds number during entry.

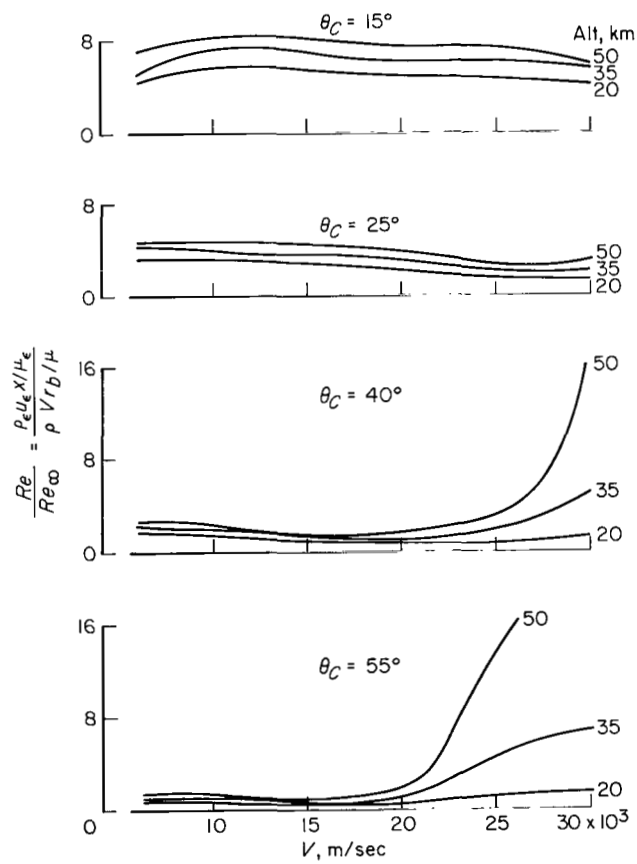
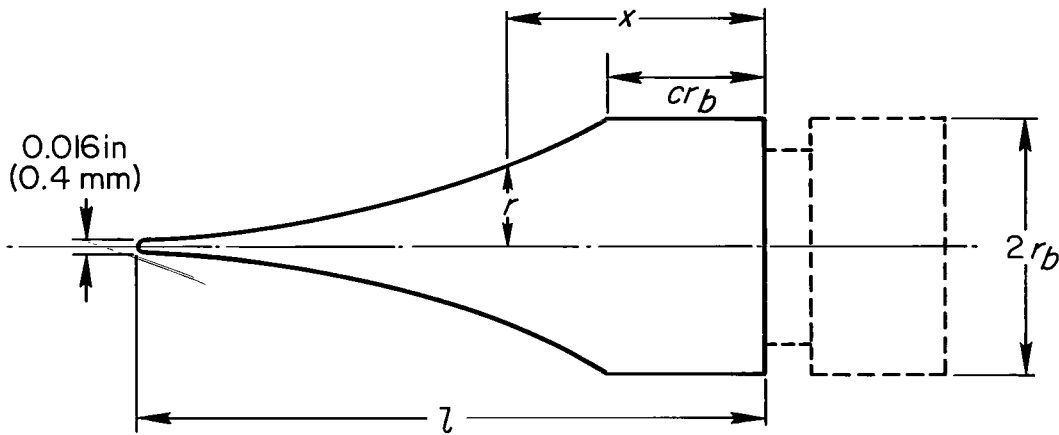


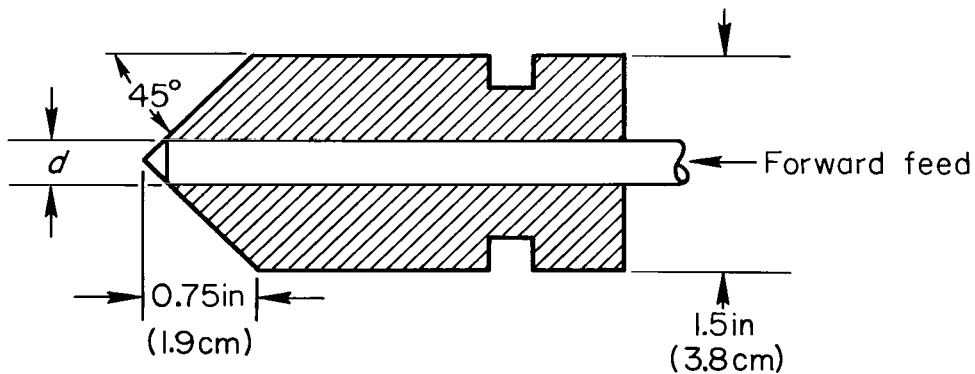
Figure 46.- Ratio of local to free-stream Reynolds numbers.

Cusped cone equation  $r = r_b - x + \frac{cr_b^{3/2}}{\sqrt{r}}$



Model designation	$r_b$	$cr_b$	$l$
$c = 0$	0.75 in (1.9 cm)	0 in (0 mm)	0.75 in (1.90 cm)
$c = 0.1$	0.75 in (1.9 cm)	0.075 in (1.9 mm)	1.08 in (2.74 cm)
$c = 0.2$	0.75 in (1.9 cm)	0.15 in (3.8 mm)	1.45 in (3.67 cm)
$c = 0.3$	0.75 in (1.9 cm)	0.225 in (5.7 mm)	1.81 in (4.58 cm)

Figure 47.- Cusped-cone models.



Model designation	Core diameter, $d$
No. 1	0.25 in (6.35 mm)
No. 2	0.125 in (3.17 mm)
No. 3	0.0625 in (1.58 mm)

Figure 48.- Extruding apex models.